EARTHQUAKE APPARENT STRESS VARIATION IN RESPONSE TO SEAMOUNT SUBDUCTION AT NICOYA PENINSULA, COSTA RICA

by

Jana Stankova-Pursley

Submitted in Partial Fulfillment

of the Requirements for the Degree of

Master of Geophysics

New Mexico Institute of Mining and Technology

Socorro, New Mexico

December, 2008

ABSTRACT

Seamounts are high relief features seen on many oceanic plates, and when these features enter the subduction zone trenches, they may perturb interface coupling by changing physical properties of the plate interface. This in turn can then affect spatial heterogeneity for earthquakes on the plate interface. In this study I explore the role of seamounts on the rupture process of microseismicity along Nicoya Peninsula, Costa Rica. This peninsula lies close to a region where the down-going Cocos plate structure varies along-strike of the Middle America Trench (MAT). The Cocos plate has low relief along the northern and central portion of the Nicoya Peninsula, where the subducting plate was created at the East Pacific Rise (EPR). Seamounts dot the plate where it subducts at the southern tip of the Nicoya Peninsula because this segment of the plate was created at the Cocos-Nazca Spreading center (CNS). Given these structural differences, I evaluate possible along-strike variations in earthquake source properties. I use 353 earthquakes from the Costa Rica Seismogenic Zone Experiment (CR-SEIZE) to estimate the effects of bathymetric variability on apparent stress (σ_a). I compute σ_a, which is a measure of stress drop combined with seismic efficiency, using waveform coda because of its proven stability relative to measurements using direct arrivals. Apparent

stress values for well constrained data indicate along strike variations between the northern and southern portions of the peninsula. Except in the region of a previously subducted seamount in the Gulf of Nicoya where the median σ_a is 0.52 MPa, the southern and central portions of the peninsula have median σ_a values 0.43 and 0.66 MPa respectively. In comparison, the median σ_a value in the northern region is 1.2 MPa. The larger median σ_a values in the northern region and in the Gulf of Nicoya imply that the interface is more strongly coupled or experiences higher friction where there is little relief on the subducting plate or surrounding a subducting seamount. I compared the earthquake σ_a distribution with the geodetic and b-value studies done on the Nicoya Peninsula. As suggested by low geodetic interface locking and high b-value, the friction is likely lower along the subduction zone interface beneath the southern portion of Nicoya Peninsula except in the small region near the subducting seamounts. The geodetic studies also suggest that the subduction zone interface experiences higher locking at the northern portion of the Nicoya Peninsula, which is reflected in higher number of large σ_a earthquakes in that region compared to the southern portion of the peninsula.

ACKNOWLEDGMENT

I am indebted to my research committee, Susan Bilek, Scott Phillips, and Rick Aster, for their generous advice, useful comments and instructional critique during this study. The data and useful discussions regarding the seismic network were provided by Andrew Newman. I am grateful for the assistance of my research colleagues, especially Kimberly Schramm. I would like to thank my family for their continuous support and patience. This work was partially funded by the Los Alamos National Laboratories, New Mexico.

This report was typeset with LaTeX[1] by the author.

[1] LaTeX document preparation system was developed by Leslie Lamport as a special version of Donald Knuth's TeX program for computer typesetting. TeX is a trademark of the American Mathematical Society. The LaTeX macro package for the New Mexico Institute of Mining and Technology report format was adapted from Gerald Arnold's modification of the LaTeX macro package for The University of Texas at Austin by Khe-Sing The.

TABLE OF CONTENTS

LIST OF TABLES

LIST OF FIGURES

This report is accepted on behalf of the faculty of the Institute by the following committee:

Susan L. Bilek, Advisor

Jana Stankova-Pursley

Date

CHAPTER 1

INTRODUCTION

The majority of Earth's large, damaging earthquakes occur in subduction zones. The size of these earthquakes is related to the area of rupture, amount of slip and rigidity. The rupture area and slip amount are influenced by the coupling between the subducting and overriding plates. The amount of coupling between the plates can be affected by the amount of sediment influx into the trench, the age of the subducting plate, or the presence of seamounts or ridges on the subducting plate. Seamounts and ridges are features that can extend thousands of meters above the seafloor and cause changes in the physical properties of the plate interface as they enter the subduction zone.

Several studies have discussed the effects of seamount subduction in convergent margin settings on the local stress regime and earthquake rupture process. In general, subducting seamounts are thought to act as large asperities (or protrusions on the otherwise smooth interface as defined by *Scholz* (2002)) that increase the normal stresses on the interface, thus increasing the coupling in the region (*Cloos*, 1992; *Scholz and Small*, 1997). The level of subduction zone coupling is reflected in the stick-slip behavior along the interface; higher coupling regions are those in which stress is reduced during stick-slip events, while in low-coupled regions the stress is reduced constantly during aseismic slip (e.g. *Scholz and Small*, 1997). Recent work suggests that seamounts at

an earlier stage in the subducting process can weaken the coupling due to the amount of fluids that are being subducted (*Mochizuki et al.*, 2008). In the Japan Trench, east of the southern portion of the Honshu Island, a magnitude 7 earthquake occurred in 1982. This earthquake was located downdip of a subducting seamount, which was imaged using active source data at about 13 km depth in the subduction zone (*Mochizuki et al.*, 2008). *Mochizuki et al.* (2008) also recorded 257 microearthquakes during a month-long experiment in that region in 2005 and concluded that majority of the events located downdip of the seamount. The authors suggest that as the seamounts subduct, the release of fluids from the subducted sediment and the seamount itself creates a low friction surface at the interface, hence promotes weak coupling. *von Huene* (2008) proposed that as the amount of fluids decrease to about $\frac{1}{10}$th of the original volume, the coupling at the interface will increase and the seamount will begin to act as an asperity. As the slab-pull stresses exceed the normal stress acting on the seamount, the seamount will fracture or shear off in an underthrusting earthquake (*Park et al.*, 1999; *Abercrombie et al.*, 2001; *Husen et al.*, 2002). *Park et al.* (1999) imaged a possibly fractured seamount in the Japan subduction zone, near the Shikoku Island. In the 1994 Java earthquake, the rupture occurred near the top of the subducted seamount and bottom of the overriding plate (*Abercrombie et al.*, 2001). The 1990 Gulf of Nicoya earthquake seemed to rupture the basal part of the seamount (*Husen et al.*, 2002). In all of the three cases, the seamounts seemed to act as asperities along the subduction zone interface, which resulted in large slip earthquakes along the interface.

Near the southern end of the Nicoya Peninsula, Costa Rica, the sub-

ducting Cocos Plate carries seamounts that reach heights of 2.5 km into the subduction zone (Figure 1.1). The size of the subducting feature and its position within the subduction zone has an effect on the earthquake rupture and subduction processes. Rupturing individual seamounts can result in simpler source time functions and shorter source durations as opposed to rupturing portions of subducting ridges (*Bilek et al.*, 2003). If a seamount subducts along an otherwise weakly coupled interface, the background seismicity can become very low seaward of the subducted seamount prior to its rupture (*Abercrombie et al.*, 2001) due to aseismic slip seaward of the seamount. Anomalously large seamounts, such as the seamounts of the Louisville Seamount Chain entering the Tonga-Kermadec trench, can hinder the subduction process and possibly cause deformation of the subducting plate hundreds of km seaward from the trench (*Small and Abbott*, 1998). The diameter of the largest of these seamounts is about 100 km, which is five times the average diameter of seamounts subducting beneath Costa Rica. Thus, the Costa Rican seamounts can change the coupling along the interface, but they are not large enough to hinder the subduction process.

My goal is to determine the effects of the subducting topography on earthquake rupture process in the Cocos - Caribbean Plate convergent margin by computing apparent stress (σ_a) using earthquake coda spectral amplitudes. The Costa Rican convergent margin is ideal for this study because the Nicoya Peninsula lies directly above the seismogenic zone, thus the Costa Rica Seismogenic Zone experiment (CR-SEIZE) seismic network recorded high quality microearthquake data. In addition, Nicoya Peninsula lies over the suture between East Pacific Rise (EPR) and Cocos-Nazca Spreading Center (CNS)

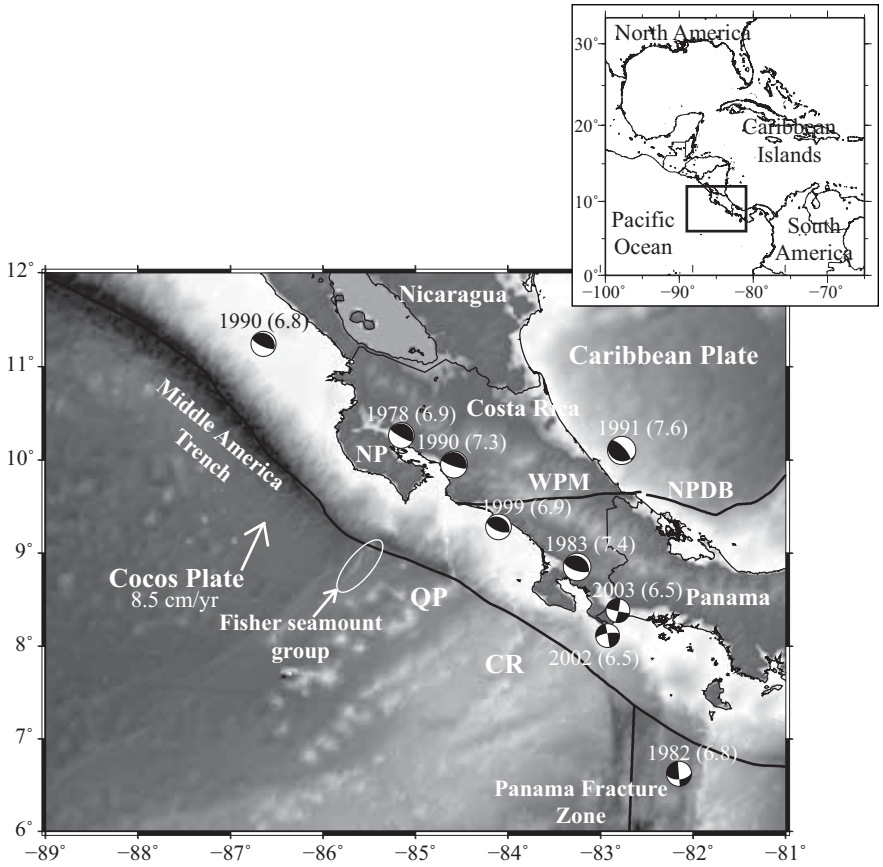

Figure 1.1:
The Cocos Plate subducts at about 8.5 cm/year beneath the Caribbean Plate. Other large tectonic features in Costa Rica are the western boundary of the Panama Microplate (WPM) and the North Panama Deformed Belt (NPDB), which separate the Caribbean Plate from the Panama Microplate (*Fisher et al.*, 1994). Beneath northern Nicoya Peninsula (NP), the smooth Cocos Plate crust from EPR enters the trench. At the southern tip of Nicoya Peninsula, high topography Cocos Plate crust from CNS carries numerous seamounts (e.g. Fisher seamount group) into the trench. Other high topography features at this margin are the Quepos Plateau (QP) and the Cocos Ridge (CR). Also shown are CMT solutions for historical earthquakes in Costa Rica with magnitude larger than 6.5 (focal solutions from Global CMT catalog). The year and magnitude of the earthquakes are given in parentheses.

formed crust, therefore I could directly compare σ_a values for earthquakes across EPR-CNS suture (Figure 1.2). Historically, three large earthquakes occurred at the subduction zone interface (M_s 7.7 on October 5, 1950; M_s 7.0 on August 23, 1978; and M_w 7.0 on March 25, 1990; *Avants et al.* (2001)) beneath Nicoya Peninsula. Only the 1990 Gulf of Nicoya event is associated with seamount subduction (*Husen et al.*, 2002). The other two events occurred close to the EPR-CNS suture. The 1950 earthquake located north of the suture, while the 1978 earthquake located south of the suture (*Avants et al.*, 2001). Earthquakes recorded during CR-SEIZE cover the whole peninsula, providing adequate data coverage across the EPR-CNS suture to study the effects of variable plate structure on σ_a.

Apparent stress is a measure of stress drop combined with seismic efficiency (*Wyss and Molnar*, 1972; *McGarr*, 1999), and it has been used in numerous studies to evaluate source properties (e.g. *Mayeda et al.*, 2003; *Eken et al.*, 2004; *Malagnini et al.*, 2006; *Choy et al.*, 2006). *Choy and Boatwright* (1995) show that the value of average apparent stress is tied to the faulting mechanism, tectonic and regional setting. *Choy et al.* (2006) suggest that the size of σ_a is related to the maturity of the fault that is being ruptured. Using a global earthquake dataset with events of $m_b \geq 5.8$, *Choy et al.* (2006) suggest that highly mature faults support events with an average σ_a of 0.3 MPa, while immature faults can support events with average σ_a of 3.7 MPa. Thrust fault events from the subduction zone interface fall into the category with the smallest average σ_a values, which *Choy et al.* (2006) attribute to high fault maturity due to large accumulated displacements along the fault and/or high pore fluid pressure. *Choy and Boatwright* (1995) obtained average σ_a 0.29

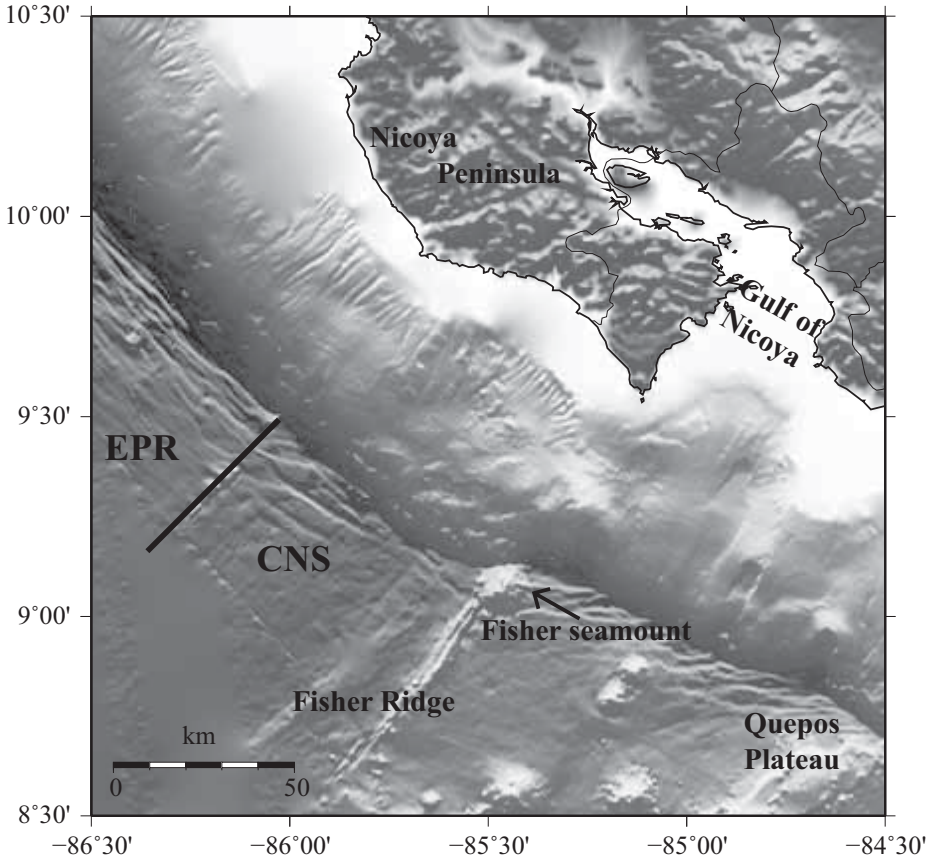

Figure 1.2:
This is a high resolution bathymetry image of the subducting Cocos Plate near Nicoya Peninsula, Costa Rica (*Ranero et al.*, 2003). The Cocos Plate subducting along northern portion of Nicoya is relatively flat (EPR origin). At the southern boundary of the peninsula, the subducting Cocos plate carries seamounts and ridges into the trench (CNS origin). The suture between the two structurally distinct portions of the plate shows in the bathymetry data as vertically offset seafloor (solid line). The Fisher seamount and ridge are subducting at the southern tip of the Nicoya Peninsula. Also shown here is the Quepos Plateau, which subducts beneath central Costa Rica.

MPa for subduction zone earthquakes using 222 thrust events. Eight of these events were used to compute average σ_a of 0.28 MPa for the entire Middle America subduction zone. Earthquakes with high average σ_a values occur in regions that have experienced very little displacement in the past, or none at all. These regions are located intraplate of oceanic slabs, near spreading ridges and transform faults, where young, immature faults are being ruptured (*Choy and Boatwright*, 1995; *Choy et al.*, 2006). However, *Choy and Boatwright* (1995) also suggest that irregularities on the surface of the subducting plate might cause increase in σ_a values, because they can change the stress regime of the region.

In order to compute σ_a from my data, I use the amplitudes from earthquake coda waves (Figure 1.3). Coda waves originate as the body and

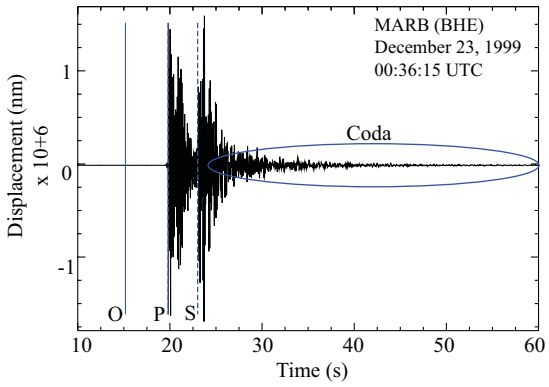

Figure 1.3:
Displacement signal from December 23, 1999, M_L 4.11 earthquake recorded at station MARB that occurred at 00:36:15 UTC at 85.7^{o}W, 10.1^{o}N and 25 km depth. Shown are the origin time (O), P- and S-wave arrivals (dashed lines), and the coda portion of the seismogram (ellipse).

surface waves that scatter in the Earth due to inhomogeneities along their

path from the earthquake source to the recording station (*Aki*, 1969; *Aki and Chouet*, 1975). It has been shown that coda amplitude measurements are more stable in determining source properties than direct body waves due to their relative insensitivity to source radiation patterns and crustal heterogeneities (*Chouet et al.*, 1978; *Rautian and Khalturin*, 1978; *Mayeda*, 1993; *Mayeda and Walter*, 1996; *Eken et al.*, 2004; *Malagnini et al.*, 2004, 2006; *Mayeda et al.*, 2007). The interstation coda amplitude measurements are very similar given variable seismic network size and tectonic setting, which makes this technique ideal for spectral studies in regions with sparse network coverage, large tectonic complexity, or unknown subsurface structure (e.g. *Eken et al.*, 2004; *Malagnini et al.*, 2004).

CHAPTER 2

TECTONIC SETTING

Nicoya Peninsula, Costa Rica, is situated above the seismogenic zone resulting from the convergence between the Caribbean and Cocos Plates (Figure 1.1). The convergence rate is about 8.5 cm/year oriented at 25^o east of north (*Newman et al.*, 2002). The Cocos Plate originated following the breakup of the Farallon Plate at about 23 Ma (*Barckhausen et al.*, 2001), possibly due to passage of a weak region within the Farallon plate over the Galapagos hotspot (*Hey*, 1977; *Werner et al.*, 1999). New crust of Cocos plate is formed at the Cocos-Nazca spreading center (CNS) in the south, and at the East Pacific Rise (EPR) in the west. The suture between the oceanic crust originated at EPR and CNS subducts beneath the central Nicoya Peninsula (*Barckhausen et al.*, 2001; *Fisher et al.*, 2003). The whole triple junction system between Pacific, Cocos and Nazca plates is moving to the north. However, as interpreted from magnetic data, the CNS boundary has undergone several ridge-jumps toward the south, possibly due to the Galapagos plume position (*Hey*, 1977; *Barckhausen et al.*, 2001).

The variable origin of the plate affects its structural character. There are differences across the EPR-CNS suture in the temperature of the plate entering the trench, its surficial topography, the seismogenic updip limit, and the geologic structures on the continent near the subduction zone (*Fisher et al.*,

1998; *Silver et al.*, 2000; *von Huene et al.*, 2000; *Harris and Wang*, 2002; *Newman et al.*, 2002; *Fisher et al.*, 2003; *Spinelli et al.*, 2006). The crustal temperature difference influences the rate of mineral reactions and fluid viscosity of the interface, which in turn affects the seismogenic updip limit. The subducting surficial topography has an effect on the forearc deformation. Both the crustal temperature difference and heterogeneous topography across the suture are due to the variable plate origin.

2.1 Thermal state

The EPR formed crust is colder than the CNS formed crust due to higher hydrothermal circulation (Figure 2.1). The conductive heat flow of crust originated at the EPR is only 20-40 mW/m^2, and has been attributed to fast spreading at EPR resulting in high permeability of the oceanic basement rock (*Fisher et al.*, 2003). High permeability, and consequently low conductive heat flow, for crust formed at EPR is also suggested by *Silver et al.* (2000), who estimated that conductive heat flow values from boreholes drilled just north of the EPR-CNS suture are only about 10% of what is expected for conductive heat flow of a 24 Ma old oceanic crust. The heat flow measured at CNS formed crust is 105-115 mW/m^2, which is consistent with conductive lithospheric models (*Fisher et al.*, 2003).

This variable plate temperature has an effect on the updip limit of the seismogenic zone across the EPR-CNS suture. *Harris and Wang* (2002) modeled the thermal conditions of subducting EPR beneath northern Nicoya Peninsula to estimate the seismogenic updip limit as given by the intersection of 100^oC and the onset of seismicity. Their results show that at the northern

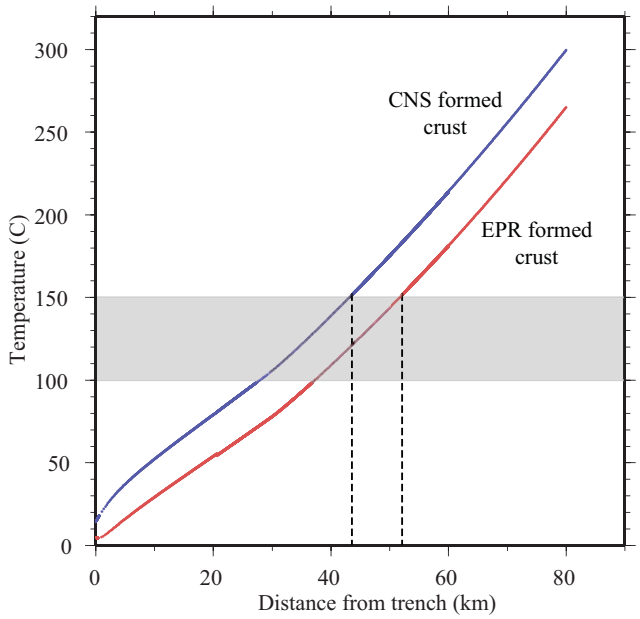

Figure 2.1:
Temperature profiles for the EPR and CNS formed crust from *Spinelli and Saffer* (2004). At the diagenetic reaction temperatures for opal and smectite (shaded box), the EPR crust is about 25^{o}C cooler (lower, red line) than the CNS crust (upper, blue line). This contributes to the shift in seismogenic updip limit along the dècollement (dashed lines). The seismogenic updip limit is at about 43 km from the trench on CNS crust, and it is at 52 km from the trench on EPR crust (dashed lines).

peninsula the seismogenic updip limit is about 60 km landward from trench. Interpretations of opal and smectite diagenetic reaction modeling suggest that the seismogenic updip limit along the southern peninsula is about 10 km closer to the trench than along the northern peninsula (*Spinelli and Saffer*, 2004; *Spinelli et al.*, 2006). In addition to mineralogic reactions, *Spinelli et al.* (2006) suggest that the difference in the seismogenic updip limit could also be due to higher fluid viscosity of the EPR crust compared to lower viscosity of the CNS

crust, assuming the same permeability for crust of both origins. Viscosity is directly related to temperature, at high temperatures viscosity is low and vice versa. Thus, dècollement fluid pressures in warmer systems (e.g. CNS formed crust) are lower than dècollement fluid pressures in colder system (crust formed at EPR). This means that to induce stick-slip behavior in the colder system, greater effective normal stress is needed.

2.2 Seismicity distribution

Güendel et al. (1989) analyzed earthquakes recorded on the first large seismic network in Costa Rica and realized that there is large difference in the dip of the Wadati-Benioff zone between events located near Nicaragua and those located in the central Costa Rica. Data recorded during the Costa Rica Seismogenic Zone Experiment (CR-SEIZE) confirm that indeed the dip of the subducting interface is steeper north of the suture and shallower south of the suture as given by earthquake locations (Figure 2.2; (*Newman et al.*, 2002; *Norabuena et al.*, 2004)). In particular, earthquakes occurring north of the EPR-CNS suture are about 5-10 km deeper as compared to earthquakes occurring south of the suture (*Newman et al.*, 2002). In addition, earthquakes that occur on the EPR crust locate about 10 km farther from the Middle America Trench (MAT) as compared to earthquakes occurring on CNS crust (*Newman et al.*, 2002).

Several large historic earthquakes occurred near the Nicoya Peninsula and the Gulf of Nicoya. In 1950, a magnitude 7.7 occurred near the central portion of the Nicoya Peninsula (*Güendel et al.*, 1989; *Marshall and Anderson*, 1995). From interviews recorded by *Marshall and Anderson* (1995) the earth-

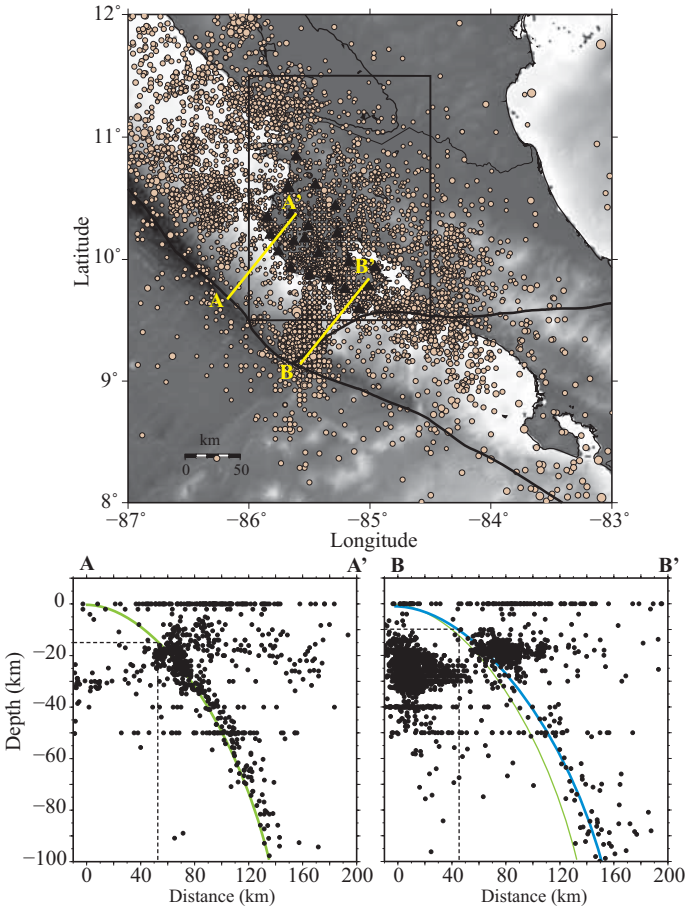

Figure 2.2:
Earthquakes recorded between December 1999 - March 2001 (light brown circles) along the Cocos-Caribbean margin at Costa Rica. Earthquakes selected for this study are bounded by the black box. Two cross-sectional profiles (A-A',B-B') in the direction of subduction for the EPR and CNS formed crust are shown in the two lower panels. The A-A' profile shows the dip of the plate interface of the EPR crust (green curve) as given by earthquake locations. The seismicity starts at about 47 km from the trench and at depth of about 15 km (dashed lines). Earthquake locations in the B-B' profile outline the dip of the interface of the CNS crust (blue curve). Shown for comparison is the CNS interface dip (thinner green curve). Here the seismicity initiates at about 43 km from the trench and at depth of 10 km (dashed lines).

quake caused liquefaction, landslides and a sudden drop in sea level. Since 1950, the sea level has been rising, suggesting that the central region of Nicoya peninsula is subsiding during this interseismic period (*Marshall and Anderson*, 1995) and thus is locked. In 1978, a M_s 7.0 earthquake occurred south of the 1950 earthquake (*Marshall and Anderson*, 1995; *Avants et al.*, 2001), however, I have not found much information about this event. In 1990 a large, M_w 7.0, earthquake occurred at the entrance to the Gulf of Nicoya (*Protti et al.*, 1995) and has been associated with fracturing of or near to a subducted seamount (*Husen et al.*, 2002).

2.3 Topography and bathymetry

The Cocos plate is generally flat at the northern end of the peninsula and laden with seamounts at the southern tip of the peninsula (Figure 1.2). To the south of the EPR-CNS suture, the trench slope is indented and rough in response to the subduction of seamounts (*Hinz et al.*, 1996; *Scholz and Small*, 1997; *Dominguez et al.*, 2000; *von Huene*, 2008). The height of the seamounts south of the EPR-CNS suture varies from about 2 to 2.5 km (*von Huene*, 2008). The Costa Rica forearc deforms in response to the subduction of these features (*Ye et al.*, 1996; *Gardner et al.*, 2001), as well as subduction of the dense, low relief crust formed at EPR (*Marshall and Anderson*, 1995).

2.4 Deformation

Near the southern tip of the Nicoya Peninsula shoreline, GPS data collected in 1995, 1996 and 1997 show continuous subsidence, while the inland region is uplifting (*Lundgren et al.*, 1999). *Lundgren et al.* (1999) describe this

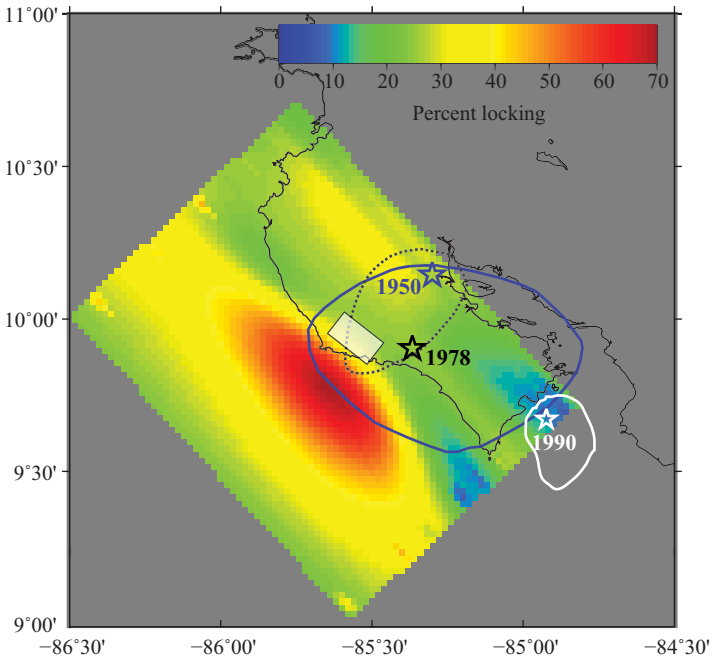

Figure 2.3:
The highest amount of interface locking percentage occurs at the central point of the peninsula, near the subduction of the EPR-CNS suture (data from *Norabuena et al.* (2004)). The white box represents the highest locking patch from the GPS study of *Lundgren et al.* (1999). Also shown are the rupture areas of large historic earthquakes with their locations (stars), and rupture areas (polygons).

deformation as characteristic of an interseismic cycle. The GPS survey data from *Lundgren et al.* (1999) and *Norabuena et al.* (2004) have highly variable resolution due to station coverage, but both suggest a locked patch near the central part of the Nicoya peninsula, approximately in the area where the EPR-CNS suture is subducting (Figure 2.3). *Marshall and Anderson* (1995) analyzed the ages, sea level changes and uplift rates of terrace formations along the southern tips of the Nicoya peninsula, and concluded that since the late

Holocene this part of the peninsula is rotating and tilting arcward at 0.01°-0.02°/k.y.

CHAPTER 3

DATA

The data for this project was collected on a seismic network deployed on Nicoya Peninsula as a part of the 1999-2001 Costa Rica Seismogenic Zone Experiment (CR-SEIZE) project (Figure 2.2). Through the project duration, 23 land based stations and 14 ocean bottom seismometers recorded small magnitude earthquakes in the region (*DeShon et al.*, 2006). Earthquakes recorded during CR-SEIZE were used to examine the fauting mechanisms of recorded data (Figure 3.1, *Hansen et al.* (2006)), the seismogenic updip limit variation across the EPR-CNS suture (*Newman et al.*, 2002), and *b*-value distribution along-strike of the trench (*Ghosh et al.*, 2008). With the exception of one cluster representing strike-slip faulting, the focal mechanisms for individual and clustered events represent underthrusting faulting along the interface (*Hansen et al.*, 2006). As long as the coda calibration results were well constrained, I have used earthquakes with both faulting mechanisms in the analysis.

Because the peninsula lies so close to the trench, the instruments provided me with excellent data focused at the interface between the Cocos and Caribbean Plates (Figure 3.2). The data I selected from the CR-SEIZE database consisted of events that located within 10 km of the subduction plate interface and up to a depth of 50 km. The 50 km depth cutoff was chosen to capture the seismicity near the locked part of the subduction zone inter-

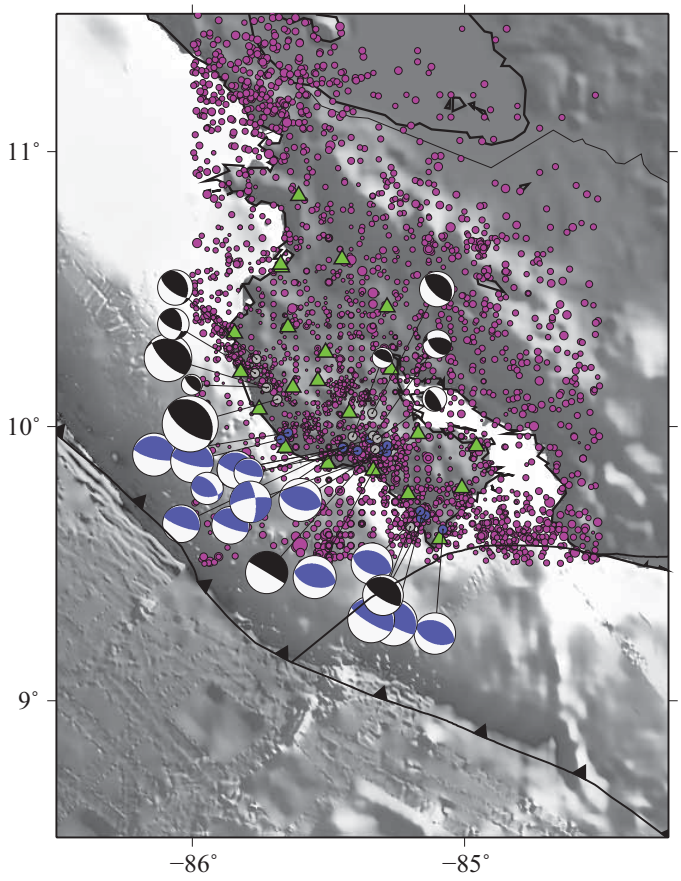

Figure 3.1:
Shown are earthquakes selected from the CR-SEIZE used in this study (purple circles), station locations (green triangles), focal mechanisms (*Hansen et al.*, 2006) for individual events (black compression quadrants) and clusters (blue compression quadrants) and the event locations (gray circles for individual events, blue circles for clusters). Out of the selected CR-SEIZE events, 353 earthquakes were used for apparent stress analysis.

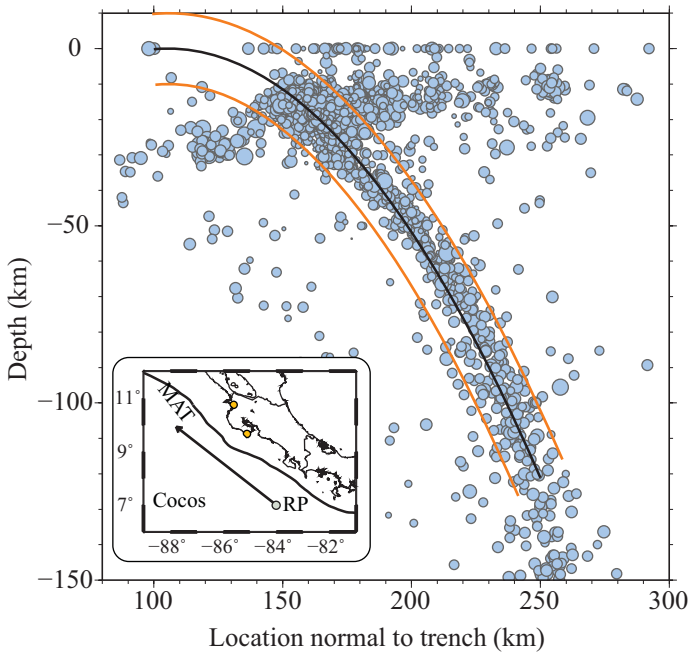

Figure 3.2:
Earthquake selected from CR-SEIZE database located within 10 km of the subduction zone interface. Shown are the *a priori* fit (black solid line), boundaries at 10 km above and below the interface (orange solid lines), and earthquake locations (blue circles) rotated 52^o W of N using pole at 84^{o}W and 7^{o}N (gray circle, insert). The insert also shows the direction of earthquake rotation. The orange circles are the locations of stations PNCB and COND that were used to further limit the data.

face. Initially, all CR-SEIZE earthquake locations were rotated 52^o west of north from a pole at 84^{o}W and 7^{o}N (Figure 3.2 insert). Then the subducting plate interface was determined as an *a priori* fit to the earthquake locations. Thereafter, I used a simple parabolic function that extended 10 km above and below the interface to capture all events within it. In addition, the earthquakes were constrained by the location of stations PNCB and COND, which, when rotated, formed the south and north edges of the seismic network. Finally,

during the processing steps the events had to locate geographically within an area bounded by 9.5^{o}N, 11^{o}N, 86^{o}W and 84.5^{o}W, because these events would be well sampled by the land network. This was all done to use only those events that were located well within the station network.

I used data from the land-based seismometers only due to better signal-to-noise ratio (SNR). The land based instrument pool consisted of short-period and broadband seismometers. After the first few calibration runs, one of the stations (VIMA) showed amplitude spectra 2 orders of magnitude higher than the rest of the network. I assumed that this behavior was due to inappropriate instrument response and removed the data from this station from my data pool. The rest of the seismometers sampled generally at 40 samples per second (40 Hz). However, there were some exceptions, in which the instrument initially sampled at 20 Hz and switched later to 40 Hz. Ultimately, this sampling rate constrained the usable frequency range of the earthquake data. All of the used data was in SAC (Seismic Analysis Code) format.

There are 353 earthquakes within the selected region that were calibrated and well constrained out of 1350 processed events. Their magnitude ranges from 0.8 to 4.2 M_L, where M_L is computed as a high frequency body wave measurement using the Antelope database package. The earthquake waveforms were cut from a continuous database based on the pre-existing P wave arrival (using picks refined by relocations from velocity model of *DeShon et al.* (2006)). The start of the waveform files was set to 20 seconds before the P-wave arrival, and the total length of the data was 200 seconds. The selected waveforms vary in quality due to the event size and distance from the network or individual sta-

tion (Figure 3.3). Both earthquakes in Figure 3.3 located approximately in the same location near station MARB and provided me with well constrained results. However, due to the 2 order of magnitude difference between them there is a displacement signal amplitude difference of more than 100 nm at MARB. The smaller event of December 15, 1999 was not recognizable at station BANE.

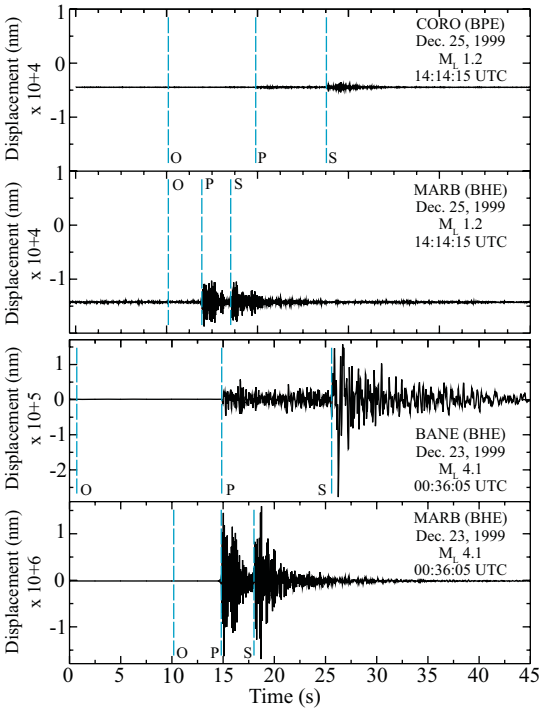

Figure 3.3:
Earthquake waveforms plotted in SAC. Top two panels show a M_L 1.2 earthquake that occurred on December 25, 1999 at 14:14:15 UTC recorded at stations BANE and MARB. Bottom two panels show a M_L 4.1 earthquake that occurred on December 23, 1999 at 00:36:05 UTC recorded at stations CORO and MARB. Both events locate very close to MARB. The body wave arrivals (P and S) and the origin times (O) are shown in all panels.

CHAPTER 4

METHODS

Using earthquake coda amplitudes instead of body wave amplitude has been shown to provide more stable interstation amplitude measurements due to the averaging properties of coda over the path and the source radiation (e.g. *Chouet et al.*, 1978; *Rautian and Khalturin*, 1978; *Phillips and Aki*, 1986; *Eken et al.*, 2004; *Malagnini et al.*, 2004; *Mayeda et al.*, 2005; *Malagnini et al.*, 2006). *Phillips and Aki* (1986) model coda wave amplitude in order to determine and remove site effects from the signal and improve amplitude stability for a set of earthquakes recorded in central California. In order to model the crustal attenuation in Turkey, *Eken et al.* (2004) used only three broadband stations that recorded earthquakes with epicentral distances up to 1400 km. They confirm the validity of their results by comparing the M_w given by coda to M_w from studies using body waves. *Malagnini et al.* (2004) and *Malagnini et al.* (2006) used the stability of coda amplitudes to estimate site effects for broadband stations using 206 earthquakes in northern Italy and 200 aftershocks from the M_w 7.6 earthquake in western India, respectively. In both cases, the measured coda amplitudes from all events had less scatter between the stations than the body wave amplitudes.

The complicated tectonic setting of Nicoya Peninsula makes the earthquake coda amplitude method a better choice over traditional body wave meth-

ods for this study. Because the body wave amplitude is affected by path heterogeneities and source radiation, the variable crustal structure of the subducting Cocos Plate, and the margin wedge geological structure could cause large differences in amplitudes between the stations for events with similar magnitude range as mine. In order to determine the variations in σ_a along-strike of the subduction zone, I needed a stable source amplitude estimates.

The data processing was done in three distinct steps following the method of *Mayeda et al.* (2003) and *Phillips et al.* (2008). At first I created narrow-band frequency envelopes from the coda of the displacement seismograms using the horizontal components of motion. Next, I picked the peaks and the lower end of the coda envelopes and computed coda shape functions from which coda amplitude was measured. Thereafter, I corrected the measured amplitudes for path and site effects and obtained transfer function to shift corrected amplitudes to absolute units using events with waveform modelled seismic moments. At last I used the corrected amplitudes to calculate seismic moment, corner frequency, and apparent stress for all calibrated events. Flowchart representation of this process is shown in Figure 4.1 (adopted from *Phillips et al.* (2008)).

4.1 Narrow-band frequency envelopes

As the shape of earthquake coda is strongly frequency-dependent, which *Mayeda and Walter* (1996) attribute to changes in scattering, anelastic processes or crustal structure, the original signal is split into narrow-band frequency envelopes. In order to create the narrow-band frequency envelopes, I needed the earthquake displacement seismograms and their corresponding

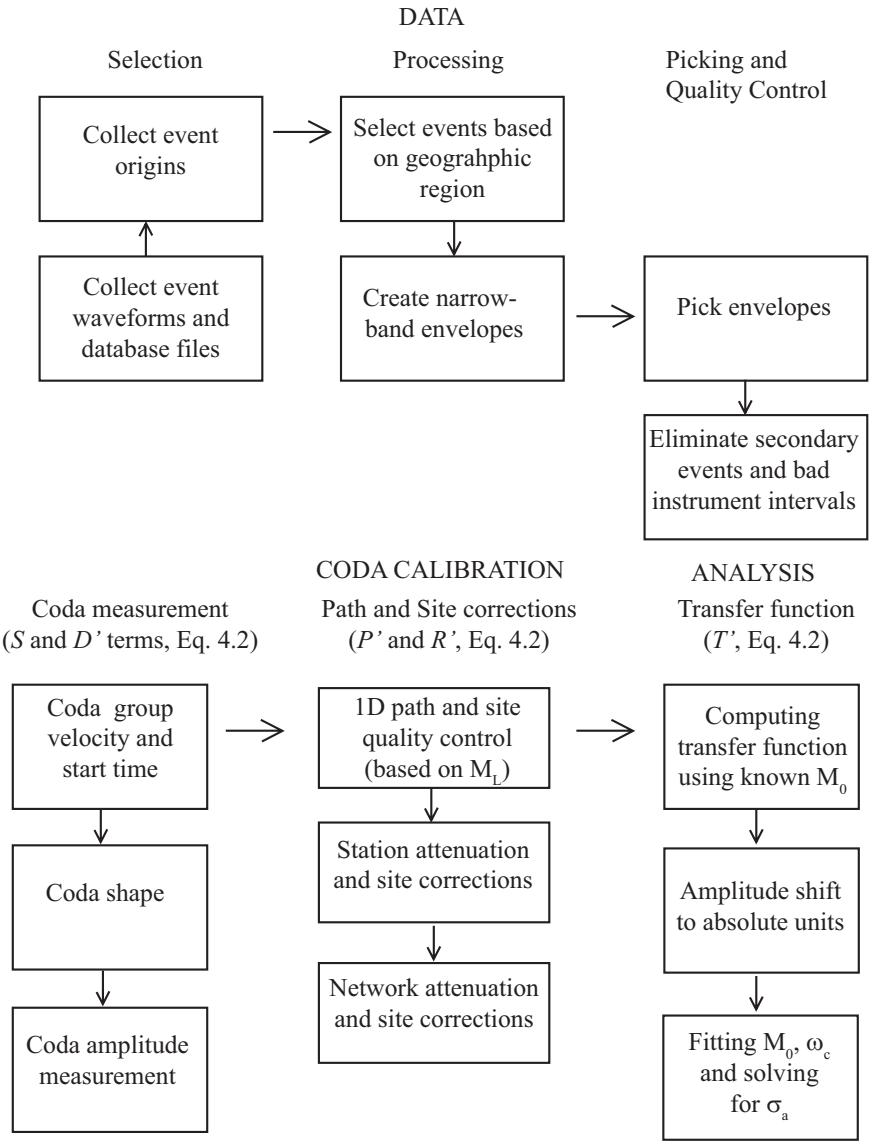

Figure 4.1:
Flowchart of data processing and coda calibration

database files. The earthquake seismograms were organized based on julian date of the earthquake origin, and the event identification number. The database files contained information about the instruments and individual earthquakes, such as event and origin identification numbers, station and event locations, and the response files for each station.

The envelopes were created for each selected earthquake and station pair for a range of narrow-band frequencies. After removing the mean from the earthquake seismograms and tapering them, I removed the instrument response and transformed the data into velocity units. Then, the data was filtered using Butterworth (4 pole, 2 pass) filters. The envelopes for each frequency band were formed as a sum of the filtered velocity signal and its Hilbert transform (*Mayeda et al.*, 2003):

$$E(f,t) = \sqrt{v(t)^2 + h(t)^2}, \tag{4.1}$$

where t is time from origin, v(t) is the signal converted to velocity, and h(t) is the Hilbert transform of the signal. The frequency range of each band, corresponding smoothing width and interpolation interval are given in Table 4.1. The envelopes were rotated into radial and transverse components, stacked and averaged. In the final step, the modified envelope information was placed into the SAC headers.

4.2 Picking process

Once I created the narrow-band frequency envelopes, I picked the coda envelope end times manually using SAC and the coda envelope peak times using an autopicking program in SAC. The coda end picks were placed

Table 4.1: The smoothing width and interpolation intervals were functions of frequency. From the original Mayeda bands (e.g. *Eken et al.*, 2004) I added bands above 2 Hz in order to constrain corner frequency and amplitude decay at higher frequencies.

Frequency (Hz)	Smoothing width (s)	Interpolation interval (s)
0.5 - 0.7	7.0	3.0
0.7 - 1.0	7.0	3.0
1.0 - 1.5	4.0	2.0
1.5 - 2.0	4.0	2.0
2.0 - 3.0	2.0	1.0
3.0 - 4.0	2.0	1.0
4.0 - 6.0	2.0	1.0
6.0 - 8.0	2.0	1.0
8.0 - 10.0	2.0	1.0
10.0 - 13.0	2.0	1.0
13.0 - 16.0	2.0	1.0
16.0 - 19.0	2.0	1.0

where coda envelope signal was close to its minimum amplitude, yet still above the background noise level (Figures 4.2 and 4.3). In addition I picked the signal at the bottom of a slope of steepest decaying amplitude. Then, based on the coda end picks, I run a SAC autopicking program to place picks at the maximum amplitudes. I used the SAC built-in function *markp* to place a marker at maximum amplitude after the S wave arrival time and before the coda end pick. In cases where there was no S wave arrival pick, the S wave time was approximated using the epicentral distance and S-wave velocity of 4.6 km/s. If there was no manual coda end pick (e.g. bands with low SNR, events with undefined magnitude or events deeper than 50 km), the frequency band was ignored by the subsequent processing. After all of the frequency envelopes

were picked, the peak times were converted to group velocities and were stored for use in the final coda calibration procedure. There was a large difference in usable coda window length between small and large events (Figures 4.2 and 4.3), which had an effect on the choice of coda amplitude measurement time in the calibration process.

The coda peak amplitudes were used to determine the coda peak group velocity and coda start time. The coda end picks were used in determining where the source amplitude will be measured. I have tested the dependence of the source spectra results on different coda peak times by adding few seconds to the automated coda peak time. I run the calibration using just the coda peak time, coda peak time + 3 seconds, and coda peak time + 5 seconds. Using just coda peak time to estimate the coda peak group velocity resulted in poor source parameter fits of earthquakes with independent seismic moment estimates. Using the coda peak time + 3 seconds and coda peak time + 5 seconds improved the fits significantly, with coda peak time + 3 seconds providing the smallest residuals. Therefore, this adjustment was applied in the group velocity estimates.

In the following processing, I assigned frequency dependent variables coda start, coda maximum duration and coda amplitude measurement time. The coda amplitude is measured within the coda windows chosen by the analyst. The coda window is spans over time domain bounded by coda start and coda maximum duration. I selected the coda start to be 5 seconds after the coda origin for each band, where coda origin is determined using the coda peak group velocity and epicentral distance. The coda maximum duration boundary

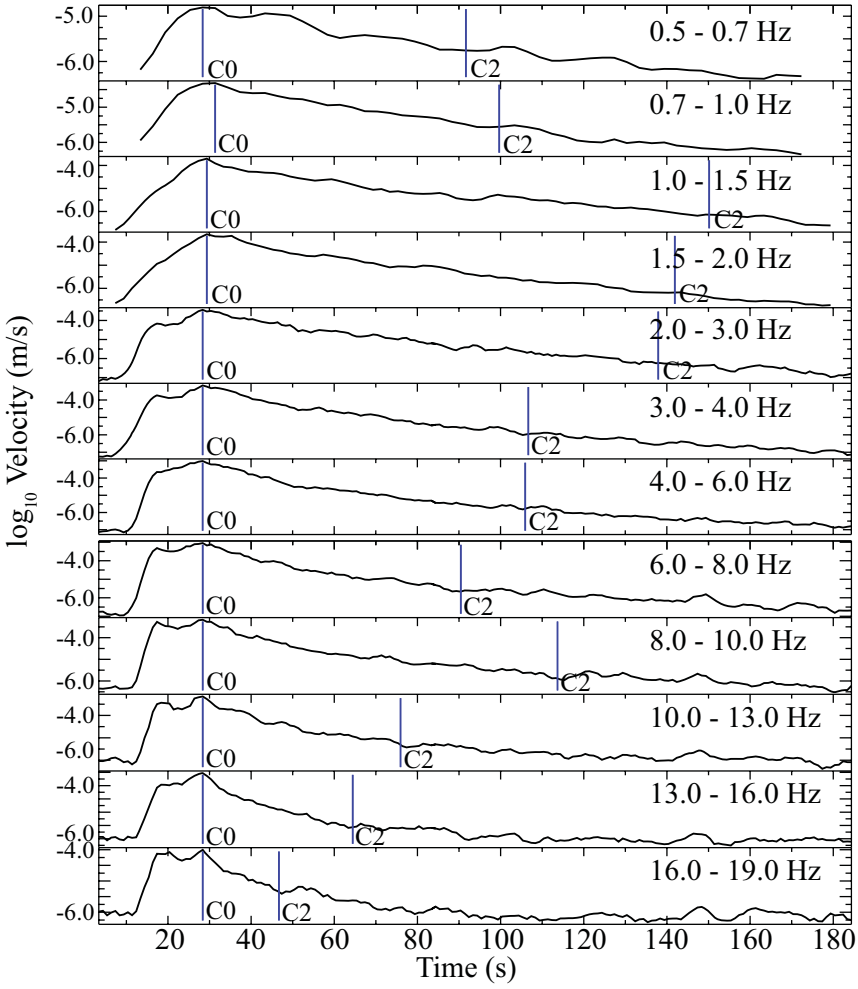

Figure 4.2:
Shown are the narrow-band frequency envelopes for the earthquake shown in Fig. 3.3, bottom panels, recorded on station BANE. The C0 and C2 markers represent the coda peak and coda end picks (emphasize with blue solid lines), respectively. This earthquake has M_L 4.11 (event ID 2963, Table A.1) and occurred on December 23, 1999 at 00:36:05 UTC.

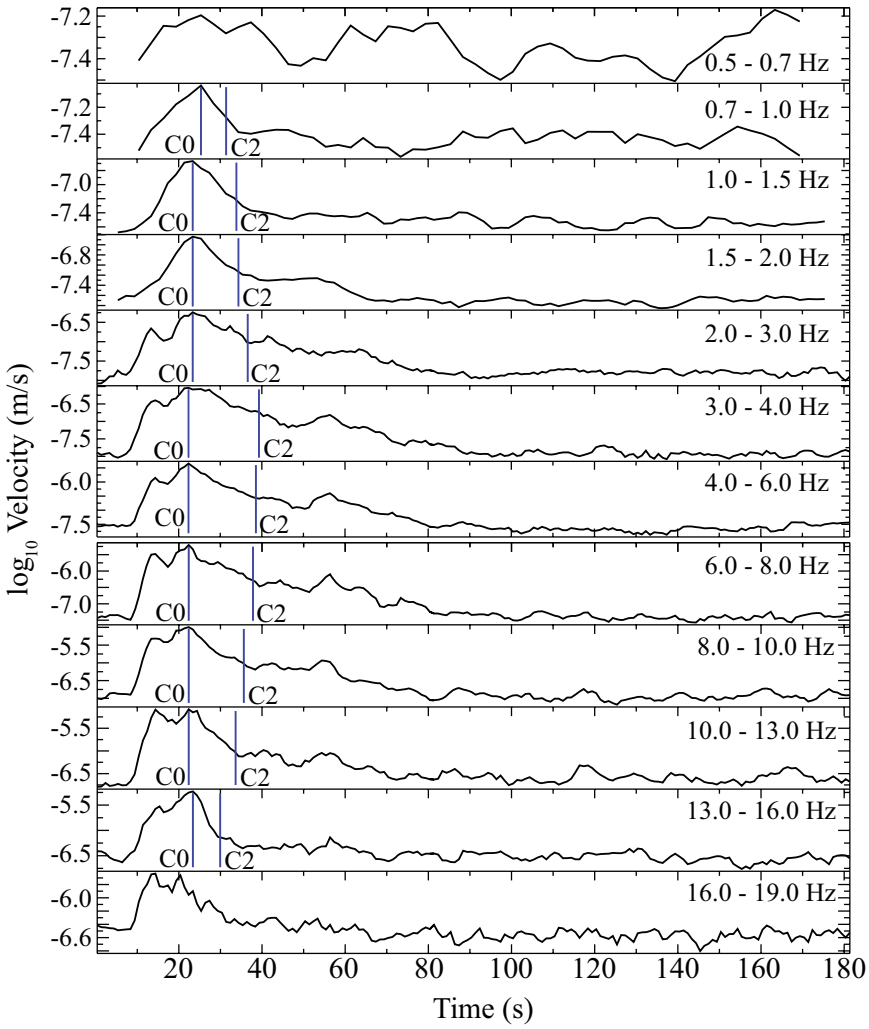

Figure 4.3:
Shown are the narrow-band frequency envelopes for the earthquake with M_L 2.02 (event ID 18903, Table A.1) that occurred on November 27, 2000 at 09:42:20 UTC. Also shown are the coda peak (C0) and coda end (C2) picks emphasized with blue solid lines. Frequency bands 0.5-0.7 and 16-19 Hz were not picked due to very noisy signal. At 0.5-0.7 Hz there is no visible coda signal, and at 16-19 Hz coda envelope is visible but noisy.

varies between frequency bands and is shown in Table 4.1. The measurement time is the time at which the program interpolates the coda amplitude using calibrated shape envelopes, and is selected within 5-15 seconds of the coda maximum duration time (Table 4.3).

4.3 Coda calibration

In order to get the true source amplitude spectrum, the measured coda amplitudes for each band had to be corrected for geometrical spreading, site effects, attenuation, and the transformation from S waves to coda (*Walter and Taylor*, 2001; *Mayeda et al.*, 2003; *Phillips et al.*, 2008). *Phillips et al.* (2008) expressed the coda amplitude in frequency domain as

$$A_{ij}(f) = S_i(f)T(\phi_i, \theta_i, f)P'(\phi_i, \theta_i, \phi_j, \theta_j, f)R'_j(f)D'_j[x, f, t_c(x, f) + t_m(f)] \tag{4.2}$$

where f is frequency, i and j are the source and receiver indices, ϕ is latitude, θ is longitude, and t_m is the measurement time of coda amplitude with respect to coda origin time, t_c. S is the source amplitude spectra that I am ultimately solving for, T' is the source-to-coda transfer function, P' represents path effects, R' is the site term, and D' represents the coda decay function. The primed factors represent dimensionless terms (*Phillips et al.*, 2008).

The corrections to coda amplitude (term A, Eq. 4.2) were done in several steps (Figure 4.1) described in the following sections. I briefly outline them here. To measure the coda amplitude, I needed the coda group velocity, coda start time, and the spreading and attenuation terms affecting the shape of the envelope. At first, I estimated the S-wave coda peak group velocity

and origin time using the automated coda peak picks. Using the coda group velocity, coda start time, and initial guess for the envelope shape parameters, I calculated the shape functions from which I interpolated coda amplitudes (term *D'*, Eq. 4.2). At this point I performed a quick quality control of the interpolated coda amplitudes using the earthquake original magnitude, M_L, and a model of the path effects on the amplitudes *Taylor and Hartse* (1998). The path and site corrections were applied then to the measured coda amplitude. Here I specified geometrical spreading using the Street-Herrmann model (*Street et al.*, 1975). Then I inverted for path propagation effects, which were done at first for individual stations and 1-dimensional distance propagation, and recalculated later for laterally varying attenuation and site terms of the whole network (terms *P'* and *R'*, Eq. 4.2). In the last calibration step, I computed a transfer function to shift amplitudes to the absolute units using events with known seismic moments (term *T'*, Eq. 4.2).

Once all of the interpolated coda amplitudes were calibrated, I could proceed with the analysis. Seismic moment, corner frequency and apparent stress values were calculated following the method of *Walter and Taylor* (2001). Initially, apparent stress was held constant at 1 MPa and I solved for seismic moment and corner frequency. This gave me a reasonable values for two of the three unknown parameters. I used the solutions as initial guess and inverted in the final step for seismic moment, corner frequency and apparent stress.

4.3.1 Coda measurement step

Coda group velocity and origin time

To determine a coda shape and from it measure the coda amplitude, I needed the coda origin time. The coda origin time was calculated using the coda group velocity. The group velocity (v_g) was estimated from the automated coda peak picks. The group velocities increase steeply at short distances, until they reach an asymptote at longer distances. A hyperbolic distance dependent function was fit through all of the coda peak picks for every frequency band in order to solve for v_g of that particular band. The hyperbolic function is as follows (*Mayeda et al.*, 2003):

$$v_g(dist, f) = v_0(f) - \frac{v_1(f)}{v_2(f) + dist}, \tag{4.3}$$

where *dist* is the epicentral distance, *f* is the center frequency for each band, and *v0*, *v1*, and *v2* are constants (*Mayeda et al.*, 2003) that are estimated using grid-search method. In this study I minimized the residuals using modified Powell's minimization method (L_1 fit, (*Press et al.*, 2007)). The resulting v_g approaches zero near zero distances and approaches peak S_g at the asymptote, providing us with reasonable v_g estimate (Figure 4.4). At low frequencies (bands 0.5_0.7, and 0.7_1.0) I had limited data at short distances, but the fit improves for all distances with increased data quantity for frequency bands above 1.0 Hz.

As the stations in the CR-SEIZE network on Nicoya Peninsula are closely spaced, I grouped all of the stations together to estimate the v_g. In all of the other processing steps, calibrating parameters are allowed to vary by station (except for HOJA). Station HOJA changed the recording channel through the experiment, thus I choose to constrain it the same as station GUAI.

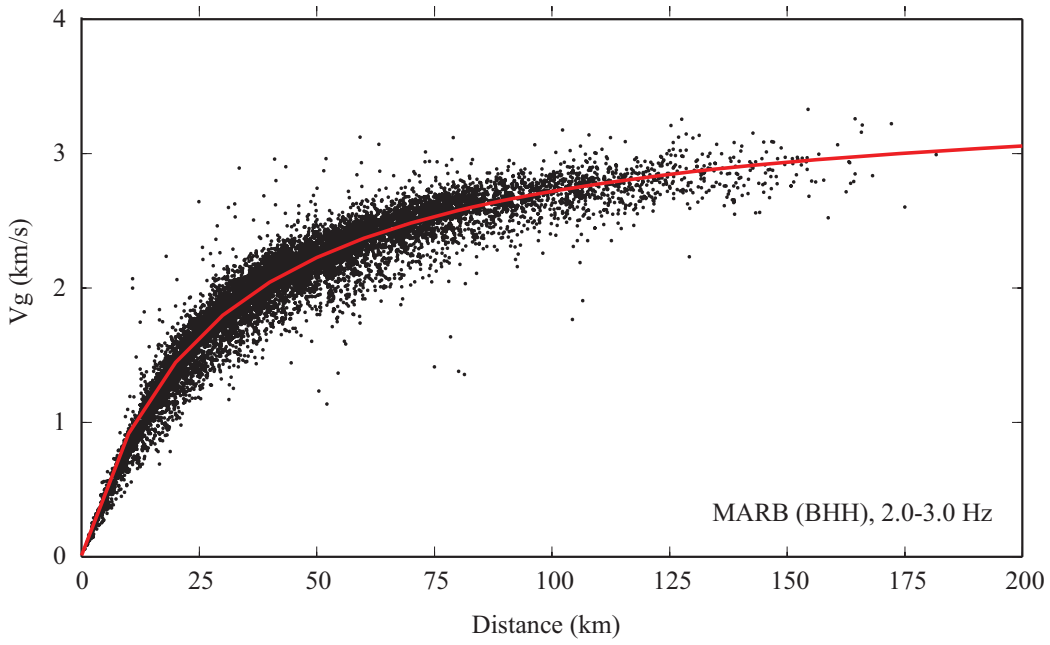

Figure 4.4:
This is the fit of the hyperbolic model of coda group velocity (solid line) to the coda peak velocity picks (black dots) for frequency band of 2-3 Hz. Each black point plotted in this figure represents coda peak velocity from one event-station pair picked in this frequency band. At this frequency, the fit is very good up to about 180 km.

In this v_g step, I selected one station (broadband station MARB) as a master station, which means that velocity constraints applied to this station will be the same for all of the other stations in the group. I used MARB as a master because of its central location and abundance of data. In previous calibration runs, I computed the coda peak velocity using each station as its own master. However, several stations lack data at short distances and thus their coda peak velocity estimates were not well constrained. Estimated v_g at epicentral distance range between 0 and 100 km for frequency bands 2-3 and 13-16 Hz

are shown in Figure 4.5. The coda peak v_g computed for individual stations are shown with the solid lines for several selected stations. The coda peak v_g computed for all stations together is shown with the dashed line. Using master station provided better estimate of v_g for the 2-3 Hz frequency band (Fig. 4.5, panel a). In the 13-16 Hz band, using individual stations resulted in smaller average residuals (Fig. 4.5, panel b), but the v_g estimated using master station still fits reasonably well.

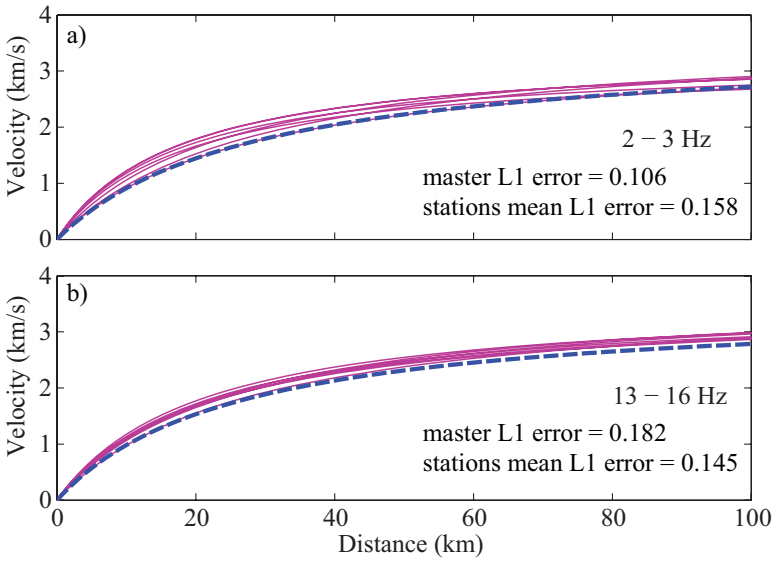

Figure 4.5:
Estimates of v_g computed using individual stations (solid lines) and a master station (dashed line), with errors calculated using L1-norm minimization for 2-3 Hz (a) and 13-16 Hz (b).

Coda shape

Mayeda et al. (2003) developed an analytic expression for synthetic coda shape models to fit the narrow-band frequency envelopes using distance dependent parameters (representing attenuation and spreading), b and γ,

$$A(f,t,r) = H(t - \frac{r}{v(r)})(t - \frac{r}{v(r)})^{-\gamma(r)} \exp[b(r)(t - \frac{r}{v(r)}], \tag{4.4}$$

where H is the Heaviside step function, the t is time from origin, r is the epicentral distance, *v(r)* is the coda peak group velocity. The γ-term controls the early coda shape, while the b-term accounts for the attenuation. Both, γ and b are distance dependent and calculated using frequency dependent parameters that fit a hyperbolic function, similar to Eq. 4.3:

$$b(r,f) = b_0(f) - \frac{b_1(f)}{b_2(f) + r}, \tag{4.5}$$

$$\gamma(r,f) = \gamma_0(f) - \frac{\gamma_1(f)}{\gamma_2(f) + r} \tag{4.6}$$

where *b0*, *b1*, *b2*, γ_0, γ_1, γ_2 are further cubic functions of frequency.

To obtain the coda shape terms, γ and b, I needed an initial estimate for the constants of the frequency dependent cubic function used to compute *b0, b1, b2* and γ_0, γ_1, γ_2 parameters. At first I used a model from the results of *Phillips et al.* (2008). Thereafter I set my latest shape function results as an initial guess for the model (Table 4.2). Prior to inversion I grouped data using a radial grid. Initially the region around the station is divided into 25 radial and 24 azimuth bins up to a maximum radial distance of 500 km. The azimuth bins are 15 degrees wide, the width of radial bins (*radius*) is determined by a power law function, where individual intervals are related as follows:

$$radius(i) = radius(1) * 10^{(a0*(i-1))}, \tag{4.7}$$

Table 4.2: Constants used to calculate the frequency dependent cubic functions *b0, b1, b2*, γ_0, γ_1, γ_2 used in Eqs. 4.5 and 4.6 to compute γ and b at station MARB.

Term	A	B	C	D
b0	-2.40565	1.03745	0.474829	-2.46110
b1	0.536041	0.430991	-0.599962	6.44710E-02
b2	2.67596	0.421917	-1.88122	0.654617
γ_0	-2.25903	3.51954	-1.33220	-0.843824
γ_1	1.65074	0.362510	0.320431	-0.175128
γ_2	1.97147	-2.49060E-02	0.497805	-0.227884

here *a0* is obtained by a minimization procedure based on the desired number of bins and outside radius.

I selected the best events in each grid for the model inversion. The events are selected based on the type of the coda end picks (manual vs. automatic), coda length, and magnitude in that order. In cases that a given grid did not have an event with manual pick, I applied an autopicking algorithm to the trace. The main constraint with such events was that their signal had to be at least 4 times the noise level to be processed. The results, which are the new cubic function constants and the *b0, b1, b2*, γ_0, γ_1, γ_2 terms, were obtained using grid search technique. The fit between the data and the resulting coda shapes is determined using an L1 minimization.

The results are shown in Fig. 4.6. I have used frequency band 1.5-2 Hz of the M_L 4.11 earthquake (from Dec. 23, 1999 at 00:36:05 UTC) to show the fit of the synthetic coda shape to the coda envelopes (Fig. 4.6, top two panels), and frequency band 3-4 Hz of the M_L 2.56 earthquake (from Jul. 12, 2000 at 19:50:08) both recorded at stations COND and MARB (Fig. 4.6). Note

that I am only fitting the shape of the coda here, not the amplitude. To fit the amplitude as well, the synthetic data needs to be corrected for the path and site effects (*P'* and *R'*) and shifted using the transfer function (*T'*, Eq. 4.2), described in the following sections.

Coda amplitude measurement

Using coda decay variables (*b*-term and γ), I can estimate the coda amplitude. The coda amplitude shape is adjusted for γ and *b*-term at each data point within the measurement window to get the coda amplitude. Then, I estimated the median from the adjusted amplitude data. The scatter between the amplitude data and the median is determined using root-mean square method (L_2 fit). The coda amplitude used for further processing is measured at the lower end of the coda shape fitted window (at time t_m given for each frequency in Table 4.3.

4.3.2 Path and site corrections

The amplitude of seismic waves recorded by a seismic network is affected by spreading, attenuation, and frequency dependent site effects (*Walter and Taylor*, 2001). In addition, to obtain a source amplitude I had to account for the efficiency of S wave change to coda. To estimate the source amplitude, I had to invert for and remove these effects from our amplitude data. This was done in several steps. At first I estimated the S-wave source amplitude using the earthquake magnitude (*Taylor and Hartse*, 1998), obtained starting Q and site terms, and removed outliers for each band. Then I inverted for site effects and 1-D Q for each band based on relative amplitudes for each event. Again

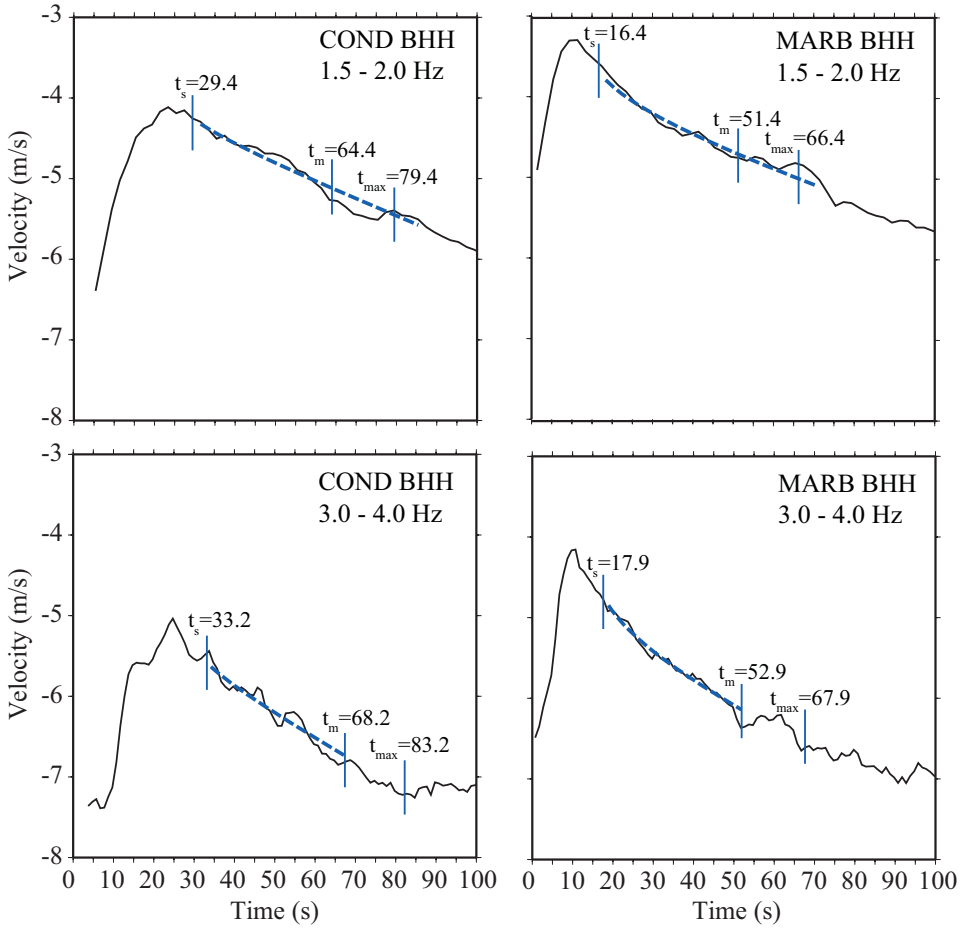

Figure 4.6: Coda shape fit

Coda shape functions (dashed lines) for frequency bands 1.5-2 and 3-4 Hz from stations COND and MARB plotted against the coda envelopes (solid lines). Also shown are the boundaries for coda measurement window, t_s, t_m and t_{max} that are described in the next section.

Table 4.3: This is a list of coda window parameters used to determine the amplitude measurement position. All of the times are relative to the coda origin time, which is frequency dependent.

Frequency band (Hz)	tstart (s)	tmax (s)	tm (s)
0.5 - 0.7	5.0	55.0	40.0
0.7 - 1.0	5.0	55.0	40.0
1.0 - 1.5	5.0	55.0	40.0
1.5 - 2.0	5.0	55.0	40.0
2.0 - 3.0	5.0	55.0	40.0
3.0 - 4.0	5.0	55.0	40.0
4.0 - 6.0	5.0	55.0	40.0
6.0 - 8.0	5.0	45.0	35.0
8.0 - 10.0	5.0	45.0	35.0
10.0 - 13.0	5.0	40.0	30.0
13.0 - 16.0	5.0	40.0	30.0
16.0 - 19.0	5.0	30.0	25.0

I removed outliers for each band. Next I used the resulting site effects and inverted for Q using relative amplitudes for each event over a 2D great circle arc grid. In both steps, I estimated the spreading model and applied it to the predicted data.

Source scaling and magnitude for initial attenuation analysis

The effects of propagation on the measured amplitude were estimated using *Taylor and Hartse* (1998) method. I used magnitude (M_L, from database files) and center frequency (f) for each event-frequency band combination to estimate the P- and S-wave source amplitudes and corner frequencies. The magnitude was used to calculate the low-frequency spectral level (S_0), which

for an Lg coda is given by (*Taylor and Hartse*, 1998):

$$S_0 = 1.4 * mb - 10.4 \tag{4.8}$$

where in this study mb is the original M_L. From S_0 I computed the P- and S-wave corner frequencies (ω_P, ω_S) as:

$$\omega_S = 0.18 * 10^{(-0.25 * S_0)}, \tag{4.9}$$

$$\omega_P = 1.7 * \omega_S, \tag{4.10}$$

where the constant 1.7 is the V_p/V_s ratio. Using S_0 and the P and S corner frequencies, I calculated the S-wave source amplitude as:

$$S_c = S_0 - \log(1.0 + f^2/\omega_S^2), \tag{4.11}$$

where f is the center frequency in a given frequency band.

Path and site corrections

Next I inverted for path corrections, using the source corrected coda amplitude, initial guess for Q (400), and the Street-Hermann spreading model, which is fully described by *Street et al.* (1975). The initial Q guess corresponds roughly to the value of Q at 11 Hz using coda Q results from *Gonzalez and Persson* (1997), who expressed shear wave coda attenuation for the Nicoya Peninsula in terms of frequency dependent Q:

$$Q = 115 f^{0.52} \tag{4.12}$$

where f is frequency. The Street-Hermann spreading model accounts for spreading at local and regional distances as given by:

$$a(x) = x^{-\alpha_1}; x \leq X_0 \tag{4.13}$$

$$a(x) = X_0^{-\alpha_1} \frac{x}{X_0}^{-\alpha_2}; x \geq X_0 \tag{4.14}$$

where *a(x)* is the spreading function, α_1 and α_2 are short and long distance spreading coefficients (0.01 and 1 respectively), and X_0 is the cross-over distance (1000 km). Because the farthest of my selected eartquakes locate at about 200 km from the stations, I am using only the flat spreading for local distance (Eq. 4.13).

At first, I weighted amplitudes inversely with distance. Then, I predicted what the amplitudes should be by adding site and spreading terms and subtracting attenuation. The difference between the observed and predicted data before and after the inversion was minimized using L1.2 method. The L1.2 method is similar to L2-norm in that I sum up the differences between the observed and predicted values. It differs in that the individual terms are raised to 1.2 power (and consequently the resulting sum is raised to -1.2 power), which should deal with the median data values better (W. S. Phillips, personal communication, 2008). During the inversion process, the model was solved for using the Powell technique again (*Press et al.*, 2007). The path corrected amplitudes show relatively large scatter about the fitted curve (Figure 4.7), which could be due to errors in original magnitudes. Only corrected amplitudes with residuals between -1.5 and 1.0 were saved for further processing.

Attenuation correction, 1-D and 2-D

In the previous step, I solved for site terms with an initial Q estimate. In this step, I solve simultaneously for site terms and Q based on amplitude differences with no M_L-based source corrections. In this step, the number of

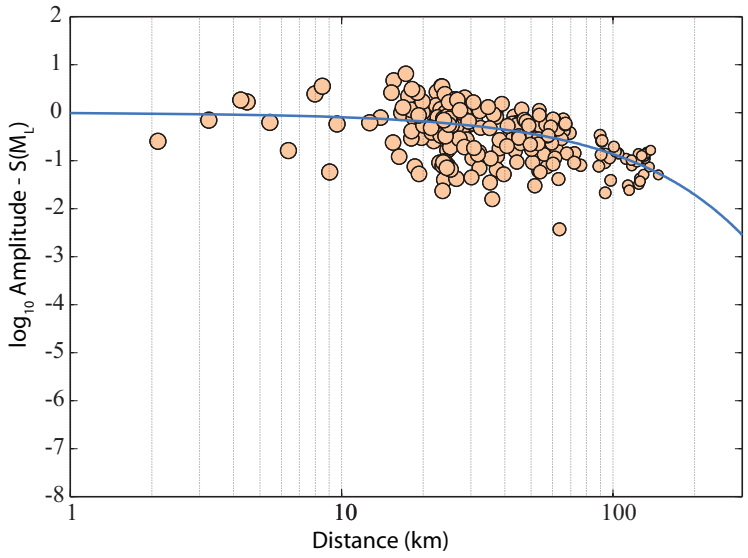

Figure 4.7:
The coda amplitudes were corrected for the source based on the original M_L following method of *Taylor and Hartse* (1998). The corrected amplitudes (solid circles) are weighted with distance to improve fit at short distances. The solid line represents the path model fit. The scatter in the corrected amplitudes may suggest that there are errors in the original magnitude estimates.

model parameters is the sum of the site and Q terms (one site term for each station and band, and one Q term for each frequency band). The model is minimized using Powell technique again.

The goodness of fit of my model is estimated using L1.2 method similar to the previous steps. The predicted data is computed as a sum of site and spreading terms minus the attenuation. The residuals for each event are calculated as the difference between the observed and predicted data minus the mean of this difference for each event.

Next, I solve for 2-D attenuation using events with residuals less than 0.3. Latitude and longitude directions are split into 0.1 degree grid intervals. Using the regional box constrained by 9.5^{o}N, 11^{o}N, 86^{o}W and 84.5^{o}W, there are 21 grids going from north to south, and 16 grids going from east to west. For each event - station pair, I calculated the great circle using WGS84 ellipsoid, and split it into a number of equal segments of length roughly equal to $\frac{1}{10}^{th}$ of the grid interval.

From each segment of the great circle arc I find Q at the midpoint of the segment as a function of Q at the corners of the surrounding grid. This is the bilinear interpolation method of *Um and Thurber* (1987). This allows us to estimate the partials with respect to attenuation at the corners. Site partials are unity, and I avoid inverting for source terms by subtracting the average of the amplitudes for each event. The solution for site terms and Q^{-1} was obtained using a linear least squares method. The final correction was given by the sum of the site term and the spreading term minus the Q term.

The resulting attenuation distribution is interesting, because it shows in several frequency bands with higher Q region near the central and southern Nicoya Peninsula. Figure 4.8 shows the Q results for two frequency bands, 1-1.5 Hz and 8-10 Hz, in the region of dense ray coverage. High Q values mean low attenuation and low Q represents regions with high attenuation. The ray coverage over the peninsula is very good, given the density of the earthquakes and close spacing of the stations, which may suggest that the sudden decrease in coda attenuation in that particular region is real.

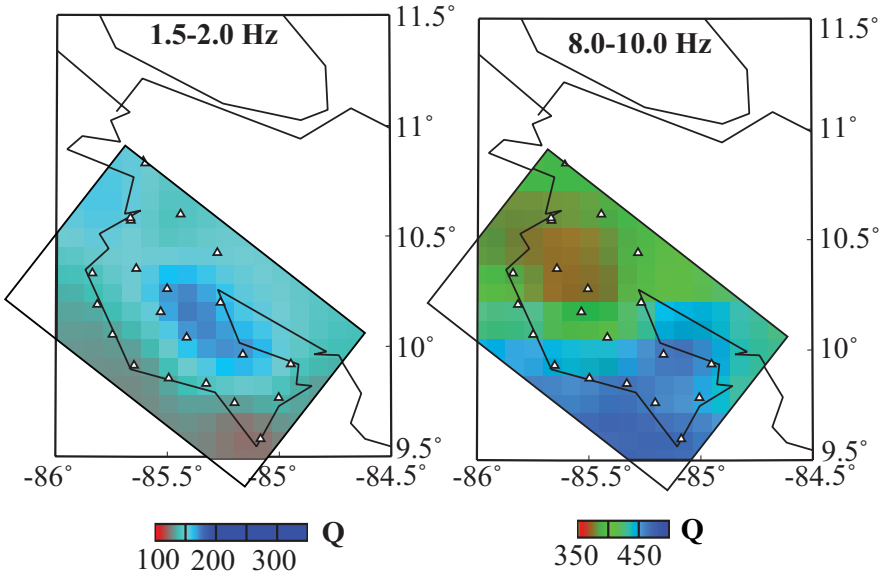

Figure 4.8: Seismic attenuation across Nicoya Peninsula
Seismic attenuation across Nicoya Peninsula at 1-1.5 Hz and 8-10 Hz. At both frequencies, there is higher Q (low attenuation) spot near the central part of the Nicoya Peninsula. At 8-10 Hz, this spot spreads into the southern Nicoya Peninsula.

4.3.3 Analysis

Source-to-coda transfer function

Before further data analysis, I need a function that would tie the measured amplitudes to an absolute scale. I had seismic moment values for three events in our dataset that were estimated independently of this calibration procedure (Table 4.4), using waveform inversion. These seismic moments were used to find a function that will cause the amplitudes to fit the Brune source model (*Brune*, 1970) and follow the Magnitude and Distance Amplitude Correction (MDAC) scaling law described in *Walter and Taylor* (2001) (Figure

4.9). The major assumptions in the Brune source model are that the amplitude spectrum is flat below the corner frequency (ω_c), and falls off as f^{-2} at frequencies above the corner. In the Brune source model, the flat portion of the amplitude spectrum (also known as the seismic moment, M_0) is proportional to ${\omega_c}^{-3}$, which is reffered to as self-similar scaling. The MDAC model is based on the Brune source model, but it allows for variable scaling of M_0 with ω_c. I used both models, the Brune source model to fit amplitudes at low frequencies and the MDAC model to incorporate non-constant M_0 scaling with ω_c, to compute the shift for corrected amplitudes of the events that had M_0 estimates.

Using fixed source parameters and independently calculated M_0, I estimated corner frequency for each of the events that had an M_0 estimate. Initially, I set a reference apparent stress (σ'_a) equal to 1 MPa, calculate *k-factor* using fixed source parameters (*Walter and Taylor*, 2001):

$$kfact = \frac{16\pi}{\beta_S^2(\frac{R_P^2\zeta^3}{\alpha_S^5} + \frac{R_S^2}{\beta_S^5})}, \tag{4.15}$$

where the seismic wave velocities, S and P, (β_s and α_s) are 3.5 and 6.0 km/s respectively, ζ, the ratio of the P and S wave corner frequencies, equals 1, R_P is the average P wave radiation pattern and equals 0.44, and R_S is the average S wave radiation pattern and equals 0.6 (*Phillips et al.*, 2008). To estimate ω_c, I followed (*Walter and Taylor*, 2001):

$$\omega_c = \frac{1}{2\pi}(\frac{kfact\sigma_a}{M_0})^{\frac{1}{3}}, \tag{4.16}$$

where

$$\sigma_a = \sigma'_a * (\frac{M_0}{M'_0})^{\psi}, \tag{4.17}$$

here, M_0 is the independently known seismic moment, M_0' is the reference seismic moment (10^{15} Nm) given the σ_a', and the exponent ψ is set to 0.25. This exponent represents a nonconstant scaling parameter and was obtained from the study by *Mayeda and Walter* (1996). If I were to use a constant scaling model, the ψ term would be 0. With the estimated ω_c, and the known seismic moment, I computed the source amplitude again following (*Walter and Taylor*, 2001):

$$\log A_p(f,r) = \log M_0 - \log(1 + (\frac{f}{\omega_c})^2), \tag{4.18}$$

where A_p is the predicted spectral amplitude, and f is the center frequency of any given frequency band. The resulting transfer function was the median difference between site and path corrected amplitude and predicted source amplitude. The goodness of fit using root mean square residuals (rms) between the predicted and observed amplitudes for each frequency band was calculated as:

$$rms = \sqrt{\frac{\sum(A_m(f) - A_p(f) - trans(f))^2}{N}}, \tag{4.19}$$

here A_m is the site and path corrected amplitude, A_p is the predicted amplitude, *trans* is the transfer function shifting A_m to absolute units, and N is the number of amplitude data.

In order to improve the fit of the observed and predicted source amplitudes, I run two more inversions to obtain the best solution. At first, I inverted for the transfer function and σ_a together. Having a reasonable results for transfer function and σ_a, I run the inversion again, this time allowing free ω_c in the process. In each case residuals were minimized using L1.2 technique. I also computed the final rms residuals for predicted and observed source amplitude

at each frequency band.

Table 4.4: Seismic moments computed using waveform inversion (M_{0w}, S. Bilek, pers. comm. 2007) compared to coda moments (M_{0c}). This table also includes corner frequencies (ω_c obtained using coda calibration, original magnitudes and depths.

Event ID	M_{0w} (log Nm)	M_{0c} (log Nm)	ω_c (Hz)	Mag (M_L)	Depth (km)
2963	15.24	15.25	2.99	4.11	21
23018	13.89	13.92	4.36	3.10	16
25897	14.52	14.43	4.48	3.46	19

The resulting shifted amplitude spectra at frequencies below the ω_c fits well with the original M_0 estimate. In Fig. 4.9, the blue line represents the independently known M_0 for this earthquake. This event was one of the few above M_L 4, with high SNR at all frequency bands. At low frequencies, below the corner frequency, the modeled M_0 (Fig. 4.9, red line) is in a good agreement with the previously known estimate.

Source parameters

Now I have the transfer functions that allow me to shift all of the path corrected amplitudes to absolute units. After shifting the corrected amplitudes, I computed M_0 for all events that had more than one corrected amplitude. At first I fit the spectra varying M_0, and constraining the ω_c using a scaling model. Then this step was repeated, but now I inverted simultaneously for M_0 and ω_c. In this second step, I also calculated source parameters for each station and the network for a given event. All of the calculations in this step were done using Eq. 4.18.

Before the inversion, M_0 was allowed to vary between 10^5 and 10^{25}

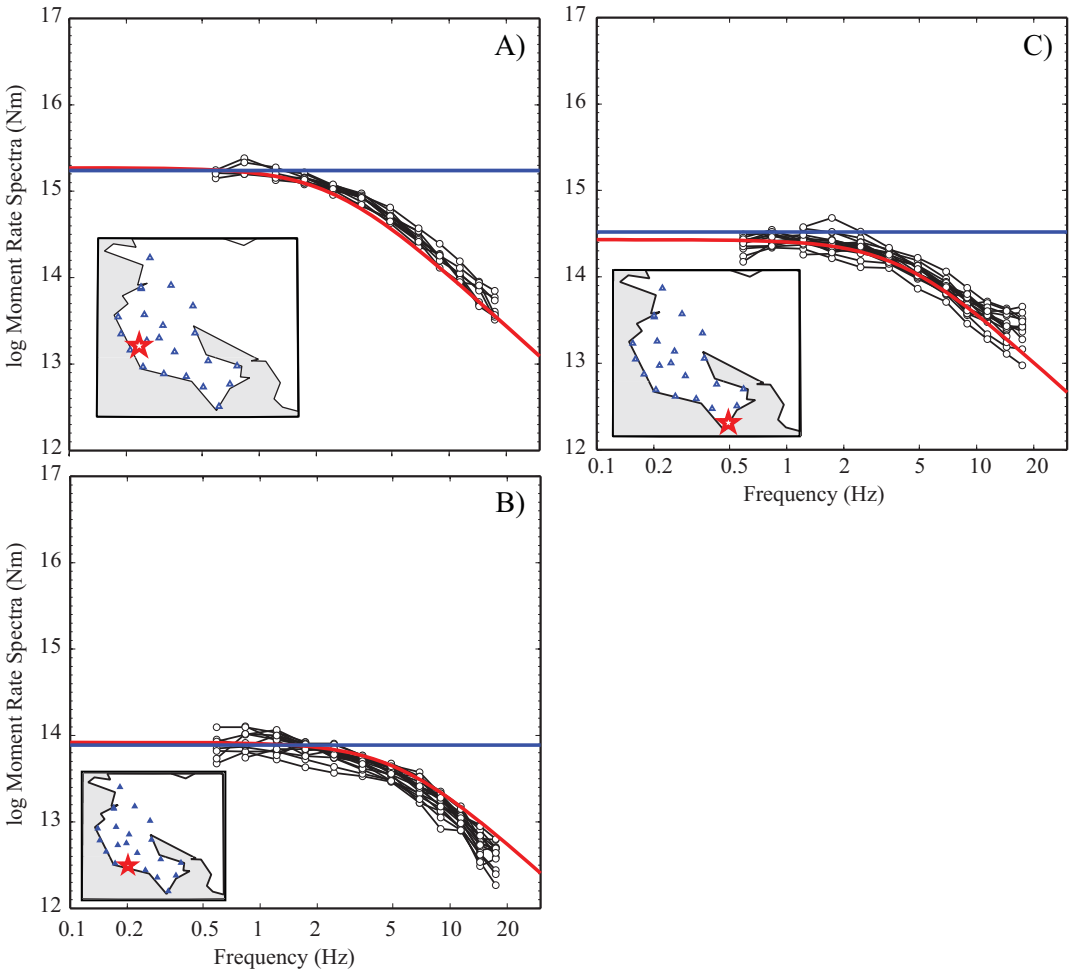

Figure 4.9:
Source spectra model (red line) of earthquakes with M_0 estimated using waveform inversion (blue line) after applying transfer function to the path and source corrected amplitudes (open circles): a) M_L 4.11 that occurred on Dec 23, 1999 (event ID 2963, Table A.1), b) M_L 2.32 that occurred on Jan 01, 2001 (event ID 23018, Table A.1), and c) M_L 3.46 that occurred on Jan 22, 2001 (event ID 25897, Table A.1).

Nm. Then, I searched for the best fitting midpoint using grid search, used this as a starting point, and solved for M_0 with Brent's minimization method (*Press et al.*, 2007). I estimated covariance at the solution point using finite differences. If the results were within the cutoff range (M_0 was between 0 and M_0 given by M_w 8.0), I repeated this process to solve for M_0 of this event using the whole network.

Once I had constrained results for M_0, I re-run the inversion to solve simultaneously for M_0 and ω_c. Again, the starting model is computed using a grid search, where I searched for best solution of ω_c given M_0 ranging between 10^5 and 10^{25} Nm. This model searches for best solution using a downhill simplex method *Press et al.* (2007). The covarience of the solution is estimated by applying eigenvalue analysis to finite differences. This process was repeated jointly for all stations.

I solved for σ_a using Eq. 4.16. The resulting fits for M_0 versus M_0 and ω_c are plotted with the computed spectra in Fig. 4.11 and 4.12. In some cases, the scatter in the amplitude spectra was large compared to the difference between the two fit models (Fig. 4.11), thus it was hard to determine which model fits the data better. However, in some cases where the tightness of fit was very good, there was a significant difference between the two models, indicating a stress difference from the nominal model (Fig. 4.12).

A comparison between the original M_L and the calculated M_w for the 353 well constrained earthquakes is shown in Figure 4.10. The five events that I had above magnitude 3.3 show reasonable one-to-one fit. However, at magnitudes below 3.3, there is up to one magnitude unit scatter between the

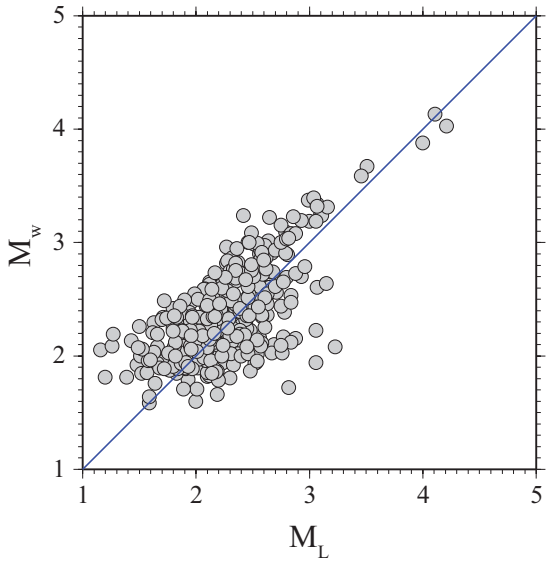

Figure 4.10:
Comparison between the original M_L and calculated M_w for 353 well constrained earthquakes. The fit between the M_L (x-axis) and M_w varies up to one magnitude unit at magnitudes below 3.3.

M_L and the M_w. In many cases, the M_w is larger, which suggests that the original M_L was underestimated. The original M_L was measured as a Richter magnitude using the maximum amplitude (A_{meas}) within the first 3 seconds after P-wave arrival as:

$$M_L = log\frac{A_{meas}}{A_0} \tag{4.20}$$

where for the Nicoya dataset epicentral distance range (*dist*, less than 200 km for all earthquakes used in this study), the A_0 is computed as:

$$A_0 = 0.15 - 1.6dist \tag{4.21}$$

Only the broadband instruments were used to compute M_L due to their flat instrument response. However, high frequency body waves are greatly affected

by path and source heterogeneities. This and the generally small size of the earthquakes recorded in a noisy environment could result in an inaccurate M_L estimates, thus explaining the large scatter between M_L and M_w in Figure 4.10.

The fit of the amplitude spectrum to the computed model has large variation in quality between the calibrated earthquakes. There were 1350 earthquakes with at least one calibrated amplitude. In order to obtain reasonable constraints on the solution for ω_c and σ_a, I required that there are at least two calibrated amplitudes below and above the ω_c. With this requirement, the number of usable earthquakes decreased to 386. I have reviewed the 386 calibrated earthquakes, and removed an additional 33 events that either located deeper than 50 km, or their amplitude spectrum was fitting poorly at the closest station.

Examples of the absolute amplitude spectrum fit to the models is shown in Figures 4.11 for a small magnitude earthquake, 4.12 for a large magnitude earthquake, 4.13 for an earthquake with low σ_a, and 4.14 for an event with high σ_a. Figure 4.11 and 4.12 compare the amplitude spectrum for M_L 1.83 (M_w 2.2) to amplitude spectrum for M_L 3.5 (M_w 3.7). Figure 4.13 and 4.14 compare amplitude spectra for earthquakes with σ_a 0.16 MPa and 10.3 MPa, respectively. In all plots, the solid line represents model where I solve for M_0 only (assuming scaling model with $\psi = 0.25$), and the dashed line represents model in which I solved for M_0 and ω_c simultaneously.

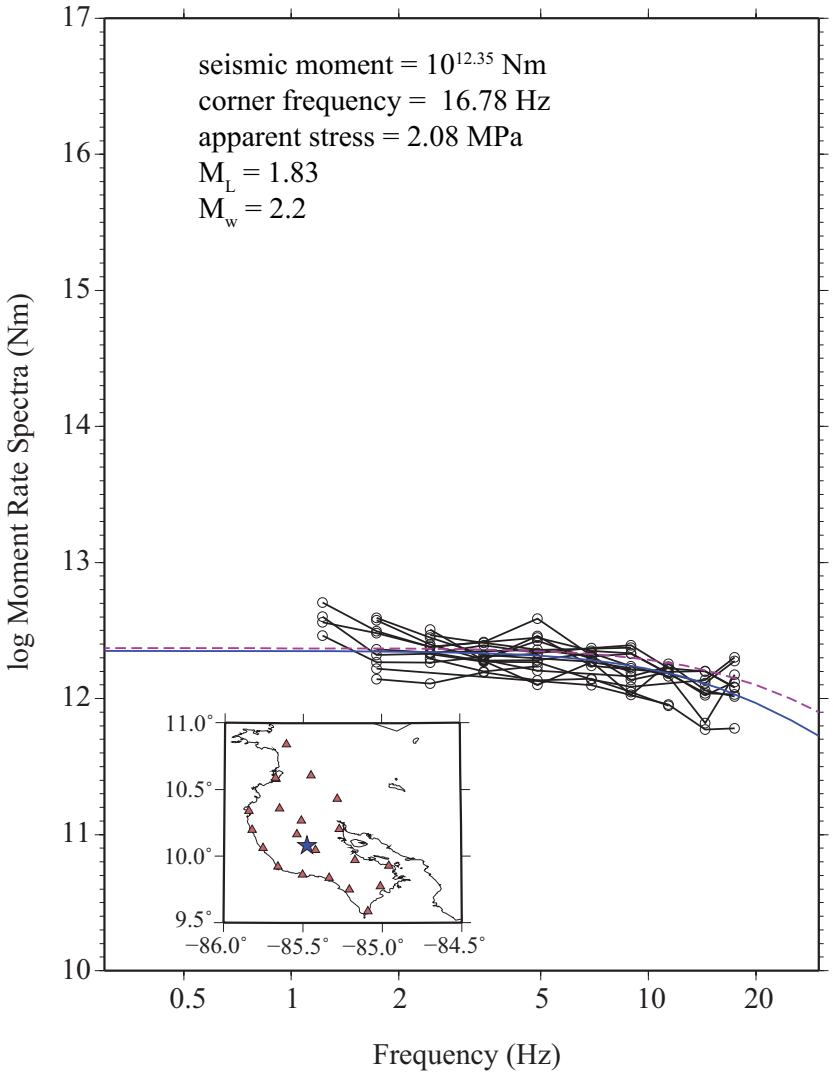

Figure 4.11:
Amplitude spectrum of M_w 2.2 earthquake (event ID 18903, Table A.1, for all stations that recorded this event. The corrected and shifted amplitudes (black circles) plotted using contrained fit (solving for M_0 only, dashed line) and free fit (solving for M_0 and ω_c, solid line). The earthquake location is shown in the insert on the bottom left. Text box at the top of the figure shows the computed M_0, ω_c, σ_a and the original M_L and new M_w.

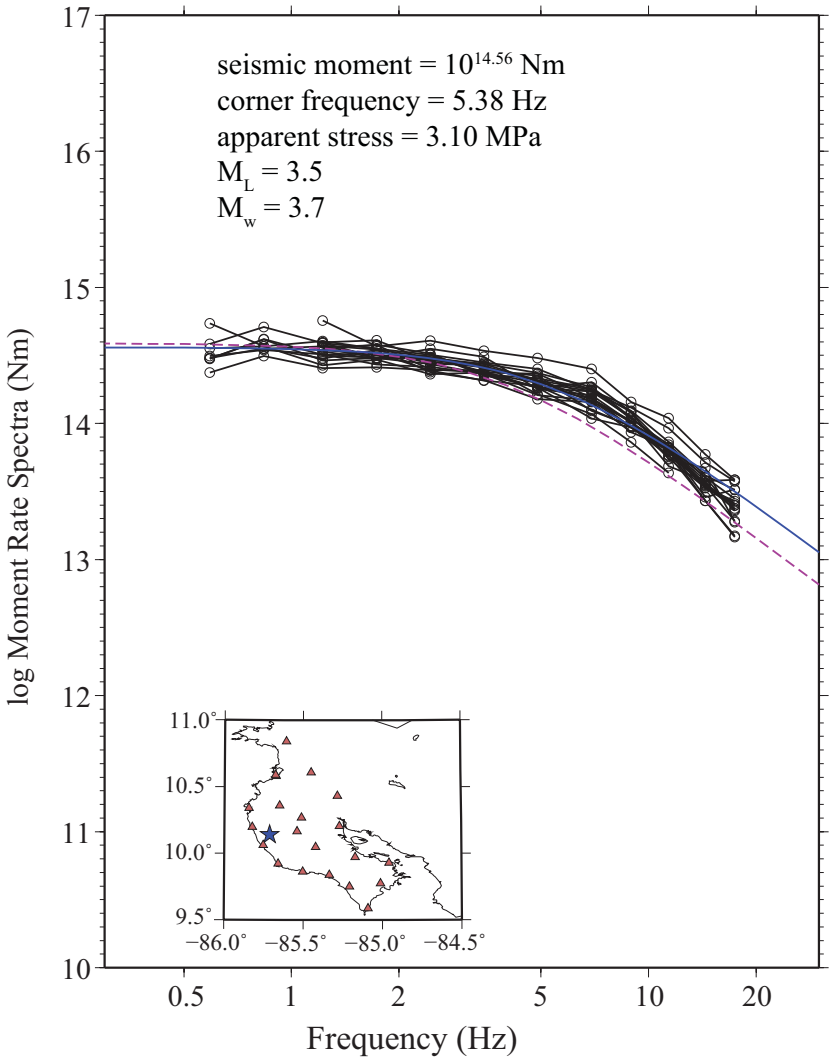

Figure 4.12:
Amplitude spectrum of M_w 3.7 earthquake (event ID 18084, Table A.1, for all stations that recorded this event. The corrected and shifted amplitudes (black circles) plotted using contrained fit (solving for M_0 only, dashed line) and free fit (solving for M_0 and ω_c, solid line). The earthquake location is shown in the insert on the bottom left. Text box at the top of the figure shows the computed M_0, ω_c, σ_a and the original M_L and new M_w.

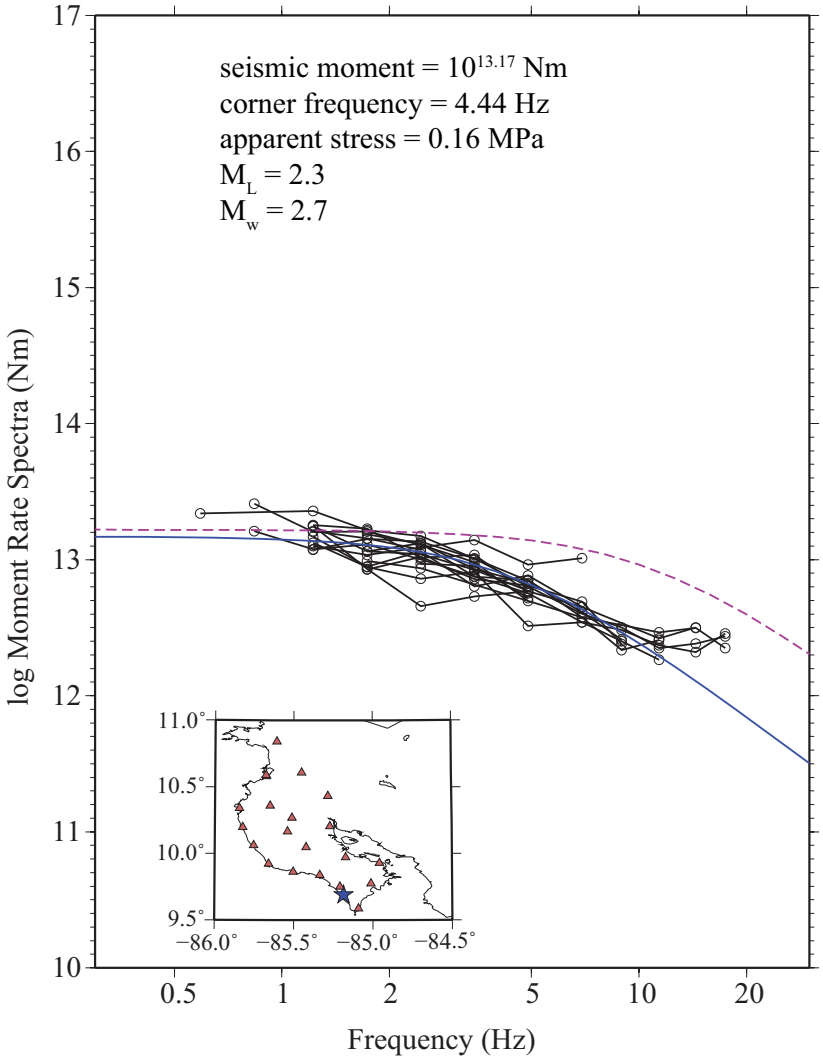

Figure 4.13:
Amplitude spectrum of M_w 2.7 earthquake (event ID 50369, Table A.1, for all stations that recorded this event. The corrected and shifted amplitudes (black circles) plotted using contrained fit (solving for M_0 only, dashed line) and free fit (solving for M_0 and ω_c, solid line). The earthquake location is shown in the insert on the bottom left. Text box at the top of the figure shows the computed M_0, ω_c, σ_a and the original M_L and new M_w.

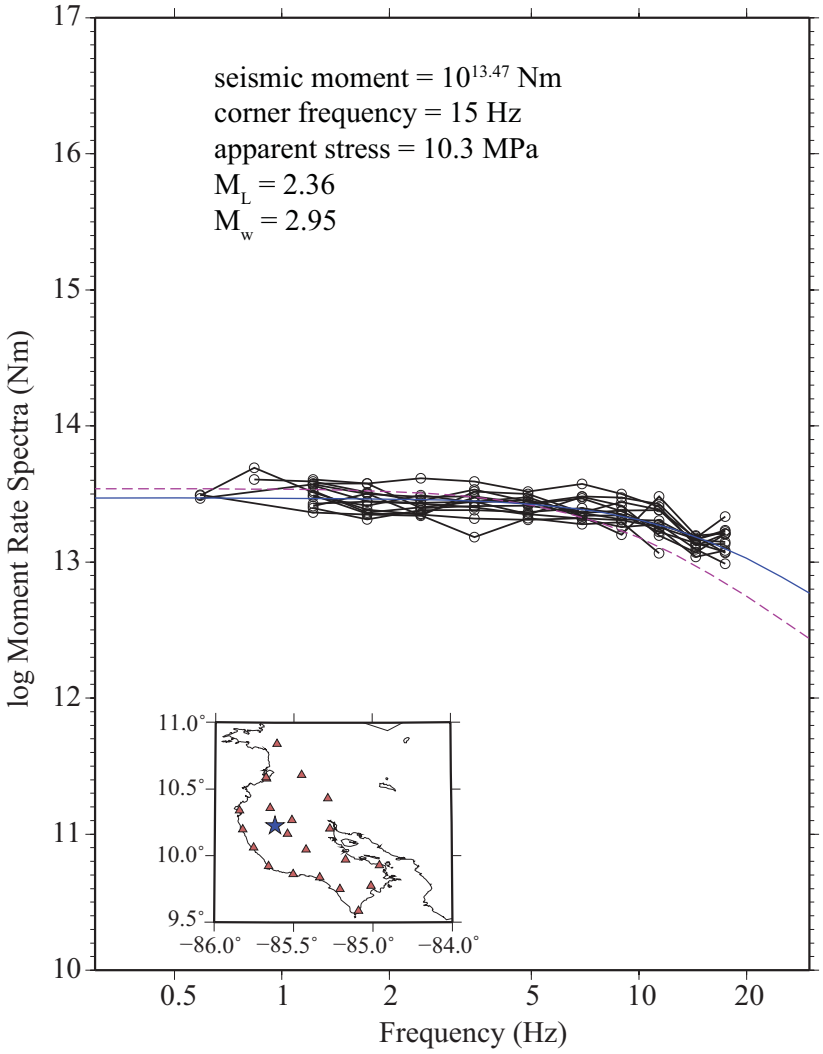

Figure 4.14:
Amplitude spectrum of M_w 2.9 earthquake (event ID 65964, Table A.1, for all stations that recorded this event. The corrected and shifted amplitudes (black circles) plotted using contrained fit (solving for M_0 only, dashed line) and free fit (solving for M_0 and ω_c, solid line). The earthquake location is shown in the insert on the bottom left. Text box at the top of the figure shows the computed M_0, ω_c, σ_a and the original M_L and new M_w.

CHAPTER 5

RESULTS

The purpose of the coda amplitude calibration was to obtain well constrained source spectra for earthquakes located along the subduction zone interface in order to estimate variations in source parameters along-strike of the subduction zone and with depth in response to variable structure of the subducting Cocos Plate. Over 1300 earthquakes were calibrated using the coda amplitude method. Out of these events I selected a set of 353 well constrained spectra with well constrained source parameters. My quality control requirements at this point were to have at least two calibrated bands above and below ω_c or at least one station with overall good spectral fit within the network for each event in order to constrain ω_c and the decay of spectra at high frequencies. All of the selected events and their resulting source parameters are listed in Appendix A, Table A.1.

5.1 Scaling model

In the classical Brune source model (*Brune*, 1970), the M_0 is proportional to negative cube of ω_c (Eq. 4.16). In the last few years, many authors have suggested that this proportionality may not hold for all magnitudes (called non-constant scaling). For example, *Kanamori and Rivera* (2004) found that the energy ratio, E_r/M_0, is smaller for small events and increases with mag-

nitude, and they also showed that this ratio is related to M_0 and ω_c, using earthquake data from a number of previous studies. They suggest that in order to allow for the changes in E_r/M_0 with magnitude, the scaling between ω_c and M_0 cannot be represented by a cube root. *Kanamori and Rivera* (2004) showed that if the cube root is modified by a positive constant (ϵ, which is ≤ 1), so that M_0 is proportional to $\omega_c^{-(3+\epsilon)}$, the fit between the observed source parameters and their modeled relationship improves significantly. Similarly, *Walter and Taylor* (2001) and *Mayeda et al.* (2003) allowed in their source inversion for variable scaling of M_0 with ω_c, and have shown that the calibrated source spectra follow the non-constant scaling models better. Therefore, I am following the non-constant M_0 - ω_c scaling of *Mayeda et al.* (2003) in this study.

The source parameters of earthquakes with M_0 computed using waveform inversion technique (S. Bilek, pers. comm. 2007) are plotted in Figure 5.1. For these three earthquakes, the rms residuals between the computed M_0 and M_0 predicted using constant scaling model and σ_a of 1.292 MPa were 2.19 Nm (diamonds and black dashed line in Figure 5.1. The rms residuals for the non-constant scaling model and σ_a equal to 1.057 MPa were 1.83 Nm (circles and blue dashed line in Figure 5.1.

In Figure 5.2 I plotted M_0 versus ω_c for the 353 well constrained earthquakes that were computed using the constant scaling model. The solid lines represent lines of constant σ_a (0.1, 1 and 10 MPa). The dashed line represents the non-constant scaling model, where M_0 is proportional to ω_c^{-4} and σ_a is 1.057 MPa. There is a large scatter in the results, making any distinction in results between the two models difficult. The group of events with M_0 below

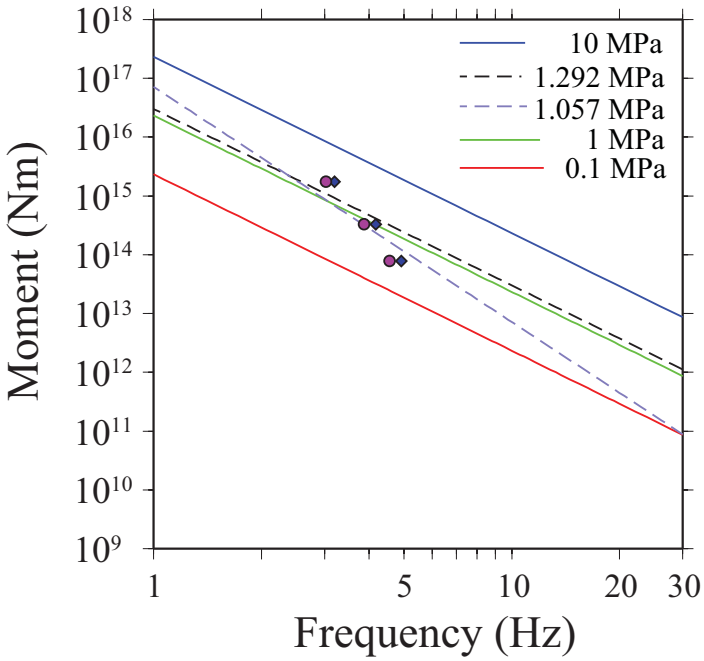

Figure 5.1:
M_0 versus ω_c using all the three earthquakes for which M_0 was determined using waveform inversion (S. Bilek, pers. comm. 2007). The solid, colored, lines represent the constant σ_a values of 0.1, 1 and 10 MPa. The black dashed line represents the constant scaling with M_0 proportional to ω_c^{-3}, and the blue dashed line represents the non-constant scaling with M_0 proportional to ω_c^{-4}.

10^{13} Nm and ω_c less than 6 Hz have generally poorer fit between the calibrated amplitudes and the spectral model. These earthquakes locate beneath the southern and central peninsula between 16 and 34 km, and span M_L 1.5 - 3.1.

The rms residual for all spectral results with the difference between the calibrated M_0 and M_0 predicted by the model using σ_a of 1.292 MPa for constant scaling and 1.057 MPa for non-constant scaling are 3.90 Nm and 2.93 Nm respectively. Only results with the absolute difference between calibrated M_0 and model-predicted M_0 were used to compute rms residuals. There were 242 events calibrated using the constant scaling model and 320 events calibrated using the non-constant scaling model that met the above criteria.

I selected a subset of the well constrained spectra based on *Hansen et al.* (2006) study to determine which model is more appropriate. These earthquakes come from a subset of events used by *DeShon et al.* (2006) for velocity model inversion. *Hansen et al.* (2006) selected them because of their signal quality. These events had to be larger than M_L 3.0, or lie on the plate boundary. In addition, for each focal mechanism *Hansen et al.* (2006) required that there were at least 7 polarity observation over 130^o azimuthal range for each focal mechanism. I had 24 events from the 353 well constrained earthquakes that were used by *Hansen et al.* (2006) to compute the focal mechanisms (Fig. 3.1). The selected events seem to follow the non-constant scaling better by visual inspection (Fig. 5.3), however, there is still scatter in the fit. The rms residuals for this subset are 3.4 Nm for constant scaling model with σ_a equal to 1.292 MPa and 2.37 Nm for non-constant scaling model with σ_a equal to 1.057 MPa (again, residual factors of solution give the spread). The same criteria

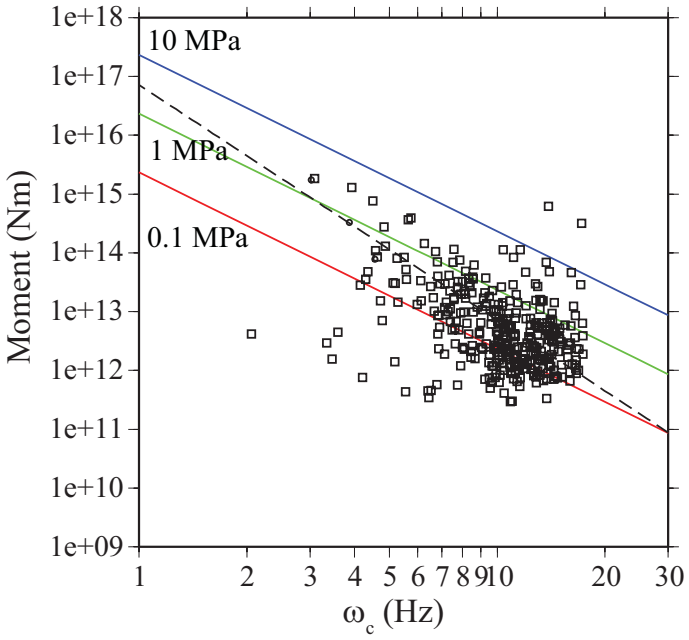

Figure 5.2:
M_0 versus ω_c using all 353 well constrained earthquakes. The solid, colored, lines represent the constant σ_a values of 0.1, 1 and 10 MPa. The dashed line represents the non-constant scaling of M_0 with ω_c using ψ of 0.25.

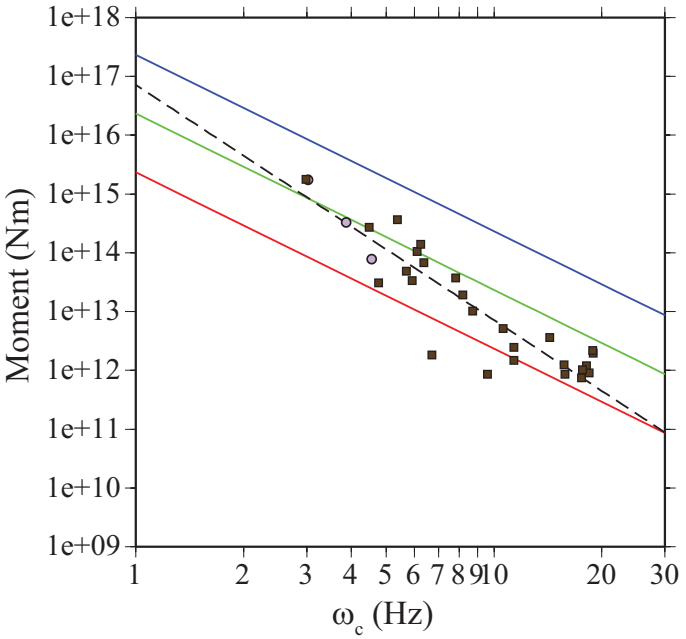

Figure 5.3:
M_0 versus ω_c using 24 earthquakes with known focal mechanism (Fig. 3.1). The events with independent M_0 estimates are shown as circles, the calibrated events are shown as squares. The solid, colored, lines represent the constant σ_a values of 0.1, 1 and 10 MPa. The dashed line represents the non-constant scaling of M_0 with ω_c using ψ of 0.25.

was used to compute the rms residuals of this subset as in the above paragraph. There were 21 earthquakes calibrated using the constant scaling model and 23 using the non-constant scaling model that had calibrated M_0 - predicted M_0 absolute difference less than one.

Another way to look at the scaling relationship between large and small earthquakes is to analyze the behavior of σ_a with M_w. If small earthquakes were basically scaled-down large events, the σ_a should be constant for

all magnitude range (*Walter et al.*, 2006). Figure 5.4 shows σ_a plotted versus M_w for all constrained data, as well as two lines of constant σ_a as plotted by *Walter et al.* (2006). Earthquakes with σ_a below 3 MPa forms the main group

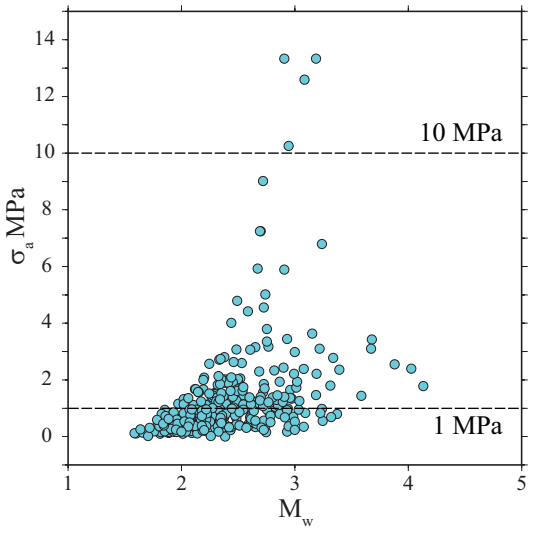

Figure 5.4:
a) Apparent stress plot vs. M_w for all constrained data. The horizontal dashed lines represents constant σ_a for 1 and 10 MPa. If σ_a were independent of magnitude, the data would plot in generally horizontal line. However, my data suggests that σ_a increases with magnitude at least with the smaller earthquakes.

in Figure 5.4. There were 26 earthquakes with σ_a above 4 MPa that span almost an order of magnitude in σ_a and range between M_w 2.4 and 3.2. The events with large σ_a located between 20 and 50 km depth. The earthquakes with σ_a above 10 MPa (4 total) located between 35 and 50 km. I selected 327 earthquakes with σ_a below 3 MPa to evaluate the relationship between M_w and σ_a for the main group in Figure 5.4. For this group of events σ_a scales with M_w as shown in Figure 5.5. The linear fit (Fig. 5.5, a) has positive slope, but the scatter in the data is large causing high residuals (Fig. 5.5, b).

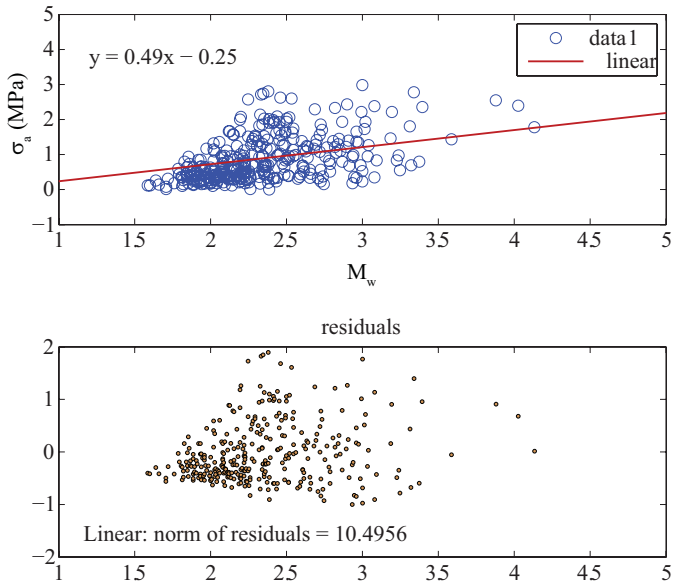

Figure 5.5:
a) Apparent stress plot vs. M_w for 327 constrained earthquakes with σ_a below 3 MPa. b) The norm of the residuals using the linear fit to the data in part a.

5.2 Along-strike σ_a variation

The earthquake σ_a does vary along-strike of the subduction zone as shown in Figure 5.6. Generally small values, below 2.5 MPa, prevail at the southern portion of the peninsula. Exception to this is the group of high σ_a value events in the entrance to the Gulf of Nicoya. Along the northern and central portions of the peninsula, the σ_a values are highly variable. Earthquakes with the highest σ_a values were located in the entrance to the Gulf of Nicoya (2 events with 13.3 MPa) and at the northern tip of the Nicoya Peninsula (13.4 MPa). Earthquakes with the lowest σ_a values occurred in the southern (0.02 MPa) and central (0.02 and 0.005 MPa) portions of the Nicoya Peninsula. In Figure 5.6 many of the σ_a values are hidden due to high density of data. Therefore, I decided to take the median of σ_a based on geographical bins to look at the spatial variation in more detail.

I initially divided the region into a 0.1 by 0.1 degree bins and computed a median σ_a for each of them. The results are shown in Figure 5.7. At this scale, the median σ_a is generally small at the southern and central portions of the Nicoya Peninsula. Exceptional to this are few high median σ_a values at the location of the subducted seamount and at the entrance to the Gulf of Nicoya. These earthquakes located at depth between 30 and 50 km, thus they did occur in the subducting slab. The median σ_a values are generally higher along the northern portion of the peninsula, possibly reflecting the stronger coupling or higher friction between the Cocos and Caribbean plates in that region. The median σ_a across the EPR-CNS suture is 1.2 MPa on the EPR side and 0.62 MPa on the CNS side.

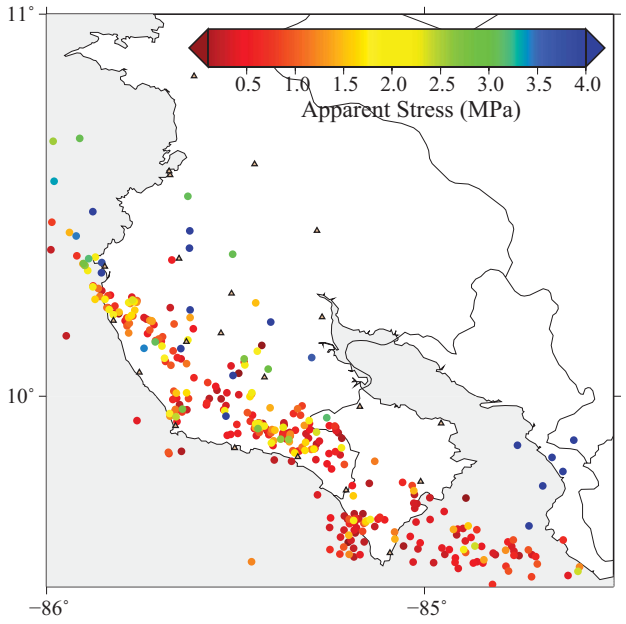

Figure 5.6:
Earthquake σ_a distribution for 353 well constrained events. The colors span σ_a range between 0.1 and 4 MPa, values below that range are dark red and values above that range are dark blue.

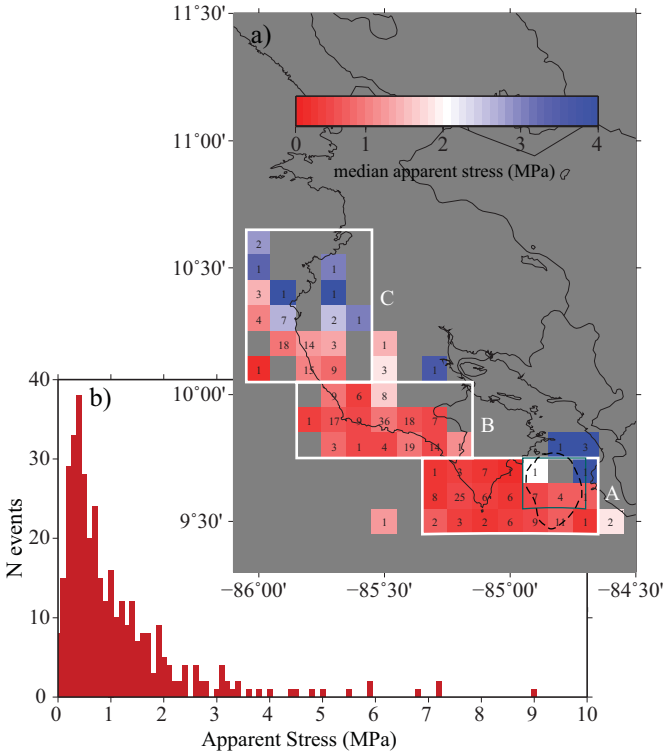

Figure 5.7:
a) The median σ_a values vary along-strike of the subduction zone. The data was split into 0.1 x 0.1 degree regions. For each region a median σ_a was calculated. The color scale shows smallest values as red and largest values as blue. Values below 0.1 and above 4 MPa were not used when creating the grid file, because of their scarcity. In general, higher median σ_a values are in the northern regions, near the subducted seamount (dashed line, *Protti et al.* (1995)) and at the entrance to the Gulf of Nicoya. The central and southern portions of the peninsula show smaller median σ_a. Regions bounded by white boxes were examined in more detail in the following text. Numbers in each grid cell represent the number of events used to compute the median σ_a. b) A histogram showing the σ_a distribution within the dataset. The distribution of σ_a between 0 and 1 MPa is nearly normal. The number of earthquakes with σ_a above 1 MPa decreases exponentially with increasing σ_a.

In this analysis, I used the GMT polar grid coloring to represent the low and high median σ_a values. The deepest red colors show regions with very small median σ_a (at and below 0.1 MPa), while the darkest blue colors show regions with high median σ_a (at and above 4 MPa). Each of the colored grids contains the number of events used to compute the σ_a median. There are several grids that contain large number of events. Therefore I decided to examine the results in more detail. The white boxes bound regions that were chosen for closer analysis.

For each of the regions in the white boxes, I re-calculated median σ_a for much smaller grid cells (0.01 by 0.01 degree). The smallest median values (0.43 MPa) from 97 calibrated events were located at the southern tip of the peninsula (region A). The exception to this is the region around a subducted seamount (dashed line in Figure 5.8, region A, *Husen et al.* (2002)), which gives median σ_a of 0.52 MPa. In the central portion of the peninsula, the median σ_a was little higher (0.66 MPa) using 141 well calibrated events. The median σ_a values were more than twice as high at the northern end of the peninsula (1.16 MPa) compared to the southern end using 85 well calibrated earthquakes. The differences in median σ_a may reflect the changes in friction or interface coupling along-strike of the subduction zone. The histograms of σ_a in each region show a difference between the northern and the other two sections. In the southern and central portions of the peninsula (regions A and B), most σ_a values are between 0 and 1.5 MPa. At the northern portion of the peninsula, most of the σ_a are at 1 MPa. If I consider only earthquakes with σ_a larger than 3 MPa, 74.6% of them are located at the northern portion of the peninsula.

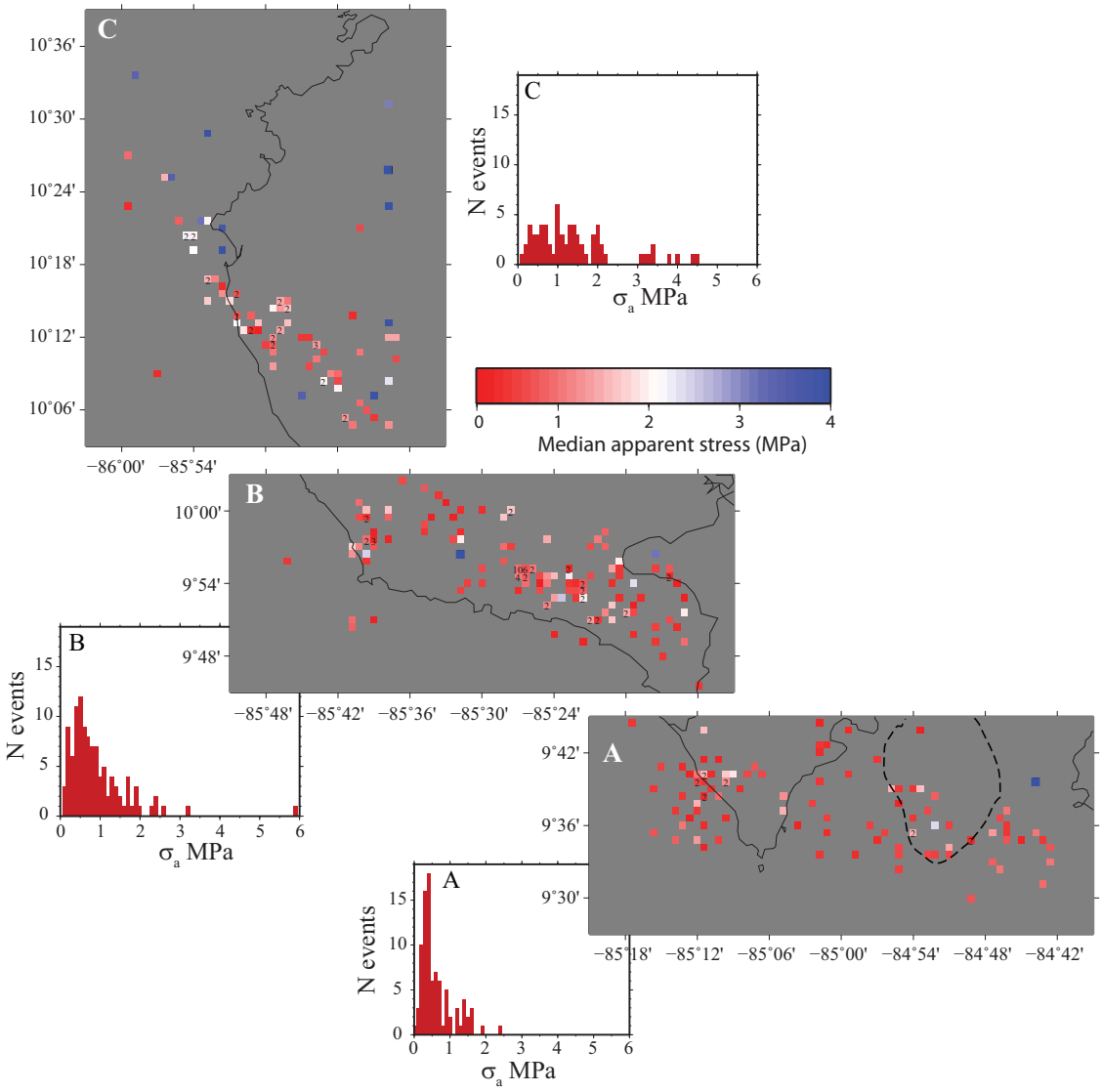

Figure 5.8:
The median σ_a values vary for regions A,B, and C. Region C has the largest median σ_a values, 1.16 MPa, using 85 earthquakes. Region B has median σ_a 0.66 MPa using 141 earthquakes. Region A has the lowest median σ_a of 0.43 MPa using 97 events. In region A, the aftershock area from the 1990, M_w 7.0, earthquake is outlined (dashed line). Within approximately this area, the median σ_a is 0.52 MPa. Also shown are the σ_a histograms for each region, with distinct difference in number of events and shape for the northern portion.

5.3 σ_a variation with depth

At greater depth along the subduction zone interface, the normal stresses acting on the interface increase, and the amount of fluids decreases, which together with higher sediment compaction results in higher friction along the interface. In any tectonic setting, the size of an earthquakes is dictated by the area of rupture, amount of slip and rigidity. Assuming that at larger depth in the subduction zone the failure along a fault produces larger stress drop, or $\eta\sigma_a$ with η being the seismic efficiency, the σ_a should increase if η remained nearly constant.

I plotted the σ_a for the 353 well constrained earthquakes versus depth in Fig. 5.9. The σ_a - depth relationship for the 353 well calibrated earthquakes is shown in Figure 5.9, part a. Majority of the earthquakes located above 30 km. The variation of σ_a with depth is not very strong up to about 2.5 MPa. There are earthquakes with σ_a between 0 and 2.5 MPa at the same depth of 20 km in all three regions (Fig. 5.9, parts b,c,and d). Earthquakes with σ_a above 2.5 MPa are more scattered with depth, with the largest σ_a (near 13 MPa) values all locating below 40 km. In the southern region, there is slight increase in depth with increasing σ_a (Fig. 5.9, part b). In the central region, the general trend shows no variation of σ_a with depth (Fig. 5.9, part c). The σ_a increases with depth in the northern region, however there is still quiet a bit of scatter in the data (Fig. 5.9, part d).

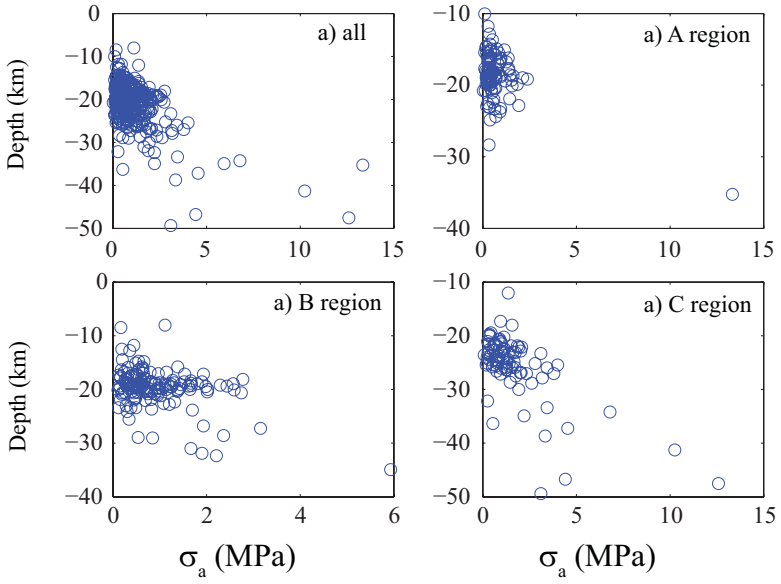

Figure 5.9:
σ_a variation with depth for all constrained data (a), region A (b), region B (c) and region C (d). Region boundaries for A, B and C are plotted in Fig. 5.8.

CHAPTER 6

DISCUSSION

Apparent stress is a measure of seismic efficiency combined with static stress drop (*Wyss and Molnar*, 1972; *McGarr*, 1999; *Beeler et al.*, 2003). *McGarr* (1999) defined seismic efficiency as the ratio of seismically radiated energy to total energy released. Studies performed on analyzing the values of seismic efficiency suggest that this parameter is generally smaller than 0.08. For example, *Wyss and Molnar* (1972) suggest that seismic efficiency for couple of earthquakes that ocurred in Denver, Colorado is possibly less than 0.01. *McGarr* (1999) analyzed seismic efficiencies for earthquakes from the Cajon Pass and southern California, and concluded that the upper limit in seismic efficiency is 0.07 and 0.08 for the two sets respectivelly. *Beeler et al.* (2003) studied the Cajon Pass borehole earthquakes, and determined that increase in apparent stress with seismic moment are due to changes in static stress drop with seismic moment. Their conclusions imply that seismic efficiency is independent of earthquake size. Given these studies, I assume that seismic efficiency is constant, and that the along-strike changes in σ_a reflect changes in the static stress drop.

Heterogeneous structure of the subducting Cocos Plate seems to affect the rupture process of microearthquakes located along the subduction zone interface. There is a clear variation in σ_a between the northern and the southern

portions of the Nicoya peninsula. North of the EPR-CNS suture (EPR crust), the median σ_a values are higher where the relatively smooth and cooler plate subducts. Here the median σ_a is 1.2 MPa using total of 109 well constrained earthquakes. South of the EPR-CNS suture (CNS crust), the average σ_a is 0.62 MPa using 244 well constrained earthquakes. The more than two factor in the variation of median σ_a values seem to reflect the along-strike structural changes of the subducting plate.

The average σ_a values for the EPR crust are little higher than the 1.5 MPa global average σ_a for subduction zone thrust earthquakes from *Choy and Boatwright* (1995). The average σ_a values for the CNS crust are within the range from global subduction zone thrust earthquakes (*Choy and Boatwright*, 1995). Average σ_a in both regions are high compared to 0.28 MPa average σ_a for the Middle America region for thrust earthquakes (*Choy and Boatwright*, 1995). However, in their study *Choy and Boatwright* (1995) used only 8 earthquakes for the Middle America region and out of these only 2 earthquakes were from the Nicoya Peninsula region (the 1990 M_w 7.0 and one of its foreshocks with M_s 6.4). The average σ_a of these two events was 0.3 MPa.

6.1 Role of seamounts

Several studies discuss the influence of seamount subduction on earthquake rupture in the convergent margin settings. *Cloos* (1992) provides a model in which subducting seamounts act as asperities, locally increasing coupling and fracturing in large underthrusting earthquakes. *Scholz and Small* (1997) discuss this model in more detail, suggesting that increased coupling is the result of excess mass and buoyancy of the subducted seamount. On the contrary,

Mochizuki et al. (2008) suggest that subducted seamounts weaken the coupling between the plates due to large water content.

There are several examples in the literature that support the notion of subducting seamounts acting as large asperities. The 1990, M_w 7.0, underthrusting earthquake in the Gulf of Nicoya, Costa Rica, has been interpreted as a rupture within a subducting seamount near the plate interface (*Husen et al.*, 2002). The earthquake located near the basal portion of the seamount, at about 20 km depth (*Husen et al.*, 2002). The 1994 Java underthrust earthquake rupture area coincides with the location of subducted seamount. The seismicity prior to this earthquake was very low updip from its location, suggesting that the seamount acted as to increase the coupling between the two plates (*Abercrombie et al.*, 2001). *Park et al.* (1999) imaged a subducting seamount near Cape Muroto (Shikoku Island, Japan) using multi-channel seismic reflection survey. The resolved image shows roughly 2 km high seamount with large thrust fault on the trench-ward face.

In the region resolved by *Husen et al.* (2002) as the area of the subducted seamount the average σ_a values are higher as compared to the rest of the data in the southern portion of Nicoya Peninsula (dotted line in Fig. 6.1). I plot the average σ_a results from Figure 5.8 over the detailed bathymetry from Figure 1.2. The difference in average σ_a near the subducted seamount compared to the rest of the southern portion of the peninsula is large. Because σ_a is a measure of the change in stress prior and after an earthquake combined with seismic efficiency, this suggests that the seamount causes either higher coupling or increase in friction along the interface. *Mochizuki et al.* (2008) state that

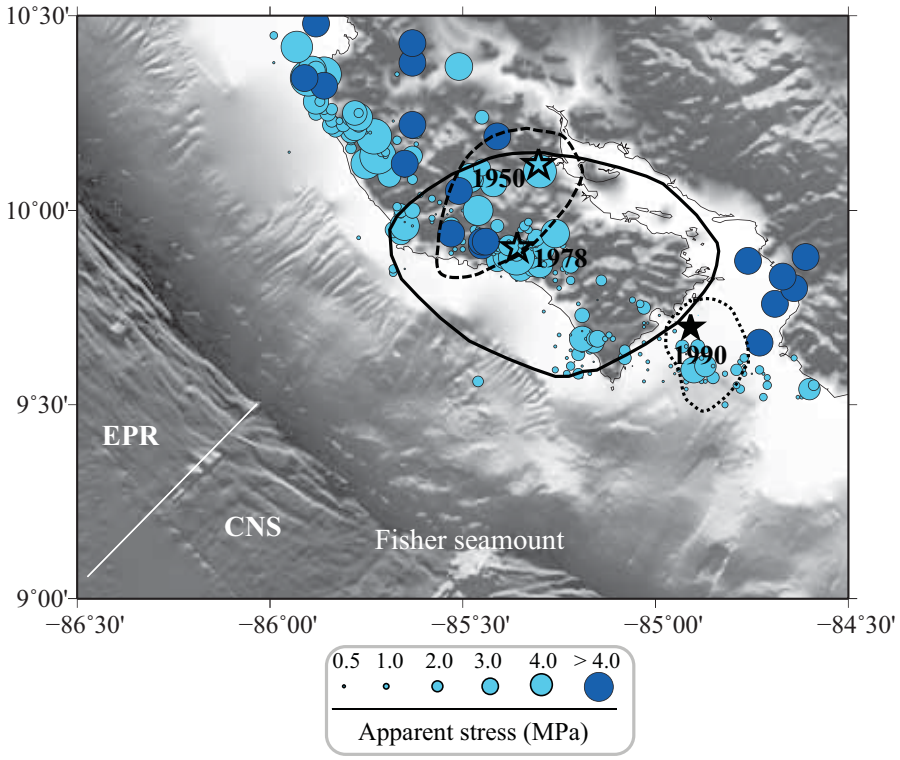

Figure 6.1:
Apparent stress distribution along-strike of the subduction zone at Nicoya Peninsula. Also shown are the rupture areas of the 1950 (solid line), 1978 (dashed line) and 1990 (dotted line) subduction thrust earthquakes.

the seamount in their study region acts as to weaken the coupling instead of being an asperity. However in their case, the base of the seamount is at about 13 km depth. It could be the case that this seamount has not released enough fluids yet as to become an asperity.

6.2 Comparison with geodetic studies

There were two geodetic studies done on the Nicoya Peninsula recently. During CR-SEIZE a GPS study was done on Nicoya Peninsula focusing on the variations in geodetic locking along-strike of the subduction zone (*Norabuena et al.*, 2004). The other geodetic study was done recently by LaFemina (personal communication, 2008) and includes several more years of geodetic data. *Norabuena et al.* (2004) resolved a region of higher coupling near the central portion of the peninsula at about 14 km depth that experiences higher coupling than the rest of the coastal region. The authors resolved another patch more inland at about 39 km (Fig. 6.2). These patches could be related or could represent individual fully locked regions separated by freely slipping zone (*Schwartz and DeShon*, 2007). The grid spacing used to create the colored map of percent locking in Figure 6.2 is 0.02 by 0.02 degrees. The unpublished results from LaFemina also show two distinct patches with higher percentage of locking compared to the rest of the Nicoya Peninsula. However, there is some difference in the location of the coastal patch between *Norabuena et al.* (2004) results and those from LaFemina. I overlaid the average σ_a values on top of the interface locking image from both studies (Figures 6.2 and 6.3).

The image using *Norabuena et al.* (2004) results is interesting, in that it shows very low apparent stress values near the highly locked patch at the central portion of the peninsula (panel B, Fig. 6.2). However, there are only two earthquakes within the region of highest locking. These earthquakes are located below the lower limit of the locked patch (event ID 18864 and 18865 located at 17 and 18.6 km respectively) assuming the patch is centered at 14 $\pm$

2 km (*Schwartz and DeShon*, 2007). At the northern part of the peninsula, the interface locking is lower, but the average σ_a is highest there (Fig. 6.2). This could reflect variations in the interface coupling across the EPR-CNS suture. At the southern end of the Nicoya Peninsula, the high average σ_a values are near the region of the subducted seamount (dashed line, Fig. 5.8) and at the entrance to the Gulf of Nicoya (Fig. 1.2). The higher average σ_a in the presence of the seamount may represent higher friction or stronger coupling around the seamount. The high average σ_a values at the entrance to the Gulf of Nicoya are all between 30 and 50 km depth, thus near the subduction zone interface or below it.

Similarly to *Norabuena et al.* (2004) there are two distinct high-locking patches at Nicoya Peninsula in the more recent model from LaFemina (Fig. 6.3). However, in the figure created with LaFemina results, the highly locked coastal patch has little overlaying average σ_a values. Near the highly-locking patch inland, there are several large average σ_a events. It is expected that in higher locking regions the earthquake σ_a is large, because the interface experiences higher coupling of friction.

In comparing the average σ_a distribution with geodetic locking results, I would expect to see absence of low average σ_a values in regions with high locking assuming that all of my data locates at or near the interface. In general, this is the case with the highly locked coastal patch. Two earthquakes with σ_a 1.0 and 0.8 MPa plot in the highly locked region from *Norabuena et al.* (2004). However, these events locate below the resolved patch. In the average σ_a plot over the results from LaFemina, there is no constrained earthquake within the

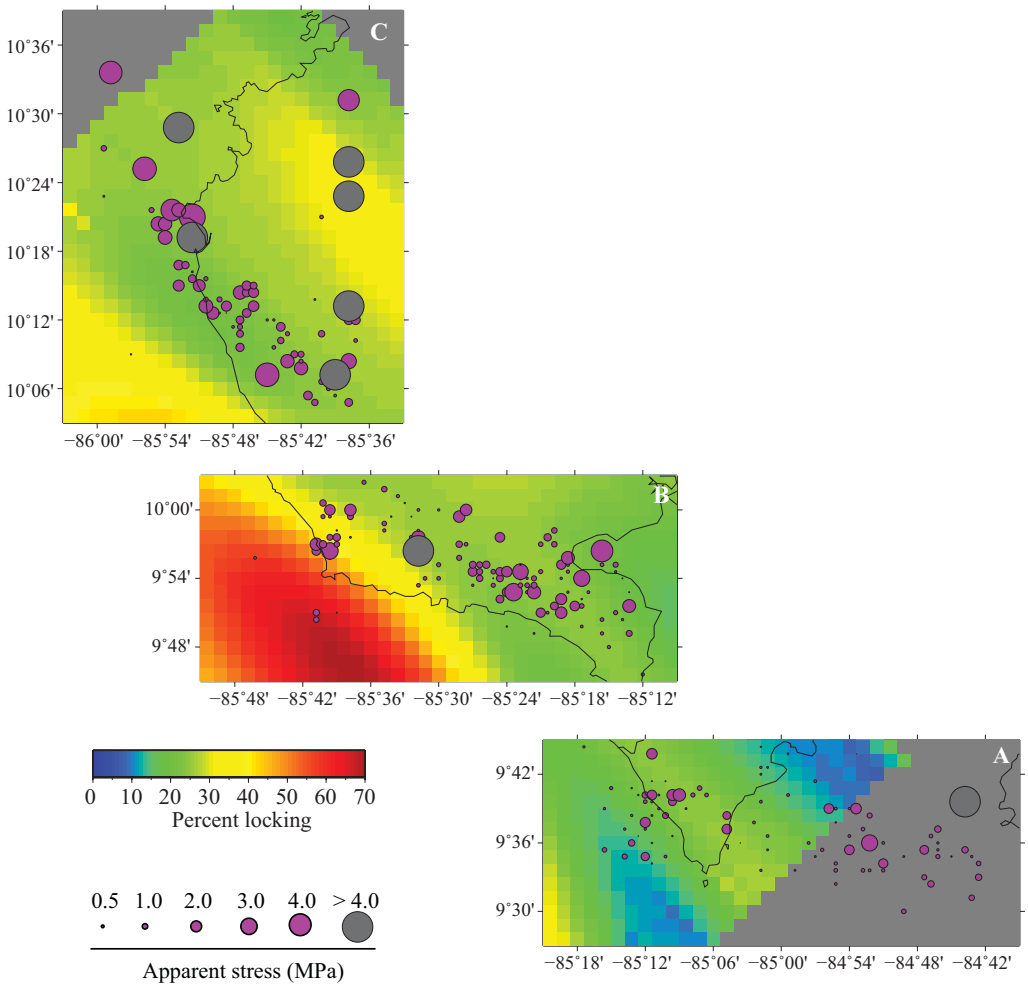

Figure 6.2:
The amount of locking on the subduction zone interface using CR-SEIZE GPS data (*Norabuena et al.*, 2004) compared to the average σ_a distribution (circles). The purple circles represent average σ_a values below 4 MPa (size is equivalent to average $\sigma_a/5$). The blue circles are of constant size and represent events with σ_a above 4 MPa.

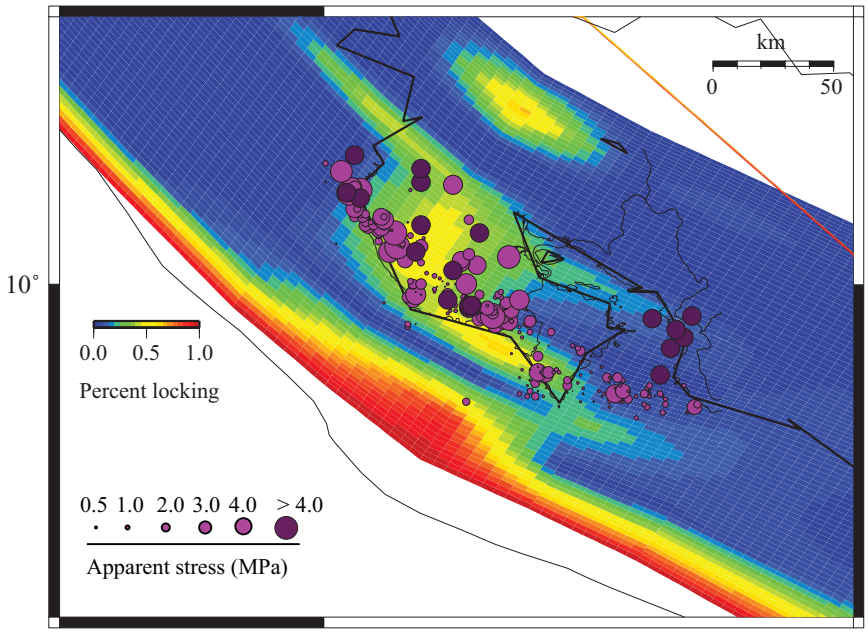

Figure 6.3: GPS and σ_a analysis II
The geodetic locking results for Nicoya Peninsula from LaFemina (personal communication, 2008). There are two highly locking patches, one along the coastline and another farther inland. The coastal locked patch is located south from the one resolved in *Norabuena et al.* (2004) study.

coastal patch with highest locking, only one earthquake is on the edge. The inland locked patch varies between the two studies, but in either case I have large σ_a earthquakes located within and around it. Given the location and depth (40 ± 5 km) of the locked patch by *Norabuena et al.* (2004), I have three earthquakes with σ_a above 4 MPa locating directly in the locked region. This is consistent with the higher stresses in that region. Using the results from LaFemina, there is a gap in constrained earthquakes at the eastern part of the locked patch, but several earthquakes (some with large σ_a) located directly over the patch closer to the coast. Unfortunately, closer analysis of the results from LaFemina is difficult because I do not have any constrains on the depth of the locked patches or resolution of the results.

6.3 Comparison with seismicity studies

Ghosh et al. (2008) computed b-value for subsets of earthquakes along the subduction zone interface below Nicoya Peninsula, using the CR-SEIZE data. In general, high b-values indicate larger portion of small earthquakes in a dataset and low b-values indicate smaller portion of small earthquakes in a dataset. The distribution in b-value, computed using a Maximum likelihood method, along-strike of the subduction zone shows low value near the central portion of the peninsula, and large values at the southern and northern portion of the peninsula (*Ghosh et al.*, 2008). As the low b-value region extends to the high locking patch from *Norabuena et al.* (2004), *Ghosh et al.* (2008) suggest that b-value analysis could be used as a proxy for determining locked patches along faults. I used the results from *Ghosh et al.* (2008) and overlaid their results with my mean σ_a values (Fig. 6.4). The high mean σ_a values are

located mostly in regions with low b-value. The mean low σ_a values are in regions with both, low and high b-value. Therefore, there does not seem to be any relationship between regions with varying b-value and low mean σ_a.

In general, the average σ_a shows the largest difference going from the southern peninsula, where the values are very low, to the central and northern peninsula. I do not see that large variance reflected in the b-value distribution. *Ghosh et al.* (2008) attribute high b-value to a region of higher locking, which is shown the geodetic results of *Norabuena et al.* (2004). However there are several large σ_a earthquakes in the northern region with low b-value, which suggest that the friction or the coupling along the interface is higher than at the southern end of the peninsula.

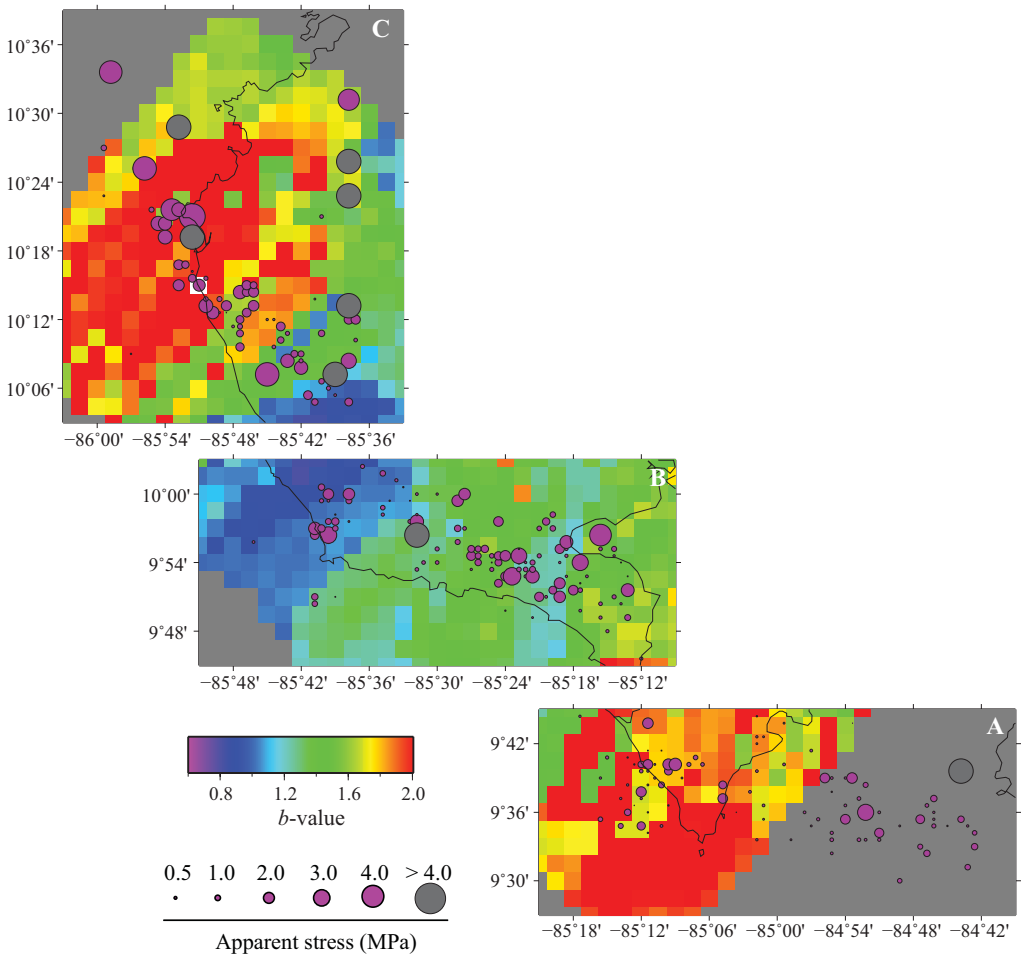

Figure 6.4:
The b-value distribution (*Ghosh et al.*, 2008) along-strike with overlaid mean σ_a values from 353 well constrained events.

CHAPTER 7

CONCLUSIONS

Coda amplitude calibration method provided me with 353 events with well constrained source parameters for shallow subduction zone earthquakes at Nicoya Peninsula, Costa Rica. The average σ_a varies along-strike of the subduction zone, in response to heterogeneous structure of the subducting Cocos Plate. The lowest values are near the southern portion of the peninsula, except for the Gulf of Nicoya region. Here the subducting plate is warmer and carries numerous seamounts into the trench. The σ_a values increase slightly at the central portion of the peninsula, where the EPR-CNS suture subducts. This region contains a high locking patch as determined geodetically along the interface. There are only a few well constrained earthquakes in this area near the coastline, and these are located below the locked patch. In the northern part of the peninsula, the average σ_a values are almost twice as high as compared to the southern part. The subducting plate north of the EPR suture is colder and shows little relief as it enters the trench. The high σ_a values at the northern portion of the peninsula suggest that the subduction zone interface is stronger or experiences higher friction, which is reflected in the inland higher locking patch from geodetic studies. The average difference in σ_a across the EPR-CNS suture is about 0.5 MPa, or factor of 2. This implies that the changes in the structure of the subducting Cocos Plate are driving the stress changes at the

subduction zone interface across the EPR-CNS suture.

Bibliography

Abercrombie, R. E., M. Antolik, K. Felzer, and G. Ekström (2001), The 1994 Java tsunami earthquake: Slip over a subducting seamount, *J. Geophys. Res.*, *106*(B4), 6595–6607.

Aki, K. (1969), Analysis of the seismic coda of local earthquakes as scattered waves, *J. Geophys. Res.*, *74*(2), 615–631.

Aki, K., and B. Chouet (1975), Origin of coda waves: source, attenuation, and scattering effects, *J. Geophys. Res.*, *80*(23), 3322–3342.

Avants, M., S. Schwartz, A. Newman, H. DeShon, M. Protti, and F. Güendel (2001), Large underthrusting earthquakes beneath the Nicoya Peninsula, Costa Rica, *Eos Trans. AGU*, *82*(47), Fall Meet. Suppl., Abstract T52E-07.

Barckhausen, U., C. R. Ranero, R. von Huene, S. C. Cande, and H. A. Roeser (2001), Revised tectonic boundaries in the Cocos Plate off Costa Rica: Implications for the segmentation of the convergent margin and for plate tectonics, *J. Geophys. Res.*, *106*(B9), 19,207 – 19,220.

Beeler, N. M., T.-F. Wong, and S. H. Hickman (2003), On the expected relationships among apparent stress, static stress drop, effective shear fracture energy, and efficiency, *Bull. Seism. Soc. Am.*, *93*(3), 1381 – 1389.

Bilek, S. L., S. Y. Schwartz, and H. R. DeShon (2003), Control of seafloor roughness on earthquake rupture behavior, *Geology*, *31*(5), 455–458.

Brune, J. N. (1970), Tectonic stress and the spectra of seismic shear waves from earthquakes, *J. Geophys. Res.*, *75*(26), 4997–5009.

Chouet, B., K. Aki, and M. Tsujiura (1978), Regional variation of the scaling law of earthquake source spectra, *Bull. Seism. Soc. Am.*, *68*(1), 49 – 79.

Choy, G. L., and J. L. Boatwright (1995), Global patterns of radiated seismic energy and apparent stress, *J. Geophys. Res.*, *100*(B9), 18,205–18,228.

Choy, G. L., A. McGarr, S. H. Kirby, and J. Boatwright (2006), An overview of the global variability in radiated energy and apparent stress, in *Earthquakes: Radiated Energy and the Physics of Faulting*, edited by R. Abercrombie, A. McGarr, H. Kanamori, and G. D. Toro, pp. 43–57, American Geophysical Union, Washington, DC.

Cloos, M. (1992), Thrust-type subduction-zone earthquakes and seamount asperities: a physical model for seismic rupture, *Geology*, *20*, 601–604.

DeShon, H. R., S. Y. Schwartz, A. V. Newman, V. González, M. Protti, L. M. Dorman, T. H. Dixon, D. E. Sampson, and E. R. Flueh (2006), Seismogenic zone structure beneath the Nicoya Peninsula, Costa Rica, from three-dimensional local earthquake *p*- and *s*- wave tomography, *Geophys. J. Int.*, *164*, 109–124, doi:10.1111/j.1365-246X.2005.02809.x.

Dominguez, S., J. Malavieille, and S. E. Lallemand (2000), Deformation of accretionary wedges in response to seamount subduction: Iinsights from sandbox experiments, *Tectonics*, *19*(1), 182–196.

Eken, T., K. Mayeda, A. Hofstetter, R. Gök, G. Örgülü, and N. Turkelli (2004), An application of the coda methodology for moment-rate spectra using broadband stations in Turkey, *Geophys. Res. Lett.*, *31*, doi: 10.1029/2004GL019627.

Fisher, A. T., C. A. Stein, R. N. Harris, K. Wang, E. A. Silver, M. Pfender, M. Hutnak, A. Cherkaoui, R. Bodzin, and H. Villinger (2003), Abrupt thermal transition reveals hydrothermal boundary and role of seamounts within the Cocos Plate, *Geophys. Res. Lett.*, *30*(11), 1550, doi: 10.1029/2002GL016766.

Fisher, D. M., T. W. Gardner, J. S. Marshall, and W. Montero (1994), Kinematics associated with late Cenozoic deformation in central Costa Rica: Western boundary of the Panama microplate, *Geology*, *22*, 263–266.

Fisher, D. M., T. W. Gardner, J. S. Marshall, P. B. Sak, and M. Protti (1998), Effects of subducting sea-floor roughness on fore-arc kinematics, Pacific coast, Costa Rica, *Geology*, *26*(5), 467–470.

Gardner, T., J. Marshall, D. Merritts, B. Bee, R. Burgette, E. Burton, J. Cooke, N. Kehrwald, M. Protti, D. Fisher, and P. Sak (2001), Holocene forearc block rotation in response to seamount subduction, southeastern Peninsula de Nicoya, Costa Rica, *Geology*, *29*(2), 151–154.

Ghosh, A., A. V. Newman, A. M. Thomas, and G. T. Farmer (2008), Interface locking along the subduction megatrust from *b*-value mapping near Nicoya Peninsula, Costa Rica, *Geophys. Res. Lett.*, *35*, L01301, doi: 10.1029/2007GL031617.

Gonzalez, V., and L. Persson (1997), Regional coda Q in Costa Rica, Central America, *Journal of Seismology*, *1*, 269–287.

Güendel, F., K. C. McNally, J. Lower, M. Protti, R. Sáenz, E. Malavassi, J. Barquero, R. V. der Laat, V. Gonzáles, C. Montero, E. Fernández, D. Rojas, J. de Dios Segura, A. Mata, and Y. Solís (1989), First results from a new seismographic network in Costa Rica, Central America, *Bull. Seism. Soc. Am.*, *79*(1), 205–210.

Hansen, S. E., S. Y. Schwartz, H. R. D. Shon, and V. González (2006), Earthquake relocation and focal mechanism determination using waveform cross correlation, Nicoya Peninsula, Costa Rica, *Bull. Seism. Soc. Am.*, *96*, doi: 10.1785012000129.

Harris, R. N., and K. Wang (2002), Thermal models of the Middle America Trench at the Nicoya Peninsula, Costa Rica, *Geophys. Res. Lett.*, *29*(21), 2010, doi:10.1029/2002GL015406.

Hey, R. (1977), Tectonic evolution of the Cocos-Nazca spreading center, *Geological Society of America Bulletin*, *88*, 1404–1420.

Hinz, K., R. von Huene, and C. R. Ranero (1996), Tectonic structure of the convergent Pacific margin offshore Costa Rica from multichannel seismic reflection data, *Tectonics*, *15*(1), 54–66.

Husen, S., E. Kissling, and R. Quintero (2002), Tomographic evidence for subducted seamount beneath the Gulf of Nicoya, Costa Rica: The cause of the 1990 Mw = 7.0 Gulf of Nicoya earthquake, *Geophys. Res. Lett.*, *29*(8), doi:10.1029/2001GL014045.

Kanamori, H., and L. Rivera (2004), Static and dynamic scaling relations for earthquakes and their implications for rupture speed and stress drop, *Bull. Seism. Soc. Am.*, *94*(1), 314–319.

Lundgren, P., M. Protti, A. Donnellan, M. Heflin, E. Hernandez, and D. Jefferson (1999), Seismic cycle and plate margin deformation in Costa Rica: GPS observations from 1994 to 1997, *J. Geophys. Res.*, *104*(B12), 28,915 – 28,926.

Malagnini, L., K. Mayeda, A. Akinci, and P. L. Bragato (2004), Estimating absolute site effects, *Bull. Seism. Soc. Am.*, *94*(4), 1343–1352.

Malagnini, L., P. Bodin, K. Mayeda, and A. Akinci (2006), Unbiased moment-rate spectra and absolute site effects in the Kachchh basin, India, from the analysis of the aftershocks of the 2001 Mw 7.6 Bhuj earthquake, *Bull. Seism. Soc. Am.*, *96*(2), doi:10.1785/0120050089.

Marshall, J. S., and R. S. Anderson (1995), Quaternary uplift and seismic cycle deformation, Peninsula de Nicoya, Costa Rica, *GSA Bulletin*, *107*(4), 463–473.

Mayeda, K. (1993), mb(LgCoda): A stable single station estimator of magnitude, *Bull. Seism. Soc. Am.*, *83*(3), 851–861.

Mayeda, K., and W. R. Walter (1996), Moment, energy, stress drop, and source spectra of western United States earthquakes from regional coda envelopes, *J. Geophys. Res.*, *101*(B5), 11,195–11,208.

Mayeda, K., A. Hofstetter, J. L. O'Boyle, and W. R. Walter (2003), Stable and transportable regional magnitudes based on coda-derived moment-rate spectra, *Bull. Seism. Soc. Am.*, *93*(1), 224 – 239.

Mayeda, K., R. Gök, W. R. Walter, and A. Hofstetter (2005), Evidence for non-constant energy/moment scaling from coda-derived source spectra, *Geophys. Res. Lett.*, *32*, L10306, doi:10.1029/2005GL022405.

Mayeda, K., L. Malagnini, and W. R. Walter (2007), A new spectral ratio method using narrow band coda envelopes: Evidence for non-self-similarity in the Hector Mine sequence, *Geophys. Res. Lett.*, *34*, L11303, doi:10.1029/2007GL030041.

McGarr, A. (1999), On relating apparent stress to the stress causing earthquake fault slip, *J. Geophys. Res.*, *104*(B2), 3003–3011.

Mochizuki, K., T. Yamada, M. Shinohara, Y. Yamanaka, and T. Kanazawa (2008), Weak interface coupling by seamounts and repeating m $\tilde{7}$ earthquakes, *Science*, *321*, 1194–1197.

Newman, A. V., S. Y. Schwartz, V. Gonzalez, H. R. DeShon, J. M. Protti, and L. M. Dorman (2002), Along-strike variability in the seismogenic zone below Nicoya Peninsula, Costa Rica, *Geophys. Res. Lett.*, *29*(20), doi: 10.1029/2002GL015409.

Norabuena, E., T. H. Dixon, S. Schwartz, H. DeShon, A. Newman, M. Protti, V. Gonzalez, L. Dorman, E. R. Flueh, P. Lundgren, F. Pollitz, and D. Sampson (2004), Geogedic and seismic constraints on some seismogenic zone processes in Costa Rica, *J. Geophys. Res.*, *109*, doi:10.1029/2003JB002931.

Park, J., T. Tsuru, Y. Kaneda, and Y. Kono (1999), A subducting seamount beneath the Nankai accretionary prism off Shikoku, southwestern Japan, *Geophys. Res. Lett.*, *26*(7), 931–934.

Phillips, W. S., and K. Aki (1986), Site amplification of coda waves from local earthquakes in central California, *Bull. Seism. Soc. Am.*, *76*(3), 627–648.

Phillips, W. S., R. J. Stead, G. E. Randall, H. E. Hartse, and K. M. Mayeda (2008), Source effects from broad area network calibration of regional distance coda waves, in *Scattering of Short Period Seismic Waves in the Heterogeneous Earth*, edited by H. Sato and M. C. Fehler, Elsevier, unpublished.

Press, W. H., S. A. Teukolsky, W. T. Vetterling, and B. P. Flannery (Eds.) (2007), *Numerical Recipes: The Art of Scientific Computing*, Cambridge University Press, 32 Avenue of the Americas, New York.

Protti, M., K. McNally, J. Pacheco, V. González, C. Montero, J. Segura, J. Brenes, V. Barboza, E. Malavassi, F. Güendel, G. Semila, D. Rojas, A. Velasco, A. Mata, and W. Schillinger (1995), The March 25, 1990 (M_w=7.0, M_l=6.8), earthquake at the entrance of the Nicoya Gulf, Costa Rica: Its prior activity, foreshocks, aftershocks, and triggered seismicity, *J. Geophys. Res.*, *100*(B10), 20,345–20,358.

Ranero, C. R., J. P. Morgan, K. McIntosh, and C. Reichert (2003), Bending-related faulting and mantle serpentinization at the Middle America trench, *Nature*, *425*, 367–373.

Rautian, T. G., and V. I. Khalturin (1978), The use of the coda for determination of the earthquake source spectrum, *Bull. Seism. Soc. Am.*, *68*(4), 923–948.

Scholz, C. H. (2002), *The mechanics of Earthquakes and Faulting*, 2nd ed., 54-55 pp., Cambridge Univ. Press, New York.

Scholz, C. H., and C. Small (1997), The effect of seamount subduction on seismic coupling, *Geology*, *25*(6), 487–490.

Schwartz, S. Y., and H. R. DeShon (2007), Distinct updip limits to geodetic locking and microseismicity at the northern Costa Rica seismogenic zone, in *The seismogenic zone of subduction thrust faults*, edited by T. H. Dixon and J. C. Moore, pp. 576–599, Columbia University Press, New York.

Silver, E., M. Kastner, A. Fisher, J. Morris, K. McIntosh, and D. Saffer (2000), Fluid flow paths in the Middle America Trench and Costa Rica margin, *Geology*, *28*(8), 679–682.

Small, C., and D. Abbott (1998), Subduction obstruction and the crack-up of the Pacific plate, *Geology*, *26*(9), 795–798.

Spinelli, G. A., and D. M. Saffer (2004), Along-strike variations in underthurst sediment dewatering on the Nicoya margin, Costa Rica related

to the updip limit of seismicity, *Geophys. Res. Lett.*, *31*, L04613, doi: 10.1029/2003GL018863.

Spinelli, G. A., D. M. Saffer, and M. B. Underwood (2006), Hydrogeologic responses to three-dimensional temperature variability, Costa Rica subduction margin, *J. Geophys. Res.*, *111*, B04403, doi:10.1029/2004JB003436.

Street, R. L., R. B. Herrmann, and O. W. Nuttli (1975), Spectral characteristics of the Lg wave generated by central United States earthquakes, *Geophys. J. R. Astr. Soc.*, *41*, 51 – 63.

Taylor, S. R., and H. E. Hartse (1998), A procedure for estimation of source and propagation amplitude corrections for regional seismic discriminants, *J. Geophys. Res.*, *103*(B2), 2781–2789.

Um, J., and C. Thurber (1987), A fast algorithm for two-point seismic ray tracing, *Bull. Seism. Soc. Am.*, *77*(3), 972–986.

von Huene, R. (2008), When seamounts subduct, *Science*, *321*, 1165–1166.

von Huene, R., C. R. Ranero, and W. Weinrebe (2000), Quaternary convergent margin tectonics of Costa Rica, segmentation of the Cocos Plate, and Central American volcanism, *Tectonics*, *19*(2), 314 – 334.

Walter, W. R., and S. R. Taylor (2001), A revised magnitude and distance amplitude correction (MDAC2) procedure for regional seismic discriminants: theory and testing at NTS, pp. UCRL–ID–146,882, Lawrence Livermore National Laboratory Report.

Walter, W. R., K. Mayeda, R. Gok, and A. Hofstetter (2006), The scaling of seismic energy with moment: Simple models compared with observations, in *Earthquakes: Radiated Energy and the Physics of Faulting*, edited by R. Abercrombie, A. McGarr, H. Kanamori, and G. D. Toro, pp. 25–41, American Geophysical Union, Washington, DC.

Werner, R., K. Hoernle, P. van den Bogaard, C. Ranero, R. von Huene, and D. Korich (1999), Drowned 14-m.y.-old Galapagos archipelago off the coast of Costa Rica: Implications for tectonic and evolutionary models, *Geology*, *27*(6), 499–502.

Wyss, M., and P. Molnar (1972), Efficiency, stress drop, apparent stress, effective stress, and frictional stress of Denver, Colorado, earthquakes, *J. Geophys. Res.*, *77*(8), 1433–1438.

Ye, S., J. Bialas, E. R. Flueh, A. Stavenhagen, R. von Huene, G. Leandro, and K. Hinz (1996), Crustal structure of the Middle American Trench off Costa Rica from wide-angle seismic data, *Tectonics*, *15*(5), 1006–1021.

APPENDIX A

Appendix A

A.1 Source parameter results

This section contains detailed listing of constrained results for 353 well calibrated events from the CR-SEIZE dataset. After the calibration procedure, I had over 1,300 earthquakes with estimated source parameters. Out of these, I selected only events that had at least 3 calibrated bands above and below the corner frequency, which brought the count down to 353 events. The selected events are listed in A.1 based on their event location identification number. Included in the table are the location parameters: latitude, longitude, depth and original magnitude M_L. The M_L was set to -999.0 for earthquakes that did not have M_L in original database. The time, location and original M_L of processed earthquakes come from A. Newman (personal communication). The units on seismic moment (M_0), S-wave corner frequency (ω_{cS}) and apparent stress (σ_a) are given in the table header. The units of the error values for these results are the same as the unit they refer to.

Table A.1: Results for M_0, ω_c, and σ_a

Date	Time	Evid	Lat	Lon	Depth (km)	log M_0 (Nm)	ω_{cS} (Hz)	σ_a (MPa)	err σ_a	err M_0	err ω_{cS}	M_L	M_0
1999/12/09	06:50:25	2528	9.9263	-85.4433	20.29	13.91	5.2990	0.97949	0.10700	0.00503	0.0137	3.110	3.2401
1999/12/09	06:52:47	18265	9.9246	-85.4405	19.97	13.49	8.0500	1.64816	0.10310	0.00640	0.0181	2.620	2.9601
1999/12/09	07:06:56	2530	9.9226	-85.4461	20.36	13.53	5.9180	0.69663	0.10080	0.00537	0.0141	2.510	2.9867
1999/12/09	07:18:05	2531	9.9262	-85.4444	19.71	12.71	10.6100	0.97724	0.10830	0.00756	0.0245	2.180	2.4401
1999/12/09	07:24:33	2532	9.9231	-85.4470	20.51	13.69	5.6880	0.82985	0.09861	0.00517	0.0142	2.790	3.0934
1999/12/09	07:33:30	2534	9.9215	-85.4442	20.33	12.82	7.3960	0.40272	0.11740	0.00726	0.0220	2.150	2.5134
1999/12/09	07:34:37	2535	9.9246	-85.4436	19.85	13.29	7.7630	1.05196	0.11960	0.00612	0.0165	2.370	2.8267
1999/12/09	07:53:12	2536	9.9238	-85.4349	19.23	12.17	11.7200	0.51761	0.13600	0.00983	0.0321	2.130	2.0801
1999/12/09	08:05:54	2537	9.9298	-85.4383	18.63	12.12	9.5810	0.26242	0.14850	0.00932	0.0321	2.250	2.0467
1999/12/09	08:15:34	2538	9.9150	-85.4493	20.65	12.19	11.0500	0.45082	0.11690	0.00954	0.0315	2.160	2.0934
1999/12/09	08:26:08	2539	9.9200	-85.4398	20.79	12.37	12.4600	0.88716	0.14820	0.00938	0.0359	-999.0	2.2134
1999/12/09	20:27:18	2543	9.9225	-85.4430	22.78	13.28	8.1880	1.21339	0.10870	0.00667	0.0195	2.270	2.8201
1999/12/09	22:34:00	2544	9.9275	-85.4466	20.48	12.63	14.1400	2.01372	0.13970	0.00929	0.0394	1.940	2.3867
1999/12/10	00:03:13	2545	9.9287	-85.4391	19.49	12.67	13.7400	1.98609	0.12480	0.00825	0.0324	2.220	2.4134
1999/12/10	01:21:13	2546	9.9243	-85.4452	20.62	12.06	9.0800	0.20184	0.12940	0.01105	0.0381	2.210	2.0067
1999/12/10	08:26:12	2787	9.8334	-85.2871	19.63	11.89	12.5300	0.38994	0.09934	0.01146	0.0408	2.020	1.8934
1999/12/10	13:49:29	2549	9.9237	-85.4347	19.03	12.40	10.2500	0.51880	0.12730	0.01083	0.0395	2.150	2.2334
1999/12/11	07:49:57	2802	9.8897	-85.2185	23.39	11.43	10.9200	0.11668	0.08392	0.02041	0.0731	1.590	1.5867
1999/12/15	03:09:18	2848	9.8896	-85.3070	25.51	11.77	12.8800	0.34514	0.16620	0.01406	0.0539	1.390	1.8134
1999/12/15	09:32:42	2574	9.8329	-85.3973	14.50	12.43	7.3850	0.20512	0.09084	0.00678	0.0207	2.230	2.2534
1999/12/16	06:31:12	2667	9.9288	-85.4278	19.74	11.78	9.7900	0.15417	0.14370	0.01268	0.0466	-999.0	1.8201
1999/12/21	14:44:32	2954	10.1317	-85.6946	22.12	13.35	9.2190	1.93642	0.11780	0.00724	0.0207	2.620	2.8667
1999/12/22	16:16:25	2960	10.1874	-85.7156	25.38	11.97	13.5900	0.57810	0.11940	0.01719	0.0662	1.700	1.9467
1999/12/22	16:42:54	18727	9.9647	-85.6279	23.03	12.40	8.3340	0.27925	0.14670	0.01193	0.0358	1.860	2.2334
1999/12/23	00:36:20	2963	10.0992	-85.6873	27.51	15.25	2.9890	1.77828	0.07286	0.00349	-0.0104	4.110	4.1334
1999/12/23	01:15:36	3296	10.1245	-85.6445	34.23	13.91	10.1400	6.79204	0.08372	0.02921	0.0793	2.420	3.2401
1999/12/23	01:15:51	3295	10.1477	-85.6254	34.95	13.54	8.6240	2.21820	0.09622	0.00649	0.0177	2.540	2.9934
1999/12/23	01:22:41	2964	10.0913	-85.6851	26.60	12.38	11.8000	0.75858	0.11590	0.00966	0.0353	1.890	2.2201
1999/12/23	07:57:43	18752	9.9936	-85.5694	12.45	12.62	6.4620	0.18880	0.13320	0.00799	0.0249	2.490	2.3801
1999/12/24	15:17:12	2978	10.1015	-85.6536	21.84	12.17	12.3600	0.61094	0.14510	0.01696	0.0500	1.810	2.0801
1999/12/25	14:09:55	2979	10.1191	-85.6647	24.85	12.79	9.5790	0.83368	0.10170	0.00857	0.0260	2.090	2.4934
1999/12/25	14:14:25	18737	10.0976	-85.6438	20.04	12.13	10.8400	0.38194	0.10920	0.01444	0.0445	1.160	2.0534
1999/12/26	05:14:27	2983	10.0036	-85.4912	19.09	12.93	6.6670	0.35645	0.12520	0.00658	0.0188	2.070	2.5867
1999/12/27	03:25:49	18741	9.9582	-85.6408	18.56	14.11	4.4150	0.79800	0.12930	0.00448	0.0123	2.990	3.3734
1999/12/27	03:36:38	3484	9.6507	-84.9233	17.69	12.73	11.8100	1.40281	0.12660	0.01285	0.0484	2.350	2.4534

Date	Time	Evid	Lat	Lon	Depth (km)	log M_0 (Nm)	ω_{cS} (Hz)	σ_a (MPa)	err σ_a	err M_0	err ω_{cS}	M_L	M_0
1999/12/27	10:28:14	3487	9.7388	-85.1883	20.12	12.28	15.9000	1.56675	0.21280	0.01896	0.0707	-999.0	2.1534
1999/12/27	12:25:09	18744	9.9658	-85.6405	18.10	14.06	6.9030	2.77332	0.10810	0.00608	0.0155	3.070	3.3401
1999/12/30	05:14:28	3392	10.1735	-85.7269	27.19	12.25	13.7000	0.95061	0.11570	0.01245	0.0530	1.430	2.1334
1999/12/31	03:43:24	3397	9.9363	-85.3052	31.92	12.63	13.8000	1.90108	0.10490	0.01081	0.0415	2.110	2.3867
2000/01/01	02:40:17	66509	9.6762	-84.9851	19.67	12.32	9.6870	0.38371	0.09932	0.01816	0.0602	1.960	2.1801
2000/01/02	11:36:41	66528	10.1960	-85.7205	25.02	13.09	9.2890	1.27938	0.08463	0.00737	0.0217	2.260	2.6934
2000/01/02	12:43:47	66332	9.9336	-85.6545	19.62	12.58	9.0130	0.47973	0.13980	0.00841	0.0267	1.810	2.3534
2000/01/03	00:27:26	66582	9.9176	-85.4468	20.38	13.26	8.6810	1.38357	0.13320	0.00685	0.0193	2.490	2.8067
2000/01/04	07:07:13	66602	9.9223	-85.2515	28.96	12.09	12.3600	0.53580	0.17410	0.01285	0.0433	1.760	2.0267
2000/01/04	14:09:58	66556	10.3650	-85.8707	26.88	12.34	16.6400	1.99986	0.11480	0.01188	0.0554	1.660	2.1934
2000/01/04	21:32:06	66342	10.3501	-85.8534	27.01	13.18	12.7000	3.79315	0.10840	0.00846	0.0302	2.350	2.7534
2000/01/06	20:08:05	66407	9.8963	-85.4444	19.01	12.23	10.1200	0.36983	0.09063	0.01583	0.0546	1.820	2.1201
2000/01/08	10:14:40	66608	10.3725	-85.5075	45.90	12.78	14.9100	3.06902	0.09229	0.00932	0.0363	1.720	2.4867
2000/01/09	20:12:59	66610	9.8512	-85.3426	23.81	13.15	9.8610	1.70216	0.08844	0.00821	0.0257	2.170	2.7334
2000/01/13	02:27:48	51366	10.2892	-85.8761	21.67	12.32	12.0200	0.72444	0.10720	0.01220	0.0460	2.060	2.1801
2000/01/14	03:19:05	66699	9.9052	-85.4368	21.10	12.19	14.1800	0.96161	0.09628	0.01408	0.0610	2.240	2.0934
2000/01/19	17:34:09	65565	10.4331	-85.6211	47.57	13.68	14.1800	12.58930	0.11290	0.00770	0.0296	2.490	3.0867
2000/01/26	09:08:42	66201	10.2595	-85.7742	19.77	12.38	9.2920	0.37325	0.14290	0.00799	0.0254	1.880	2.2201
2000/01/27	05:05:06	66206	10.0791	-85.5111	31.30	11.82	12.9400	0.38637	0.15060	0.01353	0.0492	2.140	1.8467
2000/01/29	07:44:18	65874	9.8948	-85.3558	19.46	12.31	14.4600	1.23880	0.12570	0.00892	0.0344	-999.0	2.1734
2000/01/29	11:26:12	66242	10.0161	-85.5488	8.52	12.11	8.4790	0.17742	0.09520	0.01103	0.0363	2.010	2.0401
2000/01/29	13:04:24	51874	10.3234	-85.8540	25.46	12.71	16.9700	4.00867	0.12580	0.01064	0.0509	1.860	2.4401
2000/01/30	05:52:34	66246	9.7656	-85.1907	19.33	11.81	13.7600	0.45499	0.09977	0.01278	0.0512	-999.0	1.8401
2000/01/30	22:11:53	66775	9.8863	-85.3594	18.98	12.42	17.2900	2.57040	0.12880	0.00951	0.0472	2.280	2.2467
2000/02/01	22:11:43	51521	9.8802	-85.3575	20.13	12.95	10.3300	1.38357	0.10830	0.00756	0.0236	2.230	2.6001
2000/02/02	05:33:38	66285	9.9111	-85.3412	18.91	11.88	14.6800	0.62374	0.08398	0.01157	0.0490	1.720	1.8867
2000/02/03	03:57:48	66294	9.9774	-85.5766	11.82	12.00	12.2900	0.45082	0.09121	0.01183	0.0412	1.600	1.9667
2000/02/08	18:42:25	66799	10.2543	-85.8454	23.15	12.87	11.7100	1.74582	0.11160	0.01073	0.0354	2.330	2.5467
2000/02/10	01:19:05	65924	10.0080	-85.6561	18.53	12.58	13.2200	1.52757	0.20340	0.00874	0.0316	2.470	2.3534
2000/02/10	06:20:54	67116	9.5879	-84.8180	28.36	12.14	10.4700	0.35075	0.28310	0.01650	0.0557	1.960	2.0601
2000/02/10	09:05:40	65926	10.3606	-85.8879	27.87	13.20	11.7900	3.16957	0.11710	0.00712	0.0222	2.330	2.7667
2000/02/11	08:42:33	65930	10.2526	-85.7720	27.09	13.28	10.2000	2.33346	0.10070	0.00653	0.0188	2.350	2.8201
2000/02/14	01:53:32	65940	10.5636	-85.9798	38.70	13.18	12.2000	3.34965	0.09609	0.00762	0.0250	2.490	2.7534
2000/02/14	10:01:35	66818	9.5759	-84.9176	21.01	12.16	11.6400	0.50234	0.08406	0.01370	0.0488	1.490	2.0734
2000/02/17	00:01:41	65964	10.2262	-85.6201	41.30	13.47	15.0000	10.25650	0.09088	0.00662	0.0245	2.360	2.9467

Date	Time	Evid	Lat	Lon	Depth (km)	log M_0 (Nm)	ω_{cS} (Hz)	σ_a (MPa)	err σ_a	err M_0	err ω_{cS}	M_L	M_0
2000/02/17	05:53:41	65966	9.9343	-85.4608	20.77	12.17	13.2500	0.74989	0.12570	0.00888	0.0341	2.450	2.0801
2000/02/21	10:05:38	66847	10.0815	-85.6708	21.11	12.38	12.7600	0.96161	0.11000	0.01081	0.0393	1.800	2.2201
2000/02/24	13:16:07	66854	9.9479	-85.5246	34.90	13.06	15.8200	5.92925	0.13150	0.00719	0.0291	2.440	2.6734
2000/02/28	17:47:55	66034	9.8786	-85.3141	19.36	12.70	12.5600	1.61436	0.21390	0.00800	0.0270	2.550	2.4334
2000/03/01	07:02:27	66877	9.8291	-85.3513	16.81	11.98	10.1400	0.24547	0.14140	0.01075	0.0355	2.540	1.9534
2000/03/02	04:02:23	66048	9.6061	-84.7692	16.58	13.67	4.2910	0.34356	0.10810	0.00435	0.0120	2.880	3.0801
2000/03/02	19:22:29	66050	9.9292	-85.4362	18.77	12.56	12.7600	1.31220	0.14510	0.00885	0.0319	1.970	2.3401
2000/03/04	06:01:32	49860	9.8559	-85.3311	18.84	13.14	6.8740	0.56624	0.11990	0.00450	0.0117	2.390	2.7267
2000/03/04	06:11:52	35322	9.8665	-85.3231	16.80	12.08	15.9800	1.14025	0.13730	0.00978	0.0400	2.310	2.0201
2000/03/04	08:22:18	49794	9.8552	-85.3357	19.05	11.91	11.0400	0.27606	0.12290	0.01235	0.0398	1.930	1.9067
2000/03/05	10:48:06	50709	9.5637	-84.9192	19.46	12.31	11.0200	0.55590	0.16640	0.01278	0.0433	2.360	2.1734
2000/03/05	12:36:22	35231	9.5851	-85.1993	19.43	12.54	12.5900	1.22462	0.13510	0.00921	0.0351	2.190	2.3267
2000/03/06	06:07:12	35237	9.5973	-84.8957	22.84	12.73	13.0800	1.91426	0.09676	0.01073	0.0415	2.390	2.4534
2000/03/06	23:46:48	35434	9.9110	-85.4390	17.87	12.23	9.5650	0.31405	0.11860	0.01148	0.0405	2.170	2.1201
2000/03/07	23:14:13	35245	9.7710	-85.1461	15.32	12.54	6.5840	0.17458	0.11270	0.00883	0.0323	2.290	2.3267
2000/03/08	13:14:59	35474	10.1644	-85.7322	22.68	11.99	13.2300	0.54702	0.22690	0.01874	0.0636	2.090	1.9601
2000/03/09	05:18:54	35492	9.7415	-85.2829	16.28	12.01	11.3200	0.35810	0.13690	0.01256	0.0379	2.030	1.9734
2000/03/11	16:12:21	35275	9.7736	-85.0576	19.11	12.78	8.8420	0.63974	0.16500	0.00774	0.0238	2.400	2.4867
2000/03/12	02:25:31	35277	9.8649	-85.2192	18.58	12.67	13.5400	1.90108	0.16510	0.00749	0.0290	2.410	2.4134
2000/03/12	10:23:43	49779	10.2539	-85.8710	23.00	12.79	11.9600	1.61065	0.09238	0.00693	0.0227	2.120	2.4934
2000/03/15	04:25:58	35654	10.0359	-85.5737	16.79	13.35	6.8600	0.79983	0.08786	0.00474	0.0128	2.320	2.8667
2000/03/16	04:31:20	35679	10.2864	-85.8769	22.19	12.71	13.6400	2.08930	0.10990	0.00782	0.0300	2.090	2.4401
2000/03/16	11:32:31	35690	9.5995	-85.0169	16.82	12.25	9.2630	0.29512	0.40250	0.01161	0.0386	2.130	2.1334
2000/03/17	01:30:56	35713	10.1981	-85.7215	23.53	12.14	16.4300	1.35831	0.12520	0.01034	0.0464	1.530	2.0601
2000/03/20	11:50:14	35913	10.2648	-85.8305	19.41	13.04	6.7600	0.45186	0.10950	0.00575	0.0158	2.350	2.6601
2000/03/20	11:52:48	50281	9.9182	-85.2344	19.71	12.68	7.4900	0.32734	0.13080	0.00927	0.0312	2.390	2.4201
2000/03/23	07:42:01	50295	9.9040	-85.4055	21.18	12.74	10.5900	1.02094	0.10620	0.00627	0.0191	2.630	2.4601
2000/03/23	19:25:57	50301	9.5517	-84.5891	17.75	13.39	7.7090	1.21899	0.10180	0.00677	0.0211	2.810	2.8934
2000/03/25	15:11:34	50317	9.5841	-84.7158	17.15	13.11	5.7730	0.31478	0.11960	0.00718	0.0221	2.360	2.7067
2000/03/27	06:28:23	50327	10.4839	-85.8774	37.22	13.14	13.8400	4.54988	0.10750	0.00646	0.0240	2.400	2.7267
2000/03/27	16:11:23	50329	10.2362	-85.8189	24.54	13.23	7.1060	0.72946	0.11470	0.00515	0.0133	2.560	2.7867
2000/03/27	16:50:40	50331	9.8211	-85.2114	18.99	12.32	12.9500	0.90365	0.15120	0.01066	0.0387	2.300	2.1801
2000/03/28	08:31:40	50337	9.6557	-85.2511	18.95	12.34	9.0270	0.31989	0.13810	0.00785	0.0242	2.390	2.1934
2000/03/28	17:19:50	50343	9.6497	-84.8610	14.94	12.76	9.4080	0.74645	0.14620	0.01077	0.0373	2.840	2.4734
2000/03/29	22:16:39	50345	9.6721	-85.1544	18.72	12.86	11.5000	1.62181	0.14490	0.00801	0.0298	2.470	2.5401

Date	Time	Evid	Lat	Lon	Depth (km)	log M_0 (Nm)	ω_{cS} (Hz)	σ_a (MPa)	err σ_a	err M_0	err ω_{cS}	M_L	M_0
2000/03/29	22:54:20	50347	9.6765	-85.1429	19.92	12.56	14.2900	1.85780	0.12160	0.01036	0.0487	2.030	2.3401
2000/03/30	03:37:25	50355	9.6685	-85.1560	17.97	13.41	7.9820	1.39959	0.11860	0.00500	0.0136	2.790	2.9067
2000/03/31	21:44:34	50369	9.6913	-85.1857	17.96	13.17	4.4400	0.16032	0.15250	0.00462	0.0143	2.300	2.7467
2000/03/31	21:48:32	50371	9.6794	-85.1838	19.14	13.42	6.2340	0.68234	0.10420	0.00486	0.0134	2.580	2.9134
2000/03/31	23:17:31	50375	9.6740	-85.1875	18.98	12.54	15.1800	2.13304	0.16460	0.01024	0.0475	2.100	2.3267
2000/04/01	05:49:35	50381	9.6659	-85.1979	18.59	12.59	9.9750	0.66527	0.10870	0.00752	0.0237	2.180	2.3601
2000/04/03	05:03:02	50399	9.5840	-84.8122	18.11	13.14	5.1540	0.23714	0.12890	0.00560	0.0178	2.880	2.7267
2000/04/03	05:24:57	50401	9.5823	-84.7627	20.51	12.97	7.8600	0.62951	0.09988	0.00738	0.0228	2.700	2.6134
2000/04/10	18:26:10	50434	9.6660	-85.1600	16.77	13.01	8.7140	0.90991	0.12840	0.00710	0.0219	3.150	2.6401
2000/04/11	17:08:42	36018	9.9576	-85.6617	19.20	12.38	13.3700	1.11173	0.15820	0.01008	0.0397	1.870	2.2201
2000/04/15	21:01:39	36039	9.5708	-84.8430	16.23	13.49	7.5470	1.36458	0.10480	0.00648	0.0190	2.750	2.9601
2000/04/16	00:40:01	50450	9.9183	-85.3731	19.19	13.08	11.3800	2.29615	0.12450	0.00620	0.0197	2.350	2.6867
2000/04/18	09:03:27	36047	9.6530	-84.8974	17.75	12.71	7.4200	0.33729	0.15290	0.00715	0.0205	2.750	2.4401
2000/04/20	05:49:55	50455	9.5537	-84.7839	17.87	12.59	10.3100	0.73621	0.12820	0.00983	0.0355	2.580	2.3601
2000/04/25	06:46:02	50469	9.8986	-85.4114	18.48	12.38	10.9800	0.62087	0.11360	0.00727	0.0229	2.030	2.2201
2000/04/25	17:45:34	36078	10.0091	-85.6294	18.86	12.79	12.0800	1.66341	0.11540	0.00697	0.0231	1.900	2.4934
2000/04/26	01:06:41	50473	9.6777	-85.1994	18.83	12.16	14.4200	0.95499	0.15350	0.01057	0.0442	2.100	2.0734
2000/04/29	14:35:02	50489	9.9150	-85.4403	20.67	12.57	16.1600	2.74157	0.20150	0.00964	0.0435	2.150	2.3467
2000/04/30	05:58:39	36100	10.3679	-85.9197	25.64	12.46	11.0700	0.72778	0.16260	0.00861	0.0297	2.000	2.2734
2000/05/01	05:29:46	50497	9.6176	-85.1591	15.40	12.33	7.8520	0.20701	0.12360	0.00836	0.0277	2.430	2.1867
2000/05/01	11:16:41	36107	9.9500	-85.3277	23.69	12.08	14.3600	0.82414	0.13140	0.00970	0.0415	2.460	2.0201
2000/05/05	04:14:41	50508	9.6510	-84.9123	19.10	12.82	7.3550	0.39355	0.10520	0.00640	0.0208	2.460	2.5134
2000/05/05	16:10:45	50514	9.9503	-85.4551	19.08	12.56	9.5690	0.55208	0.12740	0.00730	0.0240	1.830	2.3401
2000/05/06	05:48:07	50519	9.6771	-85.2032	18.88	12.05	8.9970	0.19320	0.14550	0.00892	0.0288	2.230	2.0001
2000/05/07	16:42:00	36138	9.6041	-85.2132	18.64	12.87	9.5560	0.95280	0.12270	0.00719	0.0230	2.630	2.5467
2000/05/07	17:48:55	50526	9.9655	-85.6585	20.05	12.97	9.5910	1.14288	0.14670	0.00705	0.0204	2.460	2.6134
2000/05/08	00:37:37	50528	10.2257	-85.7660	25.93	12.27	16.0100	1.57761	0.11770	0.00952	0.0443	2.120	2.1467
2000/05/10	15:51:33	50534	9.9057	-85.2857	28.60	14.14	6.2480	2.36048	0.14290	0.00388	0.0095	3.040	3.3934
2000/05/12	12:31:55	36165	10.2320	-85.8397	22.45	13.13	8.5780	1.07399	0.15950	0.00575	0.0161	2.590	2.7201
2000/05/13	05:40:31	50554	10.0088	-85.5221	17.39	12.26	10.1300	0.39265	0.12710	0.00961	0.0300	-999.0	2.1401
2000/05/14	12:11:59	36186	9.9215	-85.2370	19.62	12.39	11.5500	0.73621	0.10490	0.00851	0.0282	2.390	2.2267
2000/05/14	12:13:57	50569	9.9817	-85.5761	14.81	12.57	10.1200	0.66374	0.13560	0.00675	0.0215	2.170	2.3467
2000/05/17	08:27:39	50595	10.0711	-85.4135	35.52	13.55	9.4410	2.97852	0.10080	0.00485	0.0135	2.750	3.0001
2000/05/17	16:47:38	50598	9.8968	-85.3546	20.54	13.55	5.3280	0.52723	0.14200	0.00373	0.0098	2.460	3.0001
2000/05/17	19:15:45	50600	9.5621	-84.8450	18.45	13.23	6.3120	0.50699	0.10300	0.00611	0.0190	2.960	2.7867

Date	Time	Evid	Lat	Lon	Depth (km)	log M_0 (Nm)	ω_{cS} (Hz)	σ_a (MPa)	err σ_a	err M_0	err ω_{cS}	M_L	M_0
2000/05/19	15:12:46	50842	9.7658	-85.0322	21.03	12.82	9.5070	0.85704	0.10680	0.00702	0.0216	2.610	2.5134
2000/05/21	10:36:38	35802	9.6854	-85.2115	18.74	12.70	6.5580	0.22856	0.10540	0.00579	0.0181	2.520	2.4334
2000/05/21	12:42:15	35812	10.1440	-85.6963	21.62	11.99	13.5800	0.59703	0.12070	0.01121	0.0417	2.130	1.9601
2000/05/21	14:24:33	35816	10.1561	-85.6925	20.63	12.80	9.7480	0.89536	0.11020	0.00683	0.0219	2.020	2.5001
2000/05/23	03:30:55	50224	10.1503	-85.7027	21.55	12.46	12.3800	1.00925	0.10250	0.00793	0.0280	2.130	2.2734
2000/05/24	05:59:39	50257	9.6918	-85.1623	17.69	12.26	6.7020	0.11455	0.13430	0.00728	0.0228	2.540	2.1401
2000/05/28	06:04:13	50650	9.8573	-85.3477	18.77	12.72	10.5500	0.99083	0.12120	0.00651	0.0202	2.100	2.4467
2000/06/01	03:01:38	36911	9.5858	-85.2236	19.00	12.18	13.0500	0.73282	0.13180	0.01238	0.0474	2.570	2.0867
2000/06/01	05:51:17	36300	9.9546	-85.3460	22.09	12.39	11.3600	0.69343	0.26700	0.00743	0.0240	3.060	2.2267
2000/06/02	03:37:32	36934	9.5845	-84.9455	19.47	12.09	9.8130	0.26792	0.39380	0.01039	0.0339	2.760	2.0267
2000/06/02	06:10:54	50663	9.9126	-85.3028	21.67	12.17	11.3500	0.46989	0.08561	0.00949	0.0401	3.230	2.0801
2000/06/02	07:29:47	50665	9.5595	-84.7016	16.20	13.60	6.2890	0.94842	0.10980	0.00485	0.0122	2.800	3.0334
2000/06/03	05:28:49	36309	10.2468	-85.7613	26.35	13.31	8.2470	1.29122	0.11710	0.00517	0.0145	2.280	2.8401
2000/06/03	05:29:52	36402	10.2507	-85.7608	26.05	12.34	13.1800	1.00000	0.11020	0.01128	0.0374	1.270	2.1934
2000/06/03	13:58:43	36810	10.4560	-85.9854	25.22	12.64	10.3500	0.80538	0.11080	0.00934	0.0345	2.390	2.3934
2000/06/04	01:43:27	50674	9.9103	-85.2338	19.01	12.19	10.4300	0.38019	0.10660	0.00921	0.0304	2.750	2.0934
2000/06/05	03:02:58	50677	10.3427	-85.8987	28.87	12.74	14.4300	2.63027	0.21310	0.00754	0.0289	2.210	2.4601
2000/06/05	05:48:11	50679	10.2631	-85.8373	20.70	12.39	11.9600	0.81658	0.17520	0.00802	0.0266	1.950	2.2267
2000/06/07	08:07:11	36334	10.3475	-85.9019	25.22	12.62	15.9000	2.80543	0.09285	0.00842	0.0361	2.120	2.3801
2000/06/07	15:15:04	36336	9.5416	-84.7774	16.70	13.45	6.8140	0.93325	0.10750	0.00569	0.0152	2.700	2.9334
2000/06/08	06:15:18	50688	10.2052	-85.7874	23.94	11.84	15.8100	0.72778	0.11890	0.01140	0.0452	2.180	1.8601
2000/06/09	10:13:22	50696	10.3467	-85.9036	25.18	13.10	9.5490	1.40605	0.10680	0.00572	0.0164	2.510	2.7001
2000/06/10	12:08:05	50706	9.6487	-85.2126	17.47	12.91	6.4440	0.31333	0.12570	0.00526	0.0161	2.280	2.5734
2000/06/16	06:13:56	18502	9.5062	-84.8197	24.42	12.62	9.9280	0.69502	0.11170	0.00819	0.0266	2.390	2.3801
2000/06/17	02:11:49	18526	9.9160	-85.4455	20.40	12.39	11.6500	0.74302	0.10990	0.00748	0.0261	2.480	2.2267
2000/06/18	04:07:39	1	9.9107	-85.3957	17.15	12.49	14.0000	1.53462	0.12220	0.00764	0.0296	2.440	2.2934
2000/06/20	02:16:01	18314	9.5632	-84.9752	11.80	12.28	9.0160	0.28642	0.13330	0.01009	0.0347	2.350	2.1534
2000/06/22	13:00:12	18333	9.9993	-85.4614	30.98	12.34	15.6500	1.66341	0.13040	0.00838	0.0349	1.890	2.1934
2000/06/22	13:09:50	3838	9.8498	-85.2527	17.28	12.43	10.1200	0.52481	0.12060	0.00856	0.0302	2.610	2.2534
2000/06/23	06:17:18	3916	9.8088	-85.2455	23.42	11.85	13.8300	0.48865	0.13780	0.01000	0.0377	2.480	1.8667
2000/06/24	09:43:07	36	9.7191	-85.0282	18.71	12.05	10.7800	0.32810	0.11380	0.01016	0.0340	2.400	2.0001
2000/06/24	15:41:39	39	10.2274	-85.8343	22.87	12.58	14.5300	2.02768	0.21610	0.00882	0.0357	2.450	2.3534
2000/06/25	07:19:17	3988	9.6771	-85.1230	21.96	11.73	15.7200	0.59293	0.11980	0.01282	0.0562	2.200	1.7867
2000/06/25	07:33:00	3989	9.6013	-84.9536	19.98	11.96	12.2200	0.40926	0.07854	0.01151	0.0412	1.910	1.9401
2000/06/25	09:34:38	18400	9.8708	-85.4008	19.38	11.74	14.0900	0.43451	0.13940	0.01173	0.0439	1.930	1.7934

Date	Time	Evid	Lat	Lon	Depth (km)	log M_0 (Nm)	ω_{cS} (Hz)	σ_a (MPa)	err σ_a	err M_0	err ω_{cS}	M_L	M_0
2000/06/26	02:10:07	47	9.6318	-85.0371	14.93	12.78	7.7150	0.42855	0.11180	0.00650	0.0197	2.310	2.4867
2000/06/27	07:48:11	18455	9.6757	-85.1049	22.38	12.29	11.2100	0.55976	0.35360	0.00927	0.0330	2.560	2.1601
2000/06/27	23:03:41	57	9.6175	-84.7790	18.13	13.03	7.3100	0.56234	0.12830	0.00751	0.0243	2.770	2.6534
2000/06/28	03:14:11	58	9.6824	-85.1181	20.42	14.03	4.4110	0.69024	0.09971	0.00339	0.0083	3.070	3.3201
2000/06/28	19:44:57	3569	9.9283	-85.3040	21.97	12.03	12.0800	0.45082	0.13940	0.01695	0.0598	2.070	1.9867
2000/06/29	10:09:33	69	9.5782	-85.1861	14.63	12.05	8.7290	0.17418	0.14800	0.01452	0.0454	1.820	2.0001
2000/06/29	18:02:14	3590	10.0599	-85.4914	16.01	12.44	3.4220	0.02084	0.11950	0.00900	0.0462	1.500	2.2601
2000/06/30	03:30:18	18285	9.6595	-84.8838	19.31	12.75	12.1100	1.55597	0.10540	0.00865	0.0336	2.310	2.4667
2000/06/30	08:35:40	3611	10.3571	-85.6680	36.33	11.88	14.0200	0.53827	0.16370	0.01097	0.0418	1.970	1.8867
2000/06/30	10:06:39	78	10.3839	-85.9878	24.00	13.55	4.0860	0.23768	0.10930	0.00369	0.0105	2.470	3.0001
2000/06/30	16:46:25	3623	9.6697	-85.0219	14.26	12.35	9.5590	0.38459	0.16190	0.01072	0.0372	1.850	2.2001
2000/06/30	22:35:48	83	9.6007	-85.1870	16.03	12.35	8.0310	0.22962	0.17130	0.01459	0.0494	2.160	2.2001
2000/07/02	07:51:32	1884	9.9943	-85.6596	12.81	12.18	10.3100	0.36058	0.09846	0.00994	0.0320	1.260	2.0867
2000/07/03	21:09:56	18346	9.8027	-84.6335	42.31	13.10	16.4700	7.24436	0.10640	0.00843	0.0394	2.930	2.7001
2000/07/03	21:09:57	103	9.7648	-84.6864	40.00	13.13	17.4300	9.01571	0.33780	0.00890	0.0452	-999.0	2.7201
2000/07/04	06:58:42	2175	9.6068	-85.0550	15.44	11.77	8.5480	0.10139	0.09100	0.01613	0.0587	1.200	1.8134
2000/07/05	07:05:07	109	10.1258	-85.7419	26.00	14.57	5.5100	3.42768	0.08642	0.00407	0.0096	-999.0	3.6801
2000/07/05	07:05:08	18084	10.1426	-85.7125	23.31	14.56	5.3810	3.10456	0.08975	0.00352	0.0085	3.510	3.6734
2000/07/05	09:27:02	2187	9.5481	-84.9103	15.28	12.12	11.1000	0.40364	0.19160	0.01283	0.0459	2.150	2.0467
2000/07/05	09:47:19	17965	10.1455	-85.7110	23.72	11.93	15.7700	0.84333	0.11140	0.00903	0.0394	1.480	1.9201
2000/07/06	04:50:21	113	9.8846	-84.6048	50.00	13.41	16.9500	13.33520	0.11370	0.00716	0.0332	-999.0	2.9067
2000/07/06	16:51:34	17970	9.9619	-85.5282	26.77	12.68	13.5300	1.93642	0.15580	0.00696	0.0246	1.800	2.4201
2000/07/07	03:01:08	17976	9.9033	-85.3691	19.14	13.03	6.1650	0.33343	0.24060	0.00450	0.0149	2.120	2.6534
2000/07/07	03:25:02	2259	9.8963	-85.3754	17.96	12.48	10.7200	0.68391	0.11080	0.00700	0.0231	2.220	2.2867
2000/07/07	04:27:38	1916	9.8994	-85.3682	19.74	12.60	10.0000	0.67608	0.14800	0.00749	0.0241	1.920	2.3667
2000/07/07	04:30:32	17977	9.9035	-85.3746	19.27	12.20	10.9000	0.44361	0.09786	0.00810	0.0271	2.690	2.1001
2000/07/08	00:51:36	17984	9.8769	-85.4045	17.14	12.80	12.6500	1.93197	0.10300	0.00821	0.0286	2.620	2.5001
2000/07/08	01:25:24	1928	9.8833	-85.3988	15.82	12.46	13.7200	1.38676	0.11100	0.00900	0.0427	-999.0	2.2734
2000/07/10	11:12:41	17991	10.0259	-85.5524	15.14	12.35	10.3000	0.48529	0.13250	0.00761	0.0253	1.920	2.2001
2000/07/11	06:54:06	230	10.0059	-85.4575	8.00	12.21	14.7500	1.11429	0.09922	0.01015	0.0426	-999.0	2.1067
2000/07/12	02:19:11	234	10.2059	-85.6200	12.00	12.52	13.2500	1.37721	0.12280	0.00736	0.0280	-999.0	2.3134
2000/07/12	19:50:08	2366	9.9459	-85.6575	19.38	13.40	9.6330	2.43220	0.10610	0.00568	0.0162	2.560	2.9001
2000/07/13	05:00:07	2373	9.9603	-85.6599	16.96	12.57	10.0600	0.65766	0.12580	0.00696	0.0223	2.580	2.3467
2000/07/16	12:56:52	18135	10.2140	-85.8234	21.85	13.14	10.2600	1.85780	0.10710	0.00574	0.0176	2.480	2.7267
2000/07/16	12:56:53	252	10.2058	-85.7826	18.00	13.13	9.7280	1.55955	0.10430	0.00597	0.0176	-999.0	2.7201

Date	Time	Evid	Lat	Lon	Depth (km)	log M_0 (Nm)	ω_{cS} (Hz)	σ_a (MPa)	err σ_a	err M_0	err ω_{cS}	M_L	M_0
2000/07/16	20:14:06	18137	10.2451	-85.4462	39.67	12.49	13.8900	1.49968	0.10380	0.00748	0.0292	1.630	2.2934
2000/07/19	11:10:53	267	10.2458	-85.7826	30.00	13.58	8.0460	1.93642	0.08878	0.00511	0.0133	-999.0	3.0201
2000/07/19	11:10:54	18575	10.2480	-85.7684	25.87	13.57	7.8050	1.72982	0.09239	0.00453	0.0117	2.640	3.0134
2000/07/20	08:58:11	18149	10.1912	-85.7865	21.54	13.49	4.7590	0.34119	0.10140	0.00344	0.0101	2.270	2.9601
2000/07/20	08:58:12	270	10.2058	-85.7419	20.00	13.47	4.8930	0.36058	0.10480	0.00388	0.0119	-999.0	2.9467
2000/07/20	12:27:22	272	10.1658	-85.7825	26.00	13.01	9.5800	1.21619	0.10030	0.00675	0.0218	-999.0	2.6401
2000/07/20	12:27:23	18150	10.1909	-85.7807	22.99	12.99	9.3430	1.08643	0.09101	0.00578	0.0175	2.230	2.6267
2000/07/23	11:44:55	731	10.3880	-85.6212	46.75	12.93	15.4300	4.41570	0.09589	0.00684	0.0277	2.140	2.5867
2000/07/23	19:55:44	784	9.5659	-85.4576	30.00	13.20	8.5710	1.21060	0.13420	0.00672	0.0216	2.620	2.7667
2000/07/24	04:42:21	841	9.5960	-84.7850	16.73	13.61	6.8530	1.26183	0.12020	0.00524	0.0149	2.820	3.0401
2000/07/24	13:36:54	888	10.4292	-85.9394	28.63	13.32	8.5050	1.45211	0.11400	0.00682	0.0199	2.600	2.8467
2000/07/27	10:48:18	1130	10.3297	-85.8910	26.82	12.83	12.6700	2.05589	0.10850	0.00709	0.0253	2.020	2.5201
2000/08/10	12:06:32	18155	10.1845	-85.7865	23.00	13.46	6.9090	0.98401	0.10010	0.00447	0.0120	2.560	2.9401
2000/08/11	21:19:44	1555	10.0543	-85.5061	32.40	13.41	12.8600	5.88844	0.10920	0.00684	0.0231	2.670	2.9067
2000/11/25	05:37:05	18764	9.8290	-85.1315	25.45	12.01	16.7500	1.15878	0.19690	0.01562	0.0629	1.740	1.9734
2000/11/25	11:14:43	18768	9.9913	-85.6656	19.42	11.82	15.2700	0.63533	0.17300	0.01218	0.0555	1.520	1.8467
2000/11/25	17:18:36	18783	9.8582	-85.3163	18.42	12.23	16.6500	1.67109	0.14570	0.01157	0.0555	2.290	2.1201
2000/11/26	02:01:52	18807	9.9436	-85.2586	27.24	13.03	13.0000	3.15500	0.11930	0.00608	0.0206	2.310	2.6534
2000/11/26	19:27:12	18864	9.8527	-85.6775	17.01	12.56	11.5100	0.97051	0.18620	0.01045	0.0353	2.020	2.3401
2000/11/26	19:29:01	18865	9.8498	-85.6756	18.61	13.22	7.4460	0.81846	0.13820	0.00522	0.0140	2.370	2.7801
2000/11/26	22:39:57	18883	9.7062	-85.0254	16.66	12.22	9.4420	0.29785	0.17630	0.01382	0.0534	1.840	2.1134
2000/11/27	05:24:14	18898	9.5819	-84.7497	14.67	13.45	3.9250	0.17742	0.11570	0.00376	0.0108	2.580	2.9334
2000/11/27	08:46:24	20387	9.9092	-85.4159	20.11	11.45	10.6200	0.11092	0.18390	0.01316	0.0443	2.000	1.6001
2000/11/27	09:42:26	18903	10.0818	-85.4753	32.96	12.35	16.7800	2.07970	0.13190	0.00792	0.0341	1.830	2.2001
2000/11/27	14:37:26	18914	9.8603	-85.2990	19.07	12.60	12.0400	1.17761	0.12590	0.00747	0.0272	1.910	2.3667
2000/11/28	06:02:40	18962	9.9476	-85.6729	18.30	12.45	13.4600	1.28233	0.12810	0.00730	0.0262	2.240	2.2667
2000/11/29	10:00:06	19069	9.6974	-84.9478	24.89	12.09	11.2000	0.39719	0.13170	0.01004	0.0357	2.670	2.0267
2000/11/29	16:32:34	19084	9.6058	-84.8483	16.13	12.63	8.3920	0.42658	0.12050	0.01127	0.0416	2.780	2.3867
2000/11/30	05:08:39	19135	10.0481	-85.6093	16.29	12.17	12.5100	0.63387	0.19370	0.00830	0.0280	1.660	2.0801
2000/12/01	20:54:48	19391	10.2118	-85.7752	24.84	12.24	16.6100	1.67109	0.14250	0.01045	0.0479	2.040	2.1267
2000/12/02	08:55:59	19421	9.6166	-85.2014	10.05	12.07	7.1650	0.09954	0.14340	0.00753	0.0262	2.540	2.0134
2000/12/03	13:34:20	19497	9.9617	-85.6421	19.25	11.82	11.9100	0.29785	0.13830	0.01739	0.0566	1.830	1.8467
2000/12/05	00:10:28	19594	9.5649	-85.0297	12.87	12.44	8.9060	0.36308	0.15970	0.01124	0.0388	2.270	2.2601
2000/12/05	05:09:04	19603	10.2325	-85.8375	21.09	12.04	10.1100	0.26730	0.14210	0.01701	0.0645	2.340	1.9934
2000/12/07	04:24:11	19770	9.8610	-85.2924	19.29	12.73	12.5500	1.68267	0.14530	0.00677	0.0226	2.520	2.4534

Date	Time	Evid	Lat	Lon	Depth (km)	log M_0 (Nm)	ω_{cS} (Hz)	σ_a (MPa)	err σ_a	err M_0	err ω_{cS}	M_L	M_0
2000/12/07	04:43:13	19771	9.8633	-85.2894	18.57	11.96	14.3300	0.65917	0.17770	0.01020	0.0410	2.530	1.9401
2000/12/07	10:52:35	22000	10.2160	-85.8087	23.62	11.61	8.7360	0.08241	0.13100	0.01517	0.0534	2.010	1.7067
2000/12/10	17:27:24	20065	9.9214	-85.4235	19.97	12.80	12.8000	2.02302	0.16950	0.00809	0.0290	2.220	2.5001
2000/12/11	22:24:20	20202	9.5971	-85.2501	15.76	12.96	8.1340	0.68391	0.19570	0.00775	0.0232	2.640	2.6067
2000/12/14	03:57:56	20435	9.6411	-85.1829	20.74	11.88	8.7320	0.13002	0.26650	0.01483	0.0480	1.910	1.8867
2000/12/14	18:42:34	20468	10.1989	-85.7266	25.88	12.76	11.2100	1.26474	0.18400	0.01764	0.0720	1.960	2.4734
2000/12/14	21:52:34	20502	9.8714	-84.7536	39.02	13.09	16.5900	7.24436	0.09674	0.00864	0.0422	2.800	2.6934
2000/12/16	19:14:21	20597	9.9181	-85.4336	19.09	12.47	13.8800	1.44877	0.14590	0.00920	0.0364	2.410	2.2801
2000/12/17	10:44:12	20621	10.1181	-85.4420	33.35	12.53	14.4600	1.82390	0.13800	0.00685	0.0254	2.080	2.3201
2000/12/17	11:58:26	20624	9.5625	-84.8706	13.66	12.59	9.2510	0.52723	0.11380	0.00933	0.0321	2.630	2.3601
2000/12/19	00:16:14	20799	9.7176	-85.0193	19.76	11.95	10.6800	0.26792	0.17040	0.01522	0.0546	2.230	1.9334
2000/12/19	02:18:12	20802	9.5655	-84.8607	15.29	12.30	10.1100	0.41591	0.17500	0.01146	0.0446	2.770	2.1667
2000/12/19	15:52:08	20820	9.7335	-84.9853	22.61	12.41	8.2130	0.27227	0.14000	0.01093	0.0387	2.450	2.2401
2000/12/22	05:05:49	21060	10.1585	-85.9472	25.07	11.95	10.0500	0.22542	0.12820	0.01217	0.0431	2.520	1.9334
2000/12/22	12:25:20	21070	10.2613	-85.8586	22.37	12.64	11.6800	1.16145	0.11650	0.00760	0.0258	2.240	2.3934
2000/12/22	12:45:56	21071	10.1897	-85.6626	17.29	12.56	11.4900	0.95940	0.14220	0.00710	0.0232	1.710	2.3401
2000/12/23	02:23:55	21139	9.6485	-85.1859	18.46	12.22	10.3400	0.38994	0.25040	0.01169	0.0376	2.580	2.1134
2000/12/24	12:38:40	21233	9.8465	-85.2224	16.92	12.67	7.4760	0.32359	0.16370	0.00632	0.0195	2.350	2.4134
2000/12/24	21:00:10	21279	9.6455	-85.1639	15.45	12.28	12.9800	0.86099	0.15210	0.01634	0.0612	2.280	2.1534
2000/12/25	00:57:48	21288	10.1943	-85.4066	38.73	12.79	17.1600	4.78630	0.13130	0.00688	0.0299	2.070	2.4934
2000/12/27	05:29:42	21446	9.8390	-84.6621	49.57	13.16	14.0700	5.01187	0.12290	0.00713	0.0275	2.660	2.7401
2000/12/27	07:21:28	24421	9.9608	-85.6421	19.36	11.54	10.8500	0.14061	0.17740	0.01323	0.0522	2.190	1.6601
2000/12/27	09:28:55	21454	9.9008	-85.3552	19.59	13.00	9.6960	1.24738	0.11420	0.00585	0.0170	2.120	2.6334
2000/12/28	03:04:14	21522	9.8549	-85.2354	18.14	12.25	11.7600	0.60395	0.15360	0.00905	0.0323	2.330	2.1334
2001/01/01	22:53:53	22303	10.6752	-85.9118	46.10	12.96	13.3800	3.06196	0.13260	0.00892	0.0422	2.650	2.6067
2001/01/05	15:33:38	22575	10.0132	-85.6627	18.86	12.53	11.5400	0.92257	0.15410	0.00979	0.0360	1.700	2.3201
2001/01/08	09:06:05	23014	9.8227	-85.2579	21.65	12.42	9.9250	0.48641	0.10570	0.00669	0.0210	2.320	2.2467
2001/01/08	10:29:49	23018	9.8974	-85.5215	16.38	13.92	4.3550	0.54954	0.10960	0.00315	0.0079	3.100	3.2467
2001/01/08	14:57:26	23028	9.9001	-85.5127	14.69	12.27	11.2500	0.54828	0.23240	0.01112	0.0391	2.000	2.1467
2001/01/09	12:24:05	23134	9.5407	-84.5936	23.65	15.09	3.6260	2.39332	0.13800	0.00300	0.0068	4.210	4.0267
2001/01/09	21:58:30	24624	10.1330	-85.4302	34.04	12.63	1.9630	0.00547	0.46590	0.00439	-0.0507	2.230	2.3867
2001/01/11	04:40:39	24648	9.5793	-84.7057	23.34	12.28	11.7800	0.64417	0.15310	0.01300	0.0425	2.880	2.1534
2001/01/13	07:54:14	23716	9.6222	-85.1938	19.56	12.35	8.9010	0.31189	0.26290	0.00962	0.0298	2.360	2.2001
2001/01/13	17:16:22	23735	9.9123	-85.4031	18.99	12.51	12.9200	1.24451	0.12520	0.00924	0.0359	1.950	2.3067
2001/01/14	02:00:01	23890	9.6223	-84.7650	23.71	12.17	14.1300	0.91833	0.62700	0.02059	0.0828	2.430	2.0801

Date	Time	Evid	Lat	Lon	Depth (km)	log M_0 (Nm)	ω_{cS} (Hz)	σ_a (MPa)	err σ_a	err M_0	err ω_{cS}	M_L	M_0
2001/01/14	08:02:18	23962	9.9298	-85.3715	18.14	11.78	11.8000	0.27040	0.12450	0.01875	0.0596	2.100	1.8201
2001/01/18	02:06:56	25277	9.9027	-85.4934	19.62	12.18	11.9800	0.56234	0.15750	0.00940	0.0335	1.880	2.0867
2001/01/18	02:16:15	25279	9.9256	-85.4963	16.07	11.99	13.9800	0.64269	0.15300	0.01044	0.0427	2.040	1.9601
2001/01/18	07:09:08	25297	9.9567	-85.4683	19.81	11.83	17.3300	0.93972	0.20030	0.01291	0.0637	1.570	1.8534
2001/01/19	01:46:27	25438	9.8869	-85.3801	20.05	12.85	13.5200	2.59418	0.10380	0.00638	0.0230	2.840	2.5334
2001/01/19	04:31:20	25457	9.9669	-85.3356	22.65	12.09	15.6900	1.08643	0.21940	0.00921	0.0391	2.090	2.0267
2001/01/21	02:55:00	25715	9.9233	-85.3175	22.37	12.08	16.8600	1.32130	0.12510	0.01068	0.0522	2.370	2.0201
2001/01/22	05:03:02	25897	9.6255	-85.0784	21.87	14.43	4.4810	1.44212	0.11640	0.00340	0.0080	3.460	3.5867
2001/01/22	07:16:42	25905	9.6545	-85.1797	15.93	12.21	10.1400	0.36141	0.15350	0.00933	0.0288	2.180	2.1067
2001/01/23	00:06:42	26072	9.6150	-85.0111	16.31	12.20	10.8800	0.43954	0.16840	0.01273	0.0436	2.220	2.1001
2001/01/23	01:07:28	27387	10.2174	-85.8179	25.44	11.69	10.9400	0.18493	0.49530	0.01962	0.0600	1.640	1.7601
2001/01/24	07:01:15	26301	9.9363	-85.7603	17.54	11.85	12.9300	0.40179	0.18900	0.01465	0.0519	2.190	1.8667
2001/01/24	10:27:53	26319	9.9782	-85.6476	20.90	11.93	9.6000	0.19011	0.14000	0.01141	0.0385	2.330	1.9201
2001/01/25	14:59:24	26534	9.9542	-85.6741	18.95	14.02	6.1060	1.79887	0.12340	0.00404	0.0099	3.160	3.3134
2001/01/26	12:15:12	26673	10.4200	-85.9209	33.41	13.45	10.5200	3.44350	0.11320	0.00617	0.0184	2.570	2.9334
2001/01/26	18:52:20	26714	10.2182	-85.8180	22.64	12.44	8.5340	0.31989	0.20730	0.01388	0.0588	2.100	2.2601
2001/01/27	17:59:06	26828	9.5902	-84.8905	16.30	12.89	9.5700	0.98628	0.12580	0.01022	0.0344	2.710	2.5601
2001/01/28	05:10:18	26892	9.5293	-84.6200	17.36	12.23	10.3200	0.39719	0.40960	0.01382	0.0555	2.840	2.1201
2001/01/30	23:56:29	27181	9.6352	-85.1995	18.56	13.83	6.3660	1.46218	0.12110	0.00453	0.0111	3.000	3.1867
2001/01/31	03:03:10	27533	10.0892	-85.4765	33.13	11.79	16.8300	0.79616	0.17350	0.01413	0.0598	2.120	1.8267
2001/01/31	03:14:55	27534	9.7520	-85.0280	27.57	12.87	11.0400	1.45546	0.11990	0.00709	0.0226	2.530	2.5467
2001/01/31	03:52:50	27536	9.6696	-85.1924	20.57	12.38	10.0500	0.47315	0.38620	0.00862	0.0264	2.190	2.2201
2001/01/31	04:00:00	27538	9.6685	-85.1850	20.08	12.10	10.8800	0.36728	0.17030	0.00988	0.0346	2.270	2.0334
2001/01/31	04:43:20	27541	9.6198	-84.8913	17.70	13.16	5.9490	0.37411	0.11100	0.00538	0.0155	2.680	2.7401
2001/01/31	21:25:59	29375	9.9757	-85.5249	15.94	12.61	7.8170	0.32885	0.14600	0.00916	0.0309	2.100	2.3734
2001/02/01	10:36:50	27674	9.9647	-85.5311	15.82	12.05	13.3200	0.62230	0.15690	0.00986	0.0390	1.510	2.0001
2001/02/02	07:11:54	29401	9.8826	-85.2779	23.39	11.86	12.6500	0.38459	0.12530	0.01434	0.0520	1.770	1.8734
2001/02/02	12:35:13	27783	9.8554	-85.6423	17.29	12.19	7.2620	0.12882	0.18460	0.01544	0.0558	2.200	2.0934
2001/02/06	07:40:06	28228	9.9043	-85.2282	17.54	11.88	9.4230	0.16293	0.32880	0.01469	0.0468	2.160	1.8867
2001/02/06	12:05:30	28237	10.2021	-85.7348	24.37	12.10	10.2700	0.30974	0.14980	0.01266	0.0420	1.910	2.0334
2001/02/06	15:34:52	28244	9.6229	-84.6323	23.71	12.96	8.0990	0.67608	0.11250	0.01132	0.0391	3.070	2.6067
2001/02/06	21:57:23	28286	9.9951	-85.6558	17.41	12.36	10.4800	0.51523	0.13340	0.01077	0.0365	1.620	2.2067
2001/02/08	04:53:47	28382	10.1009	-85.2982	40.45	13.78	8.8520	3.63078	0.11050	0.00498	0.0132	2.750	3.1534
2001/02/08	21:57:03	28490	9.6071	-84.8659	19.19	13.67	8.2240	2.38781	0.14540	0.00596	0.0175	2.840	3.0801
2001/02/09	08:09:10	29475	9.7326	-84.8900	20.75	11.61	5.3700	0.01901	0.18180	0.01672	0.0603	1.890	1.7067

Date	Time	Evid	Lat	Lon	Depth (km)	log M_0 (Nm)	ω_{cS} (Hz)	σ_a (MPa)	err σ_a	err M_0	err ω_{cS}	M_L	M_0
2001/02/10	01:38:34	28599	9.8877	-85.3657	19.17	12.94	7.1230	0.44259	0.12110	0.00564	0.0166	2.080	2.5934
2001/02/12	14:35:38	28939	10.0090	-85.4563	32.34	13.84	7.2630	2.21309	0.08835	0.00464	0.0119	2.930	3.1934
2001/02/14	00:07:45	29517	9.6363	-84.9142	22.96	12.18	8.4680	0.19953	0.42360	0.01891	0.0644	1.950	2.0867
2001/02/14	07:57:17	29197	9.6807	-85.2478	18.72	11.92	12.9300	0.45290	0.12500	0.01537	0.0514	1.900	1.9134
2001/02/16	06:55:17	29719	10.6675	-85.9819	37.12	14.87	4.2080	2.55270	0.12460	0.00323	0.0075	4.000	3.8801
2001/02/16	18:56:47	29779	10.2429	-85.7779	26.34	12.78	11.1100	1.26765	0.13780	0.00795	0.0256	2.120	2.4867
2001/02/17	01:17:06	29854	9.9141	-85.4184	20.03	11.95	14.3300	0.65013	0.13140	0.01848	0.0701	1.660	1.9334
2001/02/17	08:59:04	29886	9.9045	-85.3567	20.57	11.51	13.4900	0.25293	0.20170	0.01945	0.0701	1.590	1.6401
2001/02/17	18:42:10	29951	9.9694	-85.4082	19.83	12.61	12.7400	1.42561	0.14640	0.00895	0.0338	1.870	2.3734
2001/02/19	12:44:24	30432	9.5840	-85.1700	16.23	12.58	8.6150	0.42364	0.32650	0.01041	0.0337	1.970	2.3534
2001/02/20	00:51:21	30664	9.8746	-85.2853	16.34	12.39	7.2900	0.18239	0.34310	0.00914	0.0314	2.060	2.2267
2001/02/20	04:44:49	30682	10.2321	-85.6724	32.16	11.89	11.1400	0.27353	0.23210	0.01533	0.0500	1.910	1.8934
2001/02/21	03:11:20	31757	9.6783	-85.1735	19.40	11.89	11.4000	0.29648	0.16990	0.01960	0.0685	1.680	1.8934
2001/02/22	09:44:27	31770	9.6579	-85.1317	19.26	11.88	10.7800	0.24547	0.41880	0.01390	0.0466	1.840	1.8867
2001/02/23	01:21:48	31773	10.2763	-85.8539	23.13	11.99	10.6400	0.28445	0.11860	0.01738	0.0608	1.580	1.9601
2001/02/24	07:31:43	31789	9.7419	-85.0267	19.90	11.83	10.0400	0.18365	0.25350	0.01237	0.0403	2.100	1.8534
2001/02/24	09:15:20	31792	9.9014	-85.3136	24.10	11.63	13.4000	0.30549	0.07685	0.02124	0.1026	2.820	1.7201
2001/03/02	06:15:50	31876	10.2821	-85.8625	24.06	13.33	7.7100	1.09901	0.13810	0.00487	0.0129	2.570	2.8534
2001/03/02	11:26:16	31885	9.5965	-84.7251	23.26	13.18	7.9770	0.94624	0.15250	0.00672	0.0200	2.530	2.7534
2001/03/03	09:50:21	31919	9.9748	-85.3235	21.88	12.22	13.1800	0.81470	0.12430	0.00823	0.0314	2.030	2.1134
2001/03/04	08:42:19	31979	10.2104	-85.7712	21.06	12.83	9.7720	0.95061	0.12770	0.00588	0.0168	2.290	2.5201
2001/03/04	21:49:29	32021	10.2208	-85.8077	21.90	12.42	14.5200	1.51705	0.15940	0.01072	0.0442	1.800	2.2467
2001/03/05	08:28:20	32041	10.3432	-85.8982	24.38	13.51	7.4320	1.34276	0.11060	0.00469	0.0119	2.610	2.9734
2001/03/09	06:53:58	32732	9.9243	-85.3711	21.93	11.96	8.9700	0.16293	0.13120	0.01348	-0.1366	3.060	1.9401
2001/03/09	09:17:04	32733	9.6299	-85.2215	17.97	11.76	13.1400	0.36308	0.29500	0.01914	0.0712	2.300	1.8067
2001/03/09	10:32:59	32476	10.1769	-85.6114	25.85	11.91	13.5700	0.51404	0.15100	0.01003	0.0385	1.800	1.9067
2001/03/09	14:21:07	32484	9.6437	-85.0792	15.07	13.07	9.1540	1.16681	0.12730	0.00711	0.0217	2.350	2.6801
2001/03/10	02:19:34	32541	9.9939	-85.6237	29.02	11.95	15.6800	0.84918	0.21070	0.01247	0.0506	1.870	1.9334
2001/03/20	18:33:15	33448	10.0850	-85.6295	20.26	12.87	10.1200	1.12980	0.14930	0.00703	0.0223	1.990	2.5467
2001/03/21	15:28:04	33545	9.6600	-84.7234	35.27	13.83	13.3200	13.33520	0.10000	0.00539	0.0207	3.060	3.1867
2001/03/21	21:06:00	33630	10.5240	-85.6257	49.39	13.88	7.9480	3.09742	0.12030	0.00527	0.0140	2.650	3.2201
2001/03/21	23:30:44	34328	9.5975	-84.9338	18.06	12.39	10.0200	0.47534	0.24670	0.01985	0.0630	2.200	2.2267
2001/03/22	01:23:58	33653	9.9933	-85.5376	17.84	11.99	8.8850	0.16634	0.14620	0.01201	0.0450	1.960	1.9601
2001/03/23	04:38:59	33829	9.6292	-84.8766	18.23	12.97	7.3970	0.51761	0.12740	0.00715	0.0211	2.560	2.6134
2001/03/23	12:44:36	33864	10.0980	-85.4766	33.32	12.55	16.3400	2.71019	0.14370	0.00860	0.0369	1.740	2.3334

Date	Time	Evid	Lat	Lon	Depth (km)	log M_0 (Nm)	ω_{cS} (Hz)	σ_a (MPa)	err σ_a	err M_0	err ω_{cS}	M_L	M_0
2001/03/27	03:08:26	34391	9.5929	-84.7634	23.10	12.53	8.4010	0.36058	0.12250	0.01159	0.0333	2.440	2.3201
2001/03/27	09:58:26	35186	10.1975	-85.7913	23.74	12.10	11.3800	0.42267	0.13570	0.01163	0.0437	1.630	2.0334
2001/03/28	05:11:53	34498	9.5263	-84.7164	17.12	13.89	5.0740	0.83176	0.10210	0.00428	0.0102	2.860	3.2267

APPENDIX B

Appendix B

All of the scripts used to create narrow-band frequency envelopes, obtain coda amplitude measurements, and calibrate the measured amplitudes are described in this appendix. The detailed description of programs used in the processing follows the script tree-structure list.

This appendix is separated into three sections: narrow-band envelopes processing, picking routines used to get the coda start and end times, and codes that calibrate the coda amplitude. The narrow-band envelope processing section containing scripts for creating the narrow-band frequency envelopes. The picking routines consist of SAC macros used to pick and store the coda amplitude. The coda calibration section in this appendix contains scripts used for coda amplitude corrections, seismic moment fit, and apparent stress calculation.

B.1 Processing: Narrow-band frequency envelopes

In order to create the narrow-band frequency envelopes, I need the raw waveform data and several database files containing the earthquake and instrument information. The earthquake waveform data are in SAC format, separated into directories named after the event's origin day and identification number (evid). The database files that I need are shown in Table B.1 with a

short description.

Table B.1: These are database files needed to create narrow-band frequency envelopes from SAC earthquake data.

File name	File contents
NICOYA.event	Event identification number, origin number, author, -1, epoch time
NICOYA.origin	Event origin information: latitude, longitude, depth, origin time, event ID, origin ID, year-day, etc.
NICOYA.arrival	P and S wave arrival times: station name, arrival time, event ID, year-day, 01, 7, channel, arrival description, etc.
NICOYA.assoc	P and S arrival times based on wfdisc ID
NICOYA.wfdisc	Database file information tied all together
NICOYA.sensor	Instrument information
NICOYA.instrument	Instrument information

I used numerous scripts tied together in a main shell program called envelope.nmt.sh to create the envelope bands. This program needs four input information: station name, station channel, unit (I used velocity), and a flag to create new envelopes or replace the old ones. The hierarchy of the code tree structure is shown below. Right-offset programs are being called by the programs above and offset to the left of them.

B.1.1 Narrow-band envelopes code structure

- Envelopes/envelope.nmt.sh
  - Envelopes/prefor.pl
  - Envelopes/wfcor.pl
  - Envelopes/nmtpicks.pl
  - Calibration/Codes/dist.f

. Calibration/Codes/distaz.f

– Envelopes/dtmatch.f

– Envelopes/Codes/envelope.f

. Envelopes/Codes/band_setup.f

. Envelopes/Codes/ljust.f

. Envelopes/Codes/deconband.f

. Envelopes/Codes/sort.f

. Envelopes/Codes/wf_.c

. Envelopes/Codes/rmean_.c

. Envelopes/Codes/sactaper.f

. Envelopes/Codes/tovel.f

- Envelopes/Codes/sacndctransfer_.c

. Envelopes/Codes/scaled_response.c

- Envelopes/Codes/unscaled_response.c

- Envelopes/Codes/vel.f

. Envelopes/Codes/getran.f

- Envelopes/Codes/taper.f (function)

- Envelopes/Codes/dcpft_.c

. Envelopes/Codes/sacenvelope.f

- Envelopes/Codes/firtrn.f

. Envelopes/Codes/zero.f

. Envelopes/Codes/overlp.f

- Envelopes/Codes/zero.f
- Envelopes/Codes/copy.f
- Envelopes/Codes/fft.f
. Envelopes/Codes/zshft.f
- Envelopes/Codes/zero.f
. Envelopes/Codes/rotate.f
. Envelopes/Codes/sacxapiir.f
- Envelopes/Codes/design.f
. Envelopes/Codes/buroots.f
. Envelopes/Codes/warp.f
. Envelopes/Codes/lptbp.f
. Envelopes/Codes/bilin2.f
- Envelopes/Codes/apply.f
. Envelopes/Codes/sacinterpolate.f
- Envelopes/Codes/wigint.f
. Envelopes/Codes/sacsmooth.f

B.1.2 Narrow-band envelopes code description

Envelopes/envelope.nmt.sh

This script ties together every other program and subroutine needed to create pre-defined narrowband frequency envelopes out of earthquake waveforms. It needs the raw waveform data, database information (e.g. earthquake origin files, arrival info, instrument info, etc.), and deconvolution parameters. I put two stars to scripts that are called by this program.

The input parameters are *sta* (station), *comp* (component), *unit* (I use velocity), and *rflag*. The last one refers to whether I want to create new envelopes (set to replace) or not (set to update). For a number of stations, the script runs using **run_nmt.sh** file. This file invokes envelope.nmt.sh based on station-component pair.

I use only data within a latitude-longitude defined area (9.5N, 11.5N, -86W, -84.5W). There are several paths that need to be set, for example, the data input/output directories, the results directory, and all the needed database files.

The script calls in subroutine **prefor.pl** to search for the preferred origin ID per given event from the *NICOYA.event* and *NICOYA.origin* files. The preference is based on location output parameters. Next the script **wfcor.pl** is called to pull out additional earthquake and instrument fields needed for further processing. The P and S arrival information is obtained using the subroutine **nmtpicks.pl**. The information from the 3 scripts is stored together and I check for duplicate event IDs before continuing with processing.

The obtained information on earthquake event ID is matched to *NICOYA.wfdisc* files based on overlap of start and end times (**dtmatch.f**, overlap must be larger than 0). After I have match between the preferred origin and the wfdisc files, I calculate the distance between the source and receiver, the azimuth, and the back azimuth using **dist.f**. I added 0.01 km to all distance measurements to avoid zero station-receiver distance. I eliminate all events within 60 seconds of each other, and those without two horizontal components. I prepare the event directories and files, and then run the **envelope.f** script

that creates the narrowband envelopes.

Envelopes/prefor.pl

This script searches for preferred origin IDs based on the database *NICOYA.event* and *NICOYA.origin* files. It also assigns magnitude values, mb, for input magnitudes equal to ms, mb, or ml. If the input file does not contain either of the three magnitude types, it'll assign magnitude -999.0. The script uses a subroutine (explained at the end of the script) called epoch2ymdhms that converts the input epoch time into integer values of year, month, day of the month, hour, and minute. It returns the second as integer and decimal value, which are added together. Output is stored in *prefor.sort*.

Envelopes/wfcor.pl

Its function is to pull out wfdisc and instrument fields needed for processing. The inputs are: station, channel, wfdisc file, sensor file, and instrument file. Output is stored in *wfcor.$stn.$ncomp.out* in current directory.

Envelopes/nmtpicks.pl

The code pulls out P and S arrival times based on event ID from *prefor.sort*. Its inputs are: *sta*, *NICOYA.event*, *NICOYA.arrival* and *NICOYA.assoc*. Its outputs are event ID, wave phase, author and time. Output is stored in *nmtpicks.$stn.out*.

Calibration/Codes/dist.f

This is sort of a middle man between **envelope.nmt.sh** and **distaz.f**. It reads in data for event latitude and longitude, and station latitude and longitude. These numbers are the input for **distaz.f**. Output is read directly

by **distaz.f**.

Calibration_/Codes/distaz.f

Distaz.f computes the distance, azimuth and back azimuth between given locations. It needs the read-in data from **dist.f** to calculate the epicentral distance in km, azimuth and back azimuth in degrees, and the great circle arc length. It also assigns an error value to a variable called nerr. Calculations are based on the reference spheroid of 1968. They are defined by major radius (6378.16 km) and flattening of Earth. Convert here between geographic to geocentric coordinate system, which requires latitude correction using flattening. Distance calculations are done using Rudoe's formula that gives distances accuracy on cm scale. However, given the location errors of the earthquake locations, this formula will never be used to its full potential. Output variables are event ID, distance, azimuth, back azimuth, and error. Output stored in *temp2.$stn.$comp.out*.

Envelopes/dtmatch.f

This script matches the event IDs and origin times from *prefor.sort* to event IDs, start time and end time values given in the *NICOYA.wfdisc file*. The outputs are event IDs from *prefor.sort* and *NICOYA.wfdisc*, and the amount of overlap. It stores any overlap larger than zero. Output stored in *dtmatch.$stn.$comp.out*.

Envelopes/Codes/envelope.f

This is a program that creates narrowband frequency envelopes from the waveform data. Currently I am using only horizontal components. The initial condition with these is that I have to have two files (*narmin*=2) to

stack. I do not use files that don't have both, east and north, components. This script ties together numerous subroutines that are described below.

At first I use **band_setup.f** to assign frequency bands and parameters, such as taper and interpolation widths. The Lg and S peak arrival group velocities are assigned next (*vlg*,*vs0*,*vs1*, and *vs2*). The data files must start and end within 20% (*tfrac*)of start/end time, otherwise they'll be not used. The input strings (e.g. *stn*, *comp*, etc.) are left-justified using **ljust.f**. I reassign tapering width (5 seconds) for frequency bands 0.5_0.7 Hz and higher. It is calculated from the origin time, the maximum distance (3,000 km), and minimum group velocity (1.0 km/s). After this I read in the data and set deconvolution band limits (**deconband.f**).

Next I calculate the distance between source and receiver, the azimuth, and the back azimuth (**distaz.f**). The noise window (*wnoise*) is set to 600, the *vg1*=8.0, *vg2*=0.5, and minimum window time (*wtmin*) = 480. I calculate the best start and stop times based on the four parameters above. I'm using subroutine **sort.f** to sort strings of data in order to obtain median end time and start time relative to origin time. Following this, I do quality control: the data must be larger than *4*(min hwide)+2*ttaper2+2*dlmax*, and it has to contain Lg or Sn peaks (check at 1Hz). There are also limits on the total file length (2^{19} samples) for coming up FFT.

I use **wf_.c** to check the data type and read in data. Then the mean (**rmean_.c**) is removed from the signal. Initially, I taper in the time domain using sactaper.f. The data is transformed into velocity signal, and the instrument response is removed using **tovel.f** subroutine. The individual frequency

bands are filtered using IIR (Butterworth, 4 pole, 2 pass) filtering method (**sacxapiir.f**). From the velocity signal, I create narrow-band frequency envelopes using the **sacenvelope.f** subroutine. The envelopes are aligned and rotated into R and T components. The filtered velocity bands are interpolated to 1 second (**sacinterpolate.f**) and smoothed (**sacsmooth.f**). If the interpolation interval and sampling rate difference is larger than 1, the bands undergo another interpolation based on band dependent sampling rate (using **sacinterpolate.f** again). After the last interpolation, the R and T components are stacked and averaged.

Several SAC functions are used to assign header values. The picks are modified from the original version (due to short distances), so that instead of using Pg and Lg, I replace them with P and S.

Envelopes/Codes/band_setup.f

Here the envelope band width in terms of frequency is set. The total number of bands must be assigned (*nband*), otherwise it'll cause problems later on. Each frequency band has assigned the low limit (*f1*) and the high limit (*f2*); the width of boxcar function (*hwide*), the interpolation interval (*delint*), the name of the band (*key*), and the number of characters in the name (*nkey*). The interpolation interval is related to the width of boxcar function in frequency bands 1.0-1.5 and 1.5-2.0. Output is read directly by **envelope.f**.

Envelopes/Codes/ljust.f

This script left-justifies the entries in its input in order to eliminate blank spaces. It is used on variables *sta*, *comp*, *evtype* (event type; e.g. IQUAKE = earthquake), source and output. I use it later to left justify data

input files and response input files. Output is read directly by **envelope.f**.

Envelopes/Codes/deconband.f

In this script I assign the deconvolution filter limits for the cosine taper (in frequency domain) and the taper length. The code reads in station, component, 1/sampling rate, and real frequency limits. It splits frequency limits of the data input based on sampling rate, because my instruments sampled at 20 and 40 Hz. Output is read directly by **envelope.f**.

Envelopes/Codes/sort.f

This code sorts the input values from low to high. It has been adopted from the Numerical Recipes book. It is used several times during the initial processing as well as the coda calibration step. Output is read directly by **envelope.f**.

Envelopes/Codes/wf_.c

Reads in variety of data types (except for seed format) and skips a header if it exists (foff). In my case the earthquake waveforms are in sac (Seismic Analysis Code) format. Thus, before running this script, the datatype is set to t4. Output is read directly by **envelope.f**.

Envelopes/Codes/rmean_.c This code is used to remove the mean from the earthquake signal. Its output is written back into the original data string. Output is read directly by **envelope.f**.

Envelopes/Codes/sactaper.f

The earthquake waveforms are tapered at the beginning of the signal and at the end to level off to zero at the margins. The taper length is set to 25

seconds (in **deconband.f**) for bands below 0.5 Hz; and to 5 seconds for bands above 0.5 Hz (in **envelope.nmt.sh**). The data is tapered using sine function on the number of samples. Output is written back into the data string.

Envelopes/Codes/tovel.f

The code is used to remove the instrument response from the signal and to convert the signal into velocity units for further coda work. The response type must be of NDC type. It checks initially for the logic of deconvolution limits, and if there is an error in their setup it will quit. It calls in several scripts. The first (**sacndctransfer_.c**) checks for errors due to response file type. Then the code calculates the magnitude of the imaginary and real parts of the response. In the next step, the real and imaginary parts of the response are converted into velocity in time domain (using **vel.f** and **getran.f**). The frequency limits are tapered using function **taper.f**, and the taper scale is applied to the frequency bands. The response is transformed into frequency domain (using **dcpft_.c**). Then the response is removed from the data in frequency domain. The output is the data transformed back into the time domain and stored in the original data array. Output is read directly by **envelope.f**.

Envelopes/Codes/sacndctransfer_.c

The input of this script is the complex instrument response string. It calls in **scaled_response.c** that does the actual response handling. **Sacndctransfer_.c** reports the final values and errors. Based on the error value (0 is ok, -1 is not good), it will pass data file through if it has response string associated with it. If the data does not have a response file, the data will be skipped and not processed. The output variables are *nerr* (error, should be

0), *xre* (real portion of instrument response), and *xim* (imaginary portion of instrument response). Output is read directly by **tovel.f**.

Envelopes/Codes/scaled_response.c The inputs here are the location of the instrument file response, the type of the instrument response (I use theoretical), the measure of instrument response (I use displacement), curve plot options (I use linear space), starting and ending frequency, number of requested frequency samples, and calibration factor (maps digital data to earth displacement, in nm/digital count units) and period (sec). The output is the instrument response in complex form. The response is scaled with respect to the amplitude measured at calibration period. It will return $err = 0$, if there are no errors. Output is read directly by **sacndctransfer_.c**.

Envelopes/Codes/unscaled_response.c

This one works similarly to **scaled_response.c**. It has the same input, but its general purpose is to return an error definition (different integer values) based on the Center of Seismic Studies error tables. The script gives error values to all output files that did not get err = 0 from **scaled_response.c** . Output is read directly by **scaled_response.c**.

Envelopes/Codes/vel.f

This is very short fortran script that calls in **getran.f**. Its output is deconvolved instrument response in velocity units. Output is read directly by **tovel.f**.

Envelopes/Codes/getran.f

In here, the instrument response is deconvolved to displacement and

then the displacements is converted to velocity. The output is the complex form of instrument response in velocity units. Output is read directly be **vel.f**.

Envelopes/Codes/taper.f (function)

This is a function to taper spectra using cosine taper method. The inputs are frequency in question and transition frequency (low and high). Depending on the magnitude of the lower and higher transition frequency, the function produces a low pass or a high pass tapering. The output is the tapered spectra based on frequency in question and deconvolution band limits set in **deconband.f**. Output is stored in a variable called *fac* (line 120 in **tovel.f**).

Envelopes/Codes/dcpft_.c

The input variables are: the real and imaginary parts of the data vector (data for me is the impulse response), number of elements (this is number of samples padded with zeroes to total length of samples equal to the maximum of the Fourier series samples), spacing in memory of data (I set mine to 1), and a sign of argument in transform exponential (-1 is the Fourier transform from time to frequency domain, 1 is the Inverse Fourier transform from frequency to time domain). The output is the input transformed into the frequency domain. The transform is performed on sub-octave frequency bands (octave means that the bands double in frequency width from one band to the next, sub-octave means that the change is slightly less than two). The input variables, *xre* and *xim*, now contain the impulse response in velocity units and frequency domain. Output is read directly by **tovel.f**.

Envelopes/Codes/sacenvelope.f

This is a script to replace velocity data segment with Hilbert transform envelopes. The minimum length signal size is 201 samples. The actual Hilbert transform is performed by firtrn.f that is being called by this script. The narrow band frequency envelopes are computed by taking the square root of the sum of the velocity signal squared and its squared Hilbert transform. Output replaces the original data input and read by **envelope.f**.

Envelopes/Codes/firtrn.f

The script performs the calculation of Hilbert transform of a signal with an finite impulse response filter. The filter is set to 201 points and constructed by windowing the optimal impulse response using hamming window. It uses subroutines **zero.f**, **overlp.f**, and **zshft.f**. **Overlp.f** performs the Fourier transforms of filter and sequences, and zshft.f shifts the data to remove filtering delay effects. Both scripts are described below. Output replaces original data input and it is read by **sacenvelope.f**.

Envelopes/Codes/zero.f

This subroutine initializes an array to zero. The input is the array that will be zeroed and the size of the array. The output is the arrayed input array. Output is read directly by **firtrn.f**.

Envelopes/Codes/overlp.f

This is a simplified overlap-save script to be used with general filter and arbitrary input sequences. It transforms the filter sequence using the discrete Fourier sequence. It calls in **zero.f**, **copy.f**, and **fft.f**. Using the **fft.f** script, the filter and the data are transformed. Both are stored in frequency domain. Once combined, the output is transformed into time domain and the

scaling effects are removed. Output replaces the input and is read directly by **firtrn.f**.

Envelopes/Codes/copy.f

This is a subroutine that copies one real array into another. The inputs are array that will be copied and its size. The output is a copy of the input array. Output is read be **overlp.f**.

Envelopes/Codes/fft.f

This program computes the Fast Fourier Transform of a real data sequence. The input values are the real and imaginary parts of the data sequence, the cosine and sine tables, the length of the sequence (in samples), and the directional variable (-1 = forward transform, 1 = inverse transform). The input real and imaginary parts are replaced by the transformed results. The script is based on Numerical Recipes FFT technique. The data is transformed back into the time domain, before it is stored in the input variables. It is called twice; first time it transforms the filter, and the second time it transforms the actual data. Output is read by **overlp.f**.

Envelopes/Codes/zshft.f

This subroutine allows shifting signal with zero filling. The procedure is done in place, thus the input is replaced by the output. The input values are: signal, signal length, and an integer number of samples to shift the signal with (positive values represent shift to the right, negative values represent shift to the left). The shift must be smaller than the size of the array. It calls in **zero.f** script to zero the low and high ends of input array. Output is stored in input array and read directly by **firtrn.f**.

Envelopes/Codes/rotate.f

The two horizontal components are rotated given the back azimuth - 90 degrees pole into radial and transverse directions. The input values are: the two input signals, the size of the input signal in samples, angle or rotation (clockwise from direction of first input signal), and signal polarity (e.g. normal polarity means that second signal leads the first by 90 degrees in a clockwise rotation). The output values (*S01* = radial component, *S02* = transverse component) are the rotated signals stored in their input strings. Output is read directly by **envelope.f**.

Envelopes/Codes/sacxapiir.f

This is a subroutine to apply an IIR filter to sequence of data. It uses two subroutines: **design.f** to design an IIR digital filter from analog prototypes, and **apply.f** to apply the filter to the data sequence. The input arguments are: the real data array that will be filtered, the size of the array in samples, the type of analog prototype filter (Butterworth), the number of poles of the analog prototype filter (I use 4), the filter type (I use bandpass), the low and high frequency cutoffs for the filter, the sampling interval, and the number of passes for filtering (I use 2 for zero phase filtering). The output is the filtered data in its original array. Output is read into **envelope.f**.

Envelopes/Codes/design.f

This is a subroutine to design IIR digital filters from analog prototypes. The input values are: the filter order (4 poles), filter type (I use 'BP' for bandpass), technique (I use 'BU' for Butterworth), and low and high frequency cutoffs. The outputs are arrays containing the numerator and denominator co-

efficients for the second order sections, and number of second order sections. It calls in **buroots.f** to compute the poles, **warp.f** to correct for analog to digital filter transformation, and **lptbp.f** to create a bandpass filter out of the lowpass prototype using analog transformation. Then this analog filter is transformed to a digital filter using bilinear transformation (script **bilin2.f**). Output is read directly into **sacxapiir.f**.

Envelopes/Codes/buroots.f

This is a subroutine that computes the Butterworth poles for a normalized lowpass filter. Its input is the filter order. The outputs are the complex array containing poles (one from each complex conjugate, and all real poles), character indicating 2nd order section type (my is CP - complex conjugate pole pair), magnitude of filter at zero frequency (DC value set to 1), and number of second order sections. Output is read into **design.f**.

Envelopes/Codes/warp.f

This function is used to correct for the bilinear analog to digital transformation. I'm using this because the filter is designed from analog prototypes. Input values are the original design frequency specification (Hz) and the sampling interval (seconds). Output is assigned to variables *FLW* (low frequency cutoff) and *FHW* (high frequency cutoff) in **design.f** and used by *lptbp.f*.

Envelopes/Codes/lptbp.f

This is a subroutine to convert a prototype lowpass filter to a bandpass filter via the analog polynomial transformation. The lowpass filter is described in terms of its poles and zeroes (input). The output values are the parameters for second order sections. The script calculates individually the numerator and

the denominator polynomials. It uses FORTRAN internal function CONJG, that gives conjugate CX in terms of a - i*b. Scale numerator based on amplitude equivalence between bandpass filter and lowpass prototype at DC. Output is stored in variables *SN*, *SD*, and *NSECTS* and read by **design.f**.

Envelopes/Codes/apply.f

With this script I apply the IIR filter to the data sequence. The assumption is that the filter is stored as second order sections. The filtering (zero-phase shift) is done in place. The main input values are the data and the filter strings. The output is the filtered data stored in the original data array (replacing the original data). Output is read directly into **sacxapiir.f**.

Envelopes/Codes/sacinterpolate.f

This is a subroutine used to set up data for interpolation. The actual interpolation is done with a script wigint.f. The interpolation is based on sac command 'interpolate'. This script assigns new start and end times and corresponding data length, which are base on start/stop values relative to the origin time (?). The input values are number of samples, sampling rate, and start/end times. I interpolate to 1 second. The output is the reset data, modified time, and sample parameters. Output is read into **envelope.f**.

Envelopes/Codes/wigint.f

This subroutine interpolates evenly or unevenly spaced data based on Wiggins, 1976, publication. The input arguments are: first value for an array of evenly spaced data (I use *xstart0* - first sample), data array, length of data array in points, sampling rate, interpolation factor (-1), and time value to

interpolate to. The output is the interpolated data array (stored in temporary variable scratch). Output is read into sacinterpolate.f.

Envelopes/Codes/sacsmooth.f

This subroutine is based on sac command 'smooth' using mean to smooth the envelope data. Smoothing based on boxcar function width given in **band_setup.f**. I smooth first the start and end points, then continue with the interior data. The data is replaced in place. Output is read into **envelope.f**.

B.2 Processing: Coda amplitude measurements

This step was done using numerous SAC macros and short shell scripts. At first a macro input was created using **pick_setup.sh**. The picks of coda end were done with SAC macro **pick.mac**. The picks of the coda peaks were done with autopicking SAC macro **autopick.mac**, which is based on the SAC function *markp*. Completed picks were stored in each SAC file's header as well as in a central file called *NMTenvelopes_sac_picks.dat* using shell script **pick_wrap.sh**.

B.3 Processing: Coda amplitude calibration

The coda amplitudes were processed in series of steps. The code tree structure is shown below. A short description of what each of the codes do and their input and output is given in sections below the tree structure.

B.3.1 Coda amplitude calibration code tree structure

- Calibration_brune/run_codacal.sh

– Calibration_brune/run_vsearch.sh

. Calibration_brune/vsearch.sh

- Calibration_brune/Codes/pickfit2c.f

. Calibration_brune/Codes/powell.f

– Calibration_brune/run_multiples.sh

. Calibration_brune/multiples_sta.sh

- Calibration_brune/multiples.sh

. Calibration_brune/Codes/dist.f

- Calibration_brune/Codes/distaz.f

. Calibration_brune/Codes/dtmatch.f

– Calibration_brune/run_relsite.sh

. Calibration_brune/relsite_sta.sh

- Calibration_brune/relsite.sh

. Calibrationbrune/Codes/relsite.f

– Calibration_brune/run_shape.sh

. Calibration_brune/shape.sh

- Calibration_brune/Codes/azdistbin.f

. Calibration_brune/Codes/endpick.f

- Calibration_brune/Codes/shape5b.f

. Calibrationbrune/Codes/endpick.f

. Calibration_brune/Codes/powell.f

Calibration_brune/Codes/shape5binterp.f

– Calibration_brune/run_coda_amp.sh

. Calibration_brune/coda_amp_stachan.sh

- Calibration_brune/coda_amp.sh

. Calibration_brune/Codes/sfactor_tmax.f

- Calibration_brune/Codes/ljust.f

- Calibration_brune/Codes/endpick2.f

- Calibration_brune/Codes/sort.f

– Calibration_brune/delete_timesegs.sh

– Calibration_brune/test_picktype.sh

– Calibration_brune/run_psearch.sh

. Calibration_brune/psearch.sh

- Calibration_brune/Codes/mb_scaling.f

- Calibration_brune/Codes/psearch4f.f

. Calibration_brune/Codes/powell.f

– Calibration_brune/format_path_input.sh

– Calibration_brune/run_1D.sh

. Calibration_brune/joint1dpath.sh

- Calibration_brune/Codes/joint1dpath.f

. Calibration_brune/Codes/distaz.f

. Calibration_brune/Codes/brent2.f

. Calibration_brune/Codes/powell.f

– Calibration_brune/run_codatomo.sh

. Calibration_brune/Codes/qtomo5n.f

- Calibration_brune/Codes/distaz.f
- Calibration_brune/Codes/rayseg.f
- Calibration_brune/Codes/raypart.f
- Calibration_brune/Codes/lsqr.f

– Calibration_brune/pathcor.sh

. Calibration_brune/Codes/tomo_predict.f

- Calibration_brune/Codes/ddistaz.f
- Calibration_brune/Codes/rayseg.f
- Calibration_brune/Codes/raypart.f

. Calibration_brune/Codes/1D_predict.f

– Calibration_brune/collect_m0_data.sh

– Calibration_brune/egfshift2.sh

. Calibration_brune/Codes/m0trans.f

. Calibration_brune/Codes/m0trans2.f

- Calibration_brune/Codes/powell.f

. Calibration_brune/Codes/m0trans3b.f

- Calibration_brune/Codes/powell.f

– Calibration_brune/final2.sh

– Calibration_brune/specfit1.sh

. Calibration_brune/Codes/specfit1.f

- Calibration_brune/Codes/brent2.f

– Calibration_brune/specfit2.sh

. Calibration_brune/Codes/specfit2.f

- Calibration_brune/Codes/amoeba2.f

- Calibration_brune/Codes/jacobi2.f

- Calibration_brune/Codes/eigsrt.f

– Calibration_brune/stamag.sh

– Calibration_brune/netmag.sh

– Calibration_brune/checkmags.sh

B.3.2 Coda amplitude calibration program description

This whole section is run using the shell script **runcodacal.sh**. Using logical switches (e.g. yes,no), the individual portions of the calibration method are run. The generall inputs are the narrow-band envelopes in sac format, central file containing all the coda end and peak picks from the network, the NICOYA.event and NICOYA.origin database files, and the calibration control files. In addition, each section has specific inputs from the results of previous sections. The general control files contain constant values for coda measurement, path and attenuation corrections, and the empirical Green's function inversion. I'll describe these codes in sections with order given in Fig. 4.1.

Coda measurement step

In this step I determine the coda group velocity and start time using **run_vsearch.sh**. Thereafter I make a list of multiple events using **run_multi-**

ples.sh. The last step in this subsection computes the coda shape that is used to measure the coda amplitude (**run_shape.sh**).

Calibration_brune/run_vsearch.sh

For this script to run it needs to be pointed to the results directory (currently *janas/Coda/NMTres*) and the file containing coda peak and end picks (currently *janas/Coda/Picking/NMTpickfile_sacdat*). Individual frequency bands are pulled out from the *NMTres/Control/mayedabands.dat* file. According to the bands, the master station/channel pair is copied from the *NMTres/Control/stachan_control.*.dat file*. Then **vsearch.sh** is called in for further work on the input, which is linked with the FORTRAN script **pickfit2c.f** that does the actual model inversion. **Run_vsearch.sh** moves the output from **vsearch.sh** into appropriate directories for results, and created plots using **vgplot.gmt**. The plots are stored in *NMTres/Plots/vsearch_summary.ps*, and also in individual master station-channel directories under the *NMTres/Vsearch* directory.

Calibration_brune/vsearch.sh

In this script I create an input file for a FORTRAN code (**pickfit2c.f**) that does the model inversion. I need the results directory, the pickfile, the frequency band (*key*), and the master station - channel combination (*stachan*) for **vsearch.sh** to run. The input file for the 3 parameter velocity hyperbolic function fit contains: group velocity boundary conditions; *v0*, *v1*, and *v2* for the start model; and the coda peak picks from all stations with the same master (I'm currently adding 2 seconds to each pick to avoid fitting direct S wave). The output is stored in *pickfit.sta.chan.out* and echoed to the screen.

Calibration_brune/Codes/pickfit2c.f

This is a script that fits a 3 parameter hyperbolic function to the coda peak picks. The hyperbolic function represents the coda group velocity, vg, and it is plotted vs. distance. The data is converted to logarithmic scale before fitting. The script uses L1 minimization sum to give an initial estimate of the goodness of fit between the data and the hyperbolic function. Since I have 3 independent parameters, v0, v1 and v2, this script relies on a code **powell.f** to improve the fit by minimizing in all three directions and avoiding linear dependence of the 3 parameters between iterations (see Numerical Recipes p. 511). After final iteration, the data is converted back into linear scale and L1 minimization function is run again. The output of this script contains: final v0, v1, and v2, the minimum and maximum distance, L1 fit before and after minimization using powell.f, number of data points, and number of iterations (*vsearch.sta.chan.out*). In addition, the output also contains distance and group velocity info (*hyperbola.sta.chan.key.out*) so that the results can be plotted using gmt.

Calibration_brune/run_multiples.sh

As in the previous step, **run_multiples.sh** and **multiples_sta.sh** are shell scripts that set up the frequency and station loops. The core of this step is done in shell script **multiples.sh**, which searches for multiple events based on coda origin time (calculated using v_0 from coda peak group velocity inversion), and the epicentral distance (calculated using script **dist.f**). The overlap between events is estimated using **dtmatch.f**.

Calibration_brune/run_relsite.sh

There are three shell scripts again, where the first two (**run_relsite.sh** and **relsite_sta.sh**) set up the frequency and station loops, and the third (**relsite.sh**) solves for relative site effects using FORTRAN code **relsite.f**. In this step, I would solve for a relative site effects at each stations for a number of channels. Because I only have one channel (basically E + N + H) at all stations, in this step I don't use the FORTRAN code, but I set all the results = 0 in the shell script.

Calibration_brune/run_shape.sh

The **run_shape.sh** script is used to set up master station-channel pairs for **shape.sh** that calls in FORTRAN programs to ivert for the shape functions. The input consists of files and constants. The files are the following: *masterlist.box.dat* that contains the event-station information such as origin time, location, and magnitude; *mayedabands.dat* that lists all of the narrow-band frequency bands; *coda_window_params.dat* that constains the coda parameters such as t_start or t_max (Table 4.2); and the *shape5start.dat* file that contains the initial model for the cubic functions used to estimate the shape parameters for spreading and attenuation. I also input boundary conditions for epicentral distance and depth. The grid input parameters are number of azimuthal and radial bins (24 and 25 respectively); 10 km for the outer bound of first radial layer; and maximum distance for the last radial layer's outerbound.

Calibration_brune/Codes/azdistbin.f

Using the input files and constants, I create an input file for FORTRAN code **azdistbin.f**. The input is following: file with path to the envelope sac file, single or multiple statement and amount of overlap if multiple; group

velocity parameters v0, v1 and v2; smothing width (swide); amplitude error cutoff constrain; t_start and t_max; number of azimuthal and radial bins (24 and 25, respectively); the outer boundary of first azimuthal grid (10 km) and of the last azimuthal grid (500 km). After **azdistbin.f** creates the radial and azimuthal grid, the code will populate the individual cells with number of events within its boundaries, their magnitude and pick type. For cells that contain only earthquakes without pick, I use a coda end autopicking code **endpick.f**, however, the peak-noise difference must be greater than 4. The results from **azdistbin.f** are the events, the single or multiple string, and the multiple overlap time if any for all cells containing any data.

Calibration_brune/Codes/shape5b.f

Input needed for this code is the output from **azdistbin.f**; v0, v1 and v2 for particular band; smoothing width (swide); amplitude error cutoff (acut); tstart and tmax. The input file contains all of the frequency bands, with the above variables listed for each band. For data that does not have a coda end pick, used **endpick.f** to get that pick. The output file shape.sta.chan.out contains all of the unformated write statements from **shape5b.f**. The cubic function parameters are separated from the rest of the results and stored in *shape_params.sta.chan.out* in the results directory.

Calibration_brune/Codes/shape5binterp.f

In this code, the inputs are the cubic coefficients and the central frequency for each band. The code computes b0,b1,b2,s0,s1 and s2, which are the outputs.

Calibration_brune/run_coda_amp.sh

This shell script sets up a station-channel loop, in which it calls the script **run_amp_stachan.sh**. In **run_amp_stachan.sh** I set up loop to go through all the frequency bands for the particular station-channel combination. Within this loop is the core of this step. Here I call **coda_amp.sh** to create input for the FORTRAN codes that do all the work.

Calibration_brune/Codes/sfactor_tmax.f

This program computes the median value between t_start and t9 (coda end pick), sorts the values using **sort.f**, and measures the coda source amplitude as: median amplitude - spreading term + attenuation term (in log domain). In addition, this program also uses **ljust.f** to left-justify the input files, and **endpick2.f** to pick coda end for events have not been picked manually based on their shape functions. The output of this program is: event name and event ID; origin ID; event latitude, longitude and depth; epicentral distance, magnitude, magnitude type, source (author), event type, station, channel, b-term and γ term, coda origin time, the start and end of used coda window, number of points within that window, source amplitude, minimum amplitude of the 20s lonq window within the trace, average peak amplitude within the selected coda window, and picktype (manuall vs. automatic). The results are stored in files *CSF.sta.chann.f-band.dat* in the *NMTres/CSF* directory.

Calibration_brune/delete_timesegs.sh

This is a shell script that will remove data based on signal quality from the results stored in the *CSF* directory. The bad time segments for each station are determined by looking at the differences in noise values (log10 m/s) for the whole recording life of the station. If there are isolated shifts in the

noise value, the data is removed. It will display the original number of events and the number of events after removing the bad time periods. The good data (same column structure as in *CSF* directory) is stored in *CSF1* directory.

Calibration_brune/test_picktype.sh

This shell script tests for few picktype problems. At first it test for events that have simultaneously manual and automatic pick. Then it will look for explosions within the dataset, as these cannot be processed in the following steps the way these steps are setup. And finally it will look for manuall picks on events that I have known seismic moments for, as these must have picks to be able to shift the corrected amplitudes to absolute scale later on.

Path, site and transfer function corrections

run_psearch.sh This shell script sets up loop based on master station and channel, and on frequency band. Within this loop it calls **psearch.sh** that needs to be directed to the results directory and it runs using a given frequency band - station - channel combination input. The shell script **psearch.sh** calls FORTRAN codes **mb_scaling.f** and **psearch4f.f**.

Calibration_brune/Codes/mb_scaling.f This FORTRAN script solves for source amplitude and corner frequency based on *Taylor and Hartse* (1998). The input values are magnitude and frequency, and the outputs are S-wave source amplitudes, corner frequency and a low frequency spectral level (see *Taylor and Hartse* (1998) for details).

Calibration_brune/Codes/psearch4f.f The input values are event ID, station, channel, epicentral distance, amplitude corrected for source terms,

peak-to-noise difference (noise determined as minimum amplitude window using smoothing of 20 s), frequency, phase velocity (3.5 km/s), site term, attenuation term (q0=400), spreading coefficients, and the spreading parameters X0 (1000 km) and Xtrans (1). Input amplitudes are weighted iversely with increasing distance using frequency and distance. The initial and final data fit is determined using L1.2 minimization, the minimum model value is found using **powell.f**. Output values for each station-channel-frequency combination are attenuation (as Q), spreading coefficients and parameters, site terms, the initial and final L1.2 fits, number of data points, and number of data points for each station. In addition, the code outputs another file with distance and the predicted path model behavior over that distance.

Calibration_brune/format_path_input.sh This shell script takes the results from **psearch.sh** and formates them to be used in the 1D and 2D path inversion steps. The input it creates contains event ID, station and channel, station and earthquake latitude and longitude, site corrected amplitude, and two dummy noisy variables (log scale, set currently to -100).

Calibration_brune/run1D.sh In the shell script run1D.sh I create a frequency band loop in which I invoke shell script **joint1dpath.sh**. Here I create input for FORTRAN code joint1dpath.f.

Calibration_brune/Codes/joint1dpath.f Input values are: formated source corrected amplitude output from **format_path_input.sh**, frequency boundaries for each band, phase velocity (3.5 km/s), spreading coefficients p1 and p2, xcross, xtrans and eps. At first I remove L1.2 minimized mean from the site terms using **brent2.f** which is a technique adopted from *Press*

et al. (2007). Next use **distaz.f** to compute epicentral distance (km), azimuth (degrees), back-azimuth (degrees) and great circle arc length (degrees). Then I minimize the path and site model parameters using **powell.f**, and compute again L1.2 mean of the site terms. The output values are: station, site mean, Q, spreading coefficients, xcross and xtrans, and number of events per station used in the calculations; the minimum and maximum epicentral distance for each station, event ID list, station list, data, epicentral distance, and residuals between the observed and predicted data.

Calibration_brune/run_codatomo.sh This is a shell script that calls in FORTRAN code **qtomo5n.f**. Here I need the regional box and grid spacing (set to 0.1 by 0.1 degrees) and the frequency band list. I create input for **qtomo5n.f** that contains: frequency, path parameters (p1, p2, xcross and xtrans), regularization term (lambda=1.0 for frequencies below 1.5 and above 13 Hz, otherwise = 0.5), eps (frequency dependent path parameter), low and high residual cutoff (-1.5 and 1.0), and phase velocity (3.5 km/s). The inversion following inversion is run twice, at first with twice as high lambda term and the second time with the original lambda to improve convergence.

Calibration_brune/Codes/qtomo5n.f With this code I solve for Q and site term using amplitude difference data. I have total of 336 grid nodes, 21 in latitude and 16 in logitude. At first I use **distaz.f** to compute epicentral distance and backazimuth. Next I call **rayseg.f**, which is a FORTRAN code that splits the great circle arc segment between the station and the earthquake and returns the latitude and longitude of the midpoint between any station-event pairs. Then I use **raypart.f** which creates a grid cell around this midpoint

and returns the grid cell corners. I use linear interpolation to get the attenuation at the center of a path segment, given the 4 values on the surrounding grid. I do this without knowing the attenuation at the grid points, those are the parameters I have to invert for. I compute the least squares solution for the model using Frobenius norm (code **lsqr.f**). The output from **qtomo5n.f** includes grid latitude and longitude, Q, attenuation, error estimates of Q model in linear scale), and number of data in given grid cell.

Calibration_brune/pathcor.sh At first I use a FORTRAN script **tomo_predict.f** to calculate path and site corrections based on tomography results for one band -station pair at time. The output from **tomo_predict.f** is used in **1D_predict.f** to apply the corrections to the amplitudes.

Calibration_brune/Codes/tomo_predict.f The input values are files containing the source corrected amplitudes, files with site terms and Q, as well as tomographic grid, frequency, path parameters (spreading coefficients, xcross, xtrans), and phase velocity (3.5 km/s). At first uses **ddistaz.f** to compute epicentral distance for all event-station pairs. Next uses **rayseg.f** and **raypart.f** to compute the midpoint along the great circle arc between station and event and get the grid cell bounds about this midpoint. Output values are event name, station latitude and longitude, event latitude and longitude, and the correction value (estimated as correction = site term + spreading - attenuation term).

Calibration_brune/Codes/1D_predict.f Input values are event ID and epicentral distance, path and site corrections, path parameters, attenuation and phase velocity (3.5 km/s). Output values are event ID, epicentral

distance and path corrections for that event.

Analysis

At this point I have coda amplitudes that are corrected for S-to-coda transfer, path and site terms. Now I need to express the amplitudes in units that are consistent with independent seismic moment estimates, or in other words I need to shift the amplitudes to absolute units. At first I use the earthquakes with independent seismic moment estimate to compute the transfer function (or Empirical Green's Function). Then I apply the shift to all corrected amplitudes. Next I can used the shifted data to solve for corner frequency, moment-based magnitude and apparent stress.

Calibration_brune/collect_m0_data.sh The is a shell script that collects information for the earthquakes with independent M_0 estimates. The input values are the independently known seismic moments and the path corrected amplitudes. The output values are the origin ID for each earthquake, station and channel, frequency band, path and source corrected amplitude and the independent M_0 estimate.

Calibration_brune/egfshift2.sh This is the actual transfer function script, where I want to find a function that causes earthquake amplitude with known M_0 to shift to absolute units by following MDAC scaling law. The input values are the output values from **collect_m0_data.sh**, initial value for apparent stress (1 bar); source parameters zeta, alphas, betas, radpatp, radpats, moref, and psi.

At first I run **m0trans.f** to get the transfer function between corrected

amplitudes and the independent M_0 estimates. The inputs are the corrected amplitudes and the source parameters. The outputs are frequency index, frequency, transfer function, median values, residual and number of amplitudes used for the correction.

Next I use **m0trans2.f** to invert for the reference apparent stress and transfer function simultaneously, using the transfer function from **m0trans.f** as initial guess. The input values for **m0trans2.f** are the frequency band and its low and high bounds, the transfer function and the source parameters. The initial and final residuals are calculated using L1.2 method. The model is minimized using **powell.f**. Output contains the even ID, station, frequency band, corrected amplitude, seismic moment and residuals, where the residuals are computed as the amplitude - predicted amplitude - trasfer function difference.

As last transfer function step, I run the inversion one more time using **m0trans3b.f**, this time solving simultaneously for transfer function, apparent stress and corner frequency. I use apparent stress results from **m0trans2.f** as initial guess. Other inputs are the source parameters, corrected amplitude, and frequency. The model includes the transfer function, corner frequency and apparent stress for each event and frequency band. The initial and final misfit is determined using L1.2 method, and the model is minimized using **powell.f**. The output contains the transfer function for each frequency band, corner frequency and apparent stress for each event, as well as the residuals.

Calibration_brune/final2.sh In this shell script I apply the transfer function to all of the corrected amplitudes.

Calibration_brune/specfit1.sh After the shift of the corrected am-

plitude to absolute units, I calculate the M_0 fit based on the MDAC scaling model. At first I create input file for **specfit1.f** that fits the source spectra to get M_0 usind MDAC model scaling. The input contains source parameters, frequency, station, channel, event ID, master station and channel, frequency, shifted amplitude and the error value. During the fitting, I look for the best midpoint in seismic moment and minimize this midpoint using **brent2.f**. I run the fitting twice, at first for individual stations and then for all of the station that recorded a particular earthquake and their results pass residuals criteria. The output contains event ID, seismic moment, corner frequency, apparent stress, apparent stress error, number of amplitudes used for the fit, and number of stations used for the fit.

Calibration_brune/specfit2.sh In this final step, I fit simulataneously the M_0 and corner frequency and re-calculate apparent stress. The input values are the source parameters, event ID, station, center frequency, amplitude, and error, and the apparent stress. The fit is done with **specfit2.f**. This code calls **amoeba2.f** that minimizes the fit for M_0 and ω_c. Next I estimate covariance at the solution point using **jacobi2.f**. The eigenvalues are then sorted in descending order using **eigsrt.f**. After that I calculate apparent stress again, this time using the minimized ω_c and M_0. The output consists of event ID, M_0, ω_c, σ_a, σ_a error, M_0 error, ω_c error, number of bands below ω_c, number of bands above ω_c, number of amplitudes used, ω_c/minimum frequency, maximum frequency/ω_c.

Calibration_brune/stamag.sh This shell script creates tables for station-magnitude results.

Calibration_brune/netmag.sh This shell script creates tables for magnitude from the network.

Calibration_brune/checkmags.sh Here I check that the number of results for station and network magnitude tables is consistent.